

ENHANCING THE PHOTOACTIVE SURFACE AREA OF DYE SENSITIZED SOLAR
CELLS USING SUPERCRITICAL FLUIDS

By

FAHD MOHSIN RAJAB

A DISSERTATION PRESENTED TO THE GRADUATE SCHOOL
OF THE UNIVERSITY OF FLORIDA IN PARTIAL FULFILLMENT
OF THE REQUIREMENTS FOR THE DEGREE OF
DOCTOR OF PHILOSOPHY

UNIVERSITY OF FLORIDA

2010

© 2010 Fahd Mohsin Rajab

To my parents and wife: Thank you for your unconditional support with my studies

ACKNOWLEDGMENTS

I would like to thank my advisor Kirk J. Ziegler and the faculty in my committee for their support and guidance. I would also like to thank the undergraduate students who assisted with this work especially David Loaring and Jake Hyvonen. I would like to acknowledge the faculty and staff at Major Analytical Instrumentation Center, Interdisciplinary Center for Biotechnology Research, Particle and Engineering Research Center and Chemical Engineering Department at University of Florida especially Kerry Siebein, Valentin Craciun, Karen Kelley and Jim Hinnant. I would also like to acknowledge the University of Florida Opportunity Fund and the Donors of the American Chemical Society Petroleum Research Fund for support of this research.

TABLE OF CONTENTS

	<u>page</u>
ACKNOWLEDGMENTS.....	4
LIST OF TABLES.....	7
LIST OF FIGURES.....	8
ABSTRACT.....	11
CHAPTER	
1 INTRODUCTION	14
Problem Description	14
Objectives and Results	16
Dye Sensitized Solar Cells.....	17
Supercritical Fluids	18
Electrodeposition	20
2 SUPERCritical FLUID PURIFICATION OF HIPCO AND SWAN SINGLE WALL CARBON NANOTUBES (SWCNTS).....	24
Initial Remarks	24
Materials and Experimental	25
Results and Discussion.....	28
Closing Findings	31
3 PREPARING THICK, DEFECT-FREE FILMS OF ANATASE TITANIA FOR DYE SENSITIZED SOLAR CELLS	42
Preliminary Remarks.....	42
Experimental Section	44
Results.....	47
Discussion	50
Conclusionary Findings.....	53
4 NONDESTRUCTIVE MEASUREMENT OF DYE ADSORPTION ONTO TITANIA FILMS	64
Preliminary Remarks.....	64
Materials and Methods.....	65
Results and Discussion.....	67
Concluding Remarks	70

5	ENHANCING THE PHOTO ACTIVE SURFACE AREA OF DYE SENSITIZED SOLAR CELLS	78
	Initial Remarks	78
	Materials and Methods.....	80
	Results and Discussion.....	83
	Concluding Remarks	86
6	CONCLUSION.....	96
APPENDIX		
A	SUPERCritical FLUID PURIFICATION OF (PRE-PURIFIED) SINGLE WALL CARBON NANOTUBES (SWCNTS)	98
B	ELECTRO-DEPOSITION AND TEMPLATE REMOVAL USING SUPERCritical CARBON DIOXIDE	105
	Nanowire Electrodeposition Using Supercritical Carbon Dioxide.....	105
	Template Removal Using Supercritical Carbon Dioxide	109
	Conclusions and Future Avenues of Research.....	109
C	ANODIZING ALUMINUM AND NANOWIRE ELECTRO-DEPOSITION.....	113
LIST OF REFERENCES		
BIOGRAPHICAL SKETCH.....		
		124

LIST OF TABLES

<u>Table</u>		<u>page</u>
1-1	Diffusivities and viscosities of liquids, supercritical fluids and gases.....	22
2-1	HiPco carbon nanotubes metal oxide content (wt %) with residual tri-butyl phosphate (TBP).	32
2-2	HiPco carbon nanotubes metal oxide content (wt %) after subtraction of residual tri-butyl phosphate TBP.....	32
2-3	Metal ions removed from HiPco and Swan SWCNTs.....	33
3-1	Experimental conditions for preparing thick, defect-free titania films on ITO and FTO substrates.....	54
3-2	Efficiency of DSSCs made with 10-20 µm titania films on FTO substrates sintered at varied pressures at 450°C.. ..	55
4-1	Measured molar extinction coefficients for N-719 and N-749 dyes.....	72
5-1	The efficiency of the best DSSCs made with FTO substrates with titania films of various thicknesses.	87

LIST OF FIGURES

<u>Figure</u>		<u>page</u>
1-1	Capillary condensation/evaporation for liquid solvents in nanopores.....	23
2-1	Setup of carbon nanotubes metal extraction using supercritical carbon dioxide.....	34
2-2	TGA of raw and treated HiPco carbon nanotubes.....	34
2-3	Tri-butyl phosphate (TBP) residuals in HiPco carbon nanotubes.....	35
2-4	Final metal oxide content of treated HiPco carbon nanotubes.....	35
2-5	TGA of raw and treated Swan carbon nanotubes.....	36
2-6	TGA of raw and treated HiPco carbon nanotubes by multiple extractions.....	36
2-7	Final metal oxide content of treated Swan carbon nanotubes.....	37
2-8	TEM images of HiPco and Swan carbon nanotubes treated by sc-CO ₂ extraction.....	38
2-9	TEM image of HiPco carbon nanotubes treated by the one pot method..	38
2-10	Raman spectroscopy of raw and treated HiPco carbon nanotubes.....	39
2-11	Raman spectra of raw and treated Swan carbon nanotubes.....	39
2-12	Fluorescence of raw and treated HiPco carbon nanotubes.....	40
2-13	Fluorescence of (10 %) Swan and treated Swan carbon nanotubes.....	41
3-1	The preparation steps for making thick titania films on transparent conductive oxide (TCO) substrates..	56
3-2	SEM image of titania film (~25 µm thick).	57
3-3	X-ray diffraction of 20 µm thick titania films.	57
3-4	Raman spectra of µm titania films on FTO substrates.....	58
3-5	Microscopic images of the final titania films on FTO.....	59
3-6	The effect of sintering pressure on the defect density of titania films.	60
3-7	Microscopic images of the final titania films cooled at a rate of –1°C/min..	61

3-8	The effect of the cooling rate during annealing on the defect density of titania films.....	61
3-9	Performance characteristics of DSSCs fabricated from photoanodes sintered at different pressures.....	62
3-10	SEM images of 20 μm titania films sintered at varied pressures.....	63
4-1	N-719 and N-749 dye extinction coefficient in NaOH.....	73
4-2	Spectroscopic peaks of N-719 and N-749 dyes in NaOH solution and in solid titania.....	74
4-3	Absorbance of N-719 and N-749 dyes adsorbed onto the solid titania film or dissolved in NaOH.....	75
4-4	Comparison of the concentration of N-719 and N-749 dye determined by solid state or NaOH solution.....	76
4-5	Spatial profiles of N-719 dye absorption and short circuit current in 10 μm titania film.....	77
5-1	Electron transport and recombination paths between the semiconductor and the electrolyte.....	88
5-2	Absorbance of 7, 10 and 20 μm titania films in N-719 dye	88
5-3	Solubility of N-719 dye in sc-CO ₂ using in situ UV-VIS measurements.....	89
5-4	Solubility of N-719 in sc-CO ₂ using cloud point measurements.....	90
5-5	Absorbance of impregnated titania films by UV-VIS spectroscopy.....	91
5-6	Performance characteristics of DSSCs fabricated from photoanodes in N-749.....	92
5-7	Efficiency and electron life time of DSSCs fabricated from photoanodes in N-749.....	93
5-8	Performance characteristics of DSSCs fabricated from photoanodes in N-719.....	94
5-9	The effect of t-butanol and concentration of N-719 on the efficiency of DSSCs.....	95
A-1	Raman spectra of raw and treated pre-purified carbon nanotubes.....	103
A-2	Fluorescence of raw and treated pre-purified carbon nanotubes.....	103

A-3	Final metal oxide content of treated pre-purified carbon nanotubes.....	104
B-1	High pressure system for electrodeposition.....	112
B-2	SEM image of 200 nm whatman anodisc 13.	112
B-3	TEM image of nickel deposits from a watt bath solution.....	112
C-1	Substrates after deposition of Cr and Al layers, wrapped in Al foil for silica deposition.....	115

Abstract of Dissertation Presented to the Graduate School
of the University of Florida in Partial Fulfillment of the
Requirements for the Degree of Doctor of Philosophy

ENHANCING THE PHOTOACTIVE SURFACE AREA OF DYE SENSITIZED SOLAR
CELLS USING SUPERCRITICAL FLUIDS

By

Fahd Mohsin Rajab

December 2010

Chair: Kirk Jeremy Ziegler

Major: Chemical Engineering

The contribution of this dissertation is primarily related to surface interfaces and methods for enhancing materials properties. I discuss optimum extraction conditions for purifying single wall carbon nanotubes using supercritical carbon dioxide without altering their unique properties. Also, I discuss preparation of thick defect free titania films on different substrates for dye sensitized solar cells by reducing film stresses. I show a nondestructive dye analysis technique to measure dye absorbance on solid films and generate concentration and current spatial profiles, which illustrate the effect of multilayer dye formation on device performance. Moreover, I show improvement in device efficiency based on stable thick titania films impregnated with a ruthenium dye using supercritical carbon dioxide.

One of the most important challenges the world faces today is clean and affordable energy. Photovoltaic devices such as dye sensitized solar cells (DSSCs) present a promising solution for conversion of light to energy efficiently. The recorded efficiency of these devices is 10 to 11 %, which currently makes them uneconomical for production at large scale. Fundamental to such devices is the harvesting of sunlight molecules by a thin film of wideband semi-conductor nanoparticles coated with a dye.

The amount of photons harvested depends on dye thickness. Cell efficiency is a measure of electrons transfer through a wideband semiconductor, such as titanium dioxide (TiO_2), to generate current between the two electrodes.

The typical conductive electrodes can be replaced with an alternative conductive film made with carbon nanotubes. My effort was focused on purifying the carbon nanotubes from their inherent metal impurities using supercritical carbon dioxide (sc- CO_2). Hipco and Swan single wall carbon nanotubes (SWCNTs) have been purified using sc- CO_2 at temperatures ranging from 35 to 75°C and pressures ranging from 250 to 400 atm. Single and multiple extractions were performed with up to 80 % removal efficiency.

Enhancing the photoactive surface area of DSSCs using a supercritical fluid was examined. First, the solubility of two ruthenium dyes in sc- CO_2 was investigated. This part of the study required purchasing of all the equipments and parts needed to carry out the experiments as well as understanding the limitations of the setup. The solubility of ruthenium dyes in supercritical carbon dioxide, performed with the inclusion of co-solvent in a concentration of 5 to 30 % at 35 to 55°C and 100 to 400 atm, was measured by UV-VIS spectroscopy and cloud point measurements.

Second, anatase titania nanoparticle films were prepared on fluorine-doped tin oxide (FTO) and tin-doped indium oxide (ITO) substrates. The sintering and annealing steps were controlled by reducing the pressure and the rate of temperature change to reduce the stresses generated during film preparation, allowing the generation of thick titania films on both FTO and ITO with minimal defects. Films as thick as 25 μm were prepared on FTO substrates with a defect density of only 6.0 %. DSSCs fabricated with

titania films on FTO substrates at different vacuum levels showed enhanced device performance compared with standard cells. The cells prepared at intermediate pressures showed higher short-circuit current, open-circuit voltage and efficiency.

Third, a nondestructive method was developed to quantify the adsorption of dyes in titania films for DSSCs. UV-VIS spectroscopy showed that the absorbance of dyes in the solid film scales with the absorbance from the typical destructive method used to quantify dye adsorption. Using dye absorbance in the solid film and profilometry to measure the thicknesses of titania films on FTO substrates, extinction coefficients for N-719 and N-749 dyes adsorbed onto titania were determined. The nondestructive approach was able to calculate mole concentrations of both dyes for film thicknesses of 7 to 20 μm . This method also provided spatial profiles of dye concentration and short-circuit current of an impregnated film which showed optimum coverage was required for best device performance.

Finally, N-719 and N-749 ruthenium dyes were used to impregnate up to 20 μm of a thick anatase titania films on FTO for DSSCs using conventional dip and supercritical fluid methods. The dyes were dissolved in different solvent mixtures, including sc-CO₂. DSSCs fabricated with these films show up to 9.44 % and 6.57 % efficiency for N-719 and N-749, respectively. Although these efficiency levels remain below recorded efficiency values, the results of this thesis not only provide better understanding of the important factors but also suggest that higher efficiencies can be obtained if thicker films are impregnated with a suitable dye using the supercritical fluid approach.

CHAPTER 1 INTRODUCTION

Problem Description

Nanomaterials most important characteristic is high surface area. Transport in high surface area and porous structures, is essential for utilization of nanomaterials unique properties. However, due to capillary effects and surface forces, transport in nanopores can be limited at the nanosize level. This hinders use of nanomaterials in many applications where purity and integrity are needed for performance and better efficiencies. An important application that presents these problems is dye sensitized solar cells (DSSCs). Fundamental to this device is harvesting of sunlight molecules by a thin film of wide band semi-conductors nanoparticles coated with a dye. The amount of photons harvested depends on dye thickness. Cell efficiency is a measure of electrons transfer through the wideband semiconductor to generate current between the two electrodes [1].

DSSC electrodes and carbon nanotubes. DSSC electrodes are transparent conducting oxide (TCO) films on glass substrates. Film preparation techniques such as physical vapor deposition are costly and time consuming. The conductivity of the currently used films, fluorine-doped tin oxide (FTO) or tin-doped indium oxide (ITO), is reduced as films are made more transparent. Single wall carbon nanotubes (SWCNTs) can be used to make cost effective, highly transparent and conductive films for charge transport [2]. However, they have inherent metal impurities that limit use of their electronic properties. Most purification techniques use acids which affect the integrity of the SWCNTs structure or give poor extraction efficiencies due to capillary effects.

Nanoparticle-DSSC. A key factor for efficiency in DSSCs is the high photo active surface area of the semiconductor. However, most DSSCs utilize only a 10 µm film with a monolayer of dye coverage because of electron diffusion length and reduced electron collection efficiency. A thick semiconductor nanoparticle film can provide a high photoactive surface area if dye coverage is enhanced. Thick films in general show defects due to compressive or tensile forces that lead to film failure.

Nanowire-DSSC. Electron transport was found to be low in a nanoparticle film due to electron's percolation through a random network of the polycrystalline material. Nanowires enable faster electron transport but lack the high surface area. Therefore, synthesis of high density nanowire arrays is essential for achieving both high surface area and faster electron transfer. Template synthesis of nanowires by electrodeposition in electrolyte solution can lead to incomplete pore inclusion of template's channels due to hydrogen hydrolysis and surface tension of electrolyte solution. It can also produce polycrystalline materials with larger grain sizes and pin holes due to hydrogen hydrolysis which can create electron trap sites. When nanowire arrays are synthesized, the template is dissolved in an acid solution. However, template removal by acids allows surface forces to cause aggregation of the deposited nanowires, which prevents their effective use where a uniform high density nanowire array is required.

Dye coverage efficiency. When films are impregnated with dye, they are typically dissolved in a solution to measure their concentration from their absorbance. This limits ability to investigate DSSC efficiency based on film dye coverage. The time range for optimum impregnation varies depending on film properties and solvent mixtures. Optimum dye coverage of the semiconductor can increase the photo active surface

area and promote light harvesting efficiency. However, capillary effects and surface forces of liquid solvents can limit transport of dye and lead to poor dye coverage.

Objectives and Results

In chapter 2, purification of carbon nanotubes using supercritical carbon dioxide is investigated with nanotubes of different properties made with different synthesis processes. The results of an initial study on purification of carbon nanotubes using supercritical carbon dioxide is discussed in appendix A. In chapter 3, anatase thick titania films on transparent conductive glass are prepared with minimum defect density by controlling sintering and cooling conditions. DSSCs are prepared with these films and show higher device performance. In chapter 4, a nondestructive dye adsorption technique is developed to allow concentration analysis of dye on solid titania films used in fabricated DSSCs. Optimal dye adsorption time ranges are determined for titania films with different thickness. In chapter 5, wet and gas dye coverage methods are examined for ruthenium dyes dissolved in various (co)solvent mixtures for impregnating thick titania films. The efficiencies of fabricated DSSCs are determined and parameters show importance of optimum transport and film thickness for device efficiency. The rest of this chapter discusses background on dye sensitized solar cells, supercritical fluids (SCF), and electro-deposition.

Miscibility of hydrogen in SCF miniemulsions should prevent pin holes formations and pores blockage in nanowire synthesis by hydrogen hydrolysis. Electrodeposition with SCF miniemulsions is similar to pulse electrodeposition, which should enhance smaller grain sizes and better crystallinity. Template removal using a SCF should prevent capillary effects that cause aggregation. In appendix B, the theory and preparation work for synthesis of nanowires using sc-CO₂ is discussed. This part of my

research was halted due to equipment shortage and interest in pursuing the typical method for synthesis of nanowires, which is discussed in appendix C.

Dye Sensitized Solar Cells

Dye-sensitized solar cells (DSSCs) are potential future devices for converting light to electricity at large scale. DSSC main components are about 10 micron (μm) of a wide band gap semiconductor film such as titania (TiO_2) or zinc oxide (ZnO) nanoparticles, which provides a large internal surface area for sufficient chromophore to yield high light absorption in the 400–800 nm region, where much of the solar flux is incident, a monolayer of organic dye molecules absorbed onto the semiconductor, and a liquid electrolyte containing the redox couple $\text{I}-/\text{I}_3-$ which interpenetrates the dye-coated nanoparticles [1]. When a photon excites the electron in the dye, it is injected into the conduction band of a wide band gap semiconductor and is diffused across it to the current collector (anode) and carried to the cathode where it reduces I_3- in the electrolyte. Then, the dye is regenerated by the $\text{I}-$, thereby closing the cyclic conversion of light to electricity [3,4].

Under sunlight, an injected electron may experience many trapping events before either penetrating to the electrode or recombining with an oxidizing species, primarily I_3- in the electrolyte. The main parameters of the electron transport in DSSCs were determined to be the light intensity of the irradiation light, semiconductor film thickness, concentration of iodine, and nanoscale titania materials that make the semiconductor electrode [5]. A high electron diffusion coefficient and a low recombination rate constant are required for highly efficient dye-sensitized solar cells. Attempts to improve cell efficiency above its record of 10-11 % by thickening the nanocrystalline film to improve its light absorption at red wavelengths have failed because increasing film thickness is

limited by electron diffusion length. Also, higher dye loadings for photon harvesting show low diffusion and high recombination [1,6].

A typical dye sensitized solar cell is fabricated on transparent conducting oxide (TCO) glass. The conductive coating is either fluorine-doped tin oxide or tin-doped indium oxide. Screen printing transparent titanium dioxide is deposited by spreading with a blade or by spin coating. Sintering is done at 450°C for inter-particle connectivity. Film thickness is between 10 to 20 µm, film porosity is 50 to 65 %, average pore size is 15 nm and particle diameter is 15 to 20 nm. Ruthenium dyes such as ruthenium 620 are used to sensitize wide band-gap oxide semiconductors like titanium dioxide efficiently up to a wavelength of 920 nm. The counter electrode is fabricated from FTO-coated glass, with a platinum layer as catalyst for the reduction of the redox electrolyte at the counter electrode. The redox electrolyte iodide, tri-iodide (I^-/I_3^-) is used for electrical contact between the electrodes and for dye regeneration [7]. Cell efficiency n is given by equation (1-1):

$$n = \frac{FF \cdot V_{oc} \cdot J_{sc}}{P_{in}} \quad (1-1)$$

where P_{in} is light density, V_{oc} is voltage at open circuit, and J_{sc} is current at short circuit.

Fill factor (FF) is given by equation (1-2):

$$FF = \frac{P_{mp}}{V_{oc} \cdot J_{sc}} \quad (1-2)$$

where P_{mp} is power at maximum point ($V_{mp} \cdot J_{mp}$) [1,8].

Supercritical Fluids

Supercritical fluid (SCF) is a substance above its critical pressure, temperature and density but below the pressure required to condense it to a solid. It has properties

of both liquids and gases; it can dissolve solid compounds like liquids because of its solvent strength and it has high mass transfer rate like gases due to its high diffusivity and low viscosity. Solvent strength of a SCF depends on density and can be adjusted by tuning the density of fluid phase by varying temperature and pressure. Therefore, conducting reactions in SCFs enables control of viscosity, diffusivity and surface tension. Nanomaterials of better properties have been synthesized using SCFs [9,10]. Diffusion is inversely proportional to viscosity as given by Einstein Stokes relation in equation (1-3):

$$D = \frac{K_B T}{6\pi\eta r} \quad (1-3)$$

where K_B is thermal constant, T is temperature, η is solvent viscosity, r is radius of a diffusing particle [11]. Supercritical fluids viscosities are one to two orders of magnitude less than liquids, hence diffusivities are much higher, see Table 1-1 [12]. SCFs are environmentally friendly and have been investigated as replacements for hazardous organic solvents. The most common supercritical fluids are water and carbon dioxide. Supercritical carbon dioxide (sc-CO₂) critical pressure and temperature are 72.8 bars 31.1°C [12]. Sc-CO₂ is nontoxic, nonflammable, and cheap (second least expensive after water). SCFs most important property is their zero surface tension.

Transport in nanopores is critical for reactions and synthesis in nanomaterials. Surface tension, vapor pressure and potential energy from pore wall can affect phase properties within nanopores, causing capillary effects such as capillary condensation or evaporation. The Kelvin equation (1-4) describes the effect of surface tension and vapor pressure on condensation or evaporation in cylindrical pores with zero contact angles:

$$KT \ln\left(\frac{P_v}{P_{sat}}\right) = -\frac{2\gamma V_p}{R-t} \quad (1-4)$$

where K is Boltzmann's constant, T is temperature, P is pressure, and the subscript v indicates vapor pressure and sat indicates saturation, γ is the surface tension of the liquid, V_p is the volume per molecule of liquid, R is the radius of the pore and t is the thickness of the phase inside the pore [13-16]. Capillary evaporation and condensation of various liquid solvents in cylindrical nanopores was modeled using the Kelvin equation. As seen in Figure 1-1, capillary evaporation drops in nanopores of less than 60 nanometers (nm). However, the drop is at maximum in pores less than 10 nm. SCFs can be utilized in such nanopore sizes especially for their zero surface tensions.

Electrodeposition

The main components of an electro deposition cell are electrolyte containing metal ions, electrodes (cathode and anode) and a power source. The metal ions in the solution are reduced to the metal form by gain of electrons at the cathode surface. The metal solution interface is the locus of electro deposition process. It is where the interaction between the electrically conductive electrode and the ionic conductive solution takes place. The properties of water and ionic solutions are of great relevance to the properties of the two metal solution interfaces [17,18].

In an ionic-water solution, there are ion-ion interactions and ion-water interactions. In ion-ion interactions, each positive ion is surrounded by atmosphere of negative ions and vice versa. The solution is largely neutral but cations and anions are not distributed uniformly in an ionic solution. The main forces in ion water interaction are ion-dipole interactions, which cause the orientation of water molecules in the immediate vicinity of an ion. This in effect causes the formation of primary shell of with completely oriented

water molecules and secondary region of partially oriented water molecules. The description of the metal-ionic solution interface and the two regions and the prediction of potentials are best described in Grahame Triple-layer model, which has two planes of closest approach; (IHP) inner plane of partially or fully dehydrated ions and (OHP) outer plane of closest approach of fully dehydrated ions [18].

Transfer of ionic species can happen in an electrochemical cell due to migration, convection and diffusion effects. Migration of ions of electrolyte occurs due to change in electric field and is always present. Supply of excess of non-electro active ions (electrolyte solution), minimizes the contribution of migration and decreases solution resistance, which improves working electrode potential control. Convection happens due to stirring and should be minimized. The main driving force of an electrodeposition process is diffusion of analyte by a concentration gradient. Nernst equation provides a link between electrode potential and the concentrations of participants in the electrode process. For electrodeposition when only an oxidized species is present, the relationship is given by the following expressions (1-5):

$$E = E^\circ + \frac{RT}{NF} \ln C_o(0,t) \quad (1-5)$$

where E is overall potential needed, E° is standard potential, R is the thermal rate constant, T is temperature, N number of moles, F is Faraday constant and $C_o(0,t)$ is the concentration of oxidized species at the electrode surface. Electrodeposition rate can be controlled by current density through over-potential [17]. The thickness can be controlled and it is the product of molecular weight and the reciprocal of number of electrons, Faraday's constant, area and density. The maximum length of a nanowires array is limited by the thickness of the template channels.

Table 1-1. Diffusivities and viscosities of liquids, supercritical fluids and gases.

Property	D(cm ² /sec)	η (g/cm/s)
Liquids	10 ⁻⁵	10 ⁻²
SCF	10 ⁻³	10 ⁻³
Gases	10 ⁻¹	10 ⁻⁴

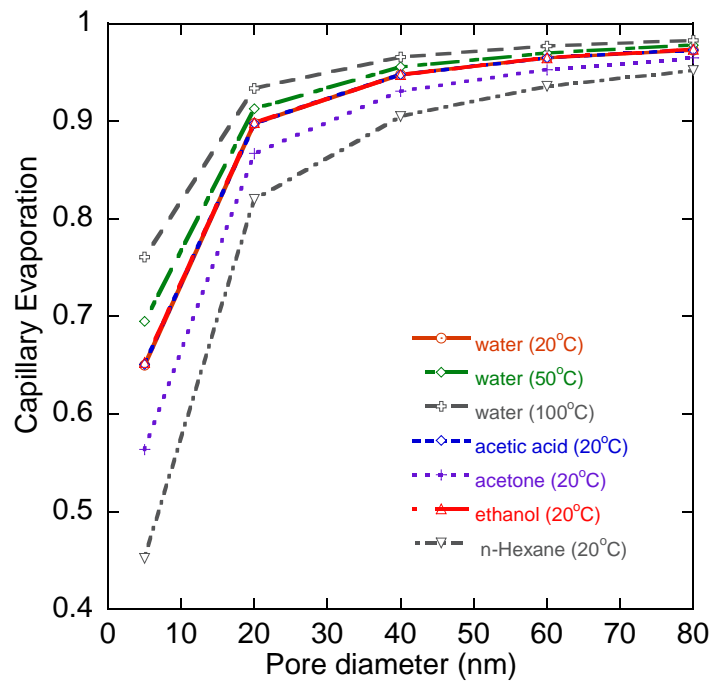


Figure 1-1. Capillary evaporation for liquid solvents in nanopores using the Kelvin equation.

CHAPTER 2
**SUPERCRITICAL FLUID PURIFICATION OF HIPCO AND SWAN SINGLE WALL
CARBON NANOTUBES (SWCNTS)**

Initial Remarks

Single-walled carbon nanotubes (SWCNTs) have been the focus of recent research due to their unique electronic and mechanical properties. Their properties can be utilized for materials science applications and electronic devices. For example, they can be used as conductive films in dye sensitized solar cells (DSSCs) instead of fluorine-doped tin oxide (FTO) or tin-doped indium oxide (ITO). SWCNTs films can be made transparent while remaining highly conductive. SWCNT films show high transparency in a wide spectral range from the UV-visual to the near IR range. Lagemaat et al. [19] purified SWCNTs using an acid reflux method and produced films of $50 \Omega/\text{sq}$ sheet resistance and 70 % transmittance at 650 nm. Films can be prepared by spraying or spin coating on glass substrates [20]. However, there are several technical difficulties that must be overcome before they can be used. Purification of SWCNTs from inherent metal impurities [21] is important for making conductive films. Most purification processes use strong acids or oxidative environments to remove the impurities, which can oxidize the carbon nanotube sidewalls.

The intensity of the carbon nanotubes are reduced by acid treatment. Blackburn et al. showed the effect of protonation on the florescence intensity of carbon nanotubes [22]. Wang et al. [23] showed the highly selective purification one pot technique. The carbon nanotubes are dissolved in an aqueous mixture of hydrogen peroxide (H_2O_2) and hydrogen chloride (HCl) at 40-70°C for 4-8 h. However, this method causes defects to the carbon nanotubes. Magnetic purification of carbon nanotubes has been studied by Wiltshire et al. [24]. Although this method can be promising, but scalability to the

industry level can be challenging. Chiang el al. [25] used a wet gas method by oxidizing at 225°C, sonicating in HCl and annealing at 800°C in Ar. Raman spectroscopy of the treated sample in their study show defects to the structure of the nanotubes. Wang el al. [26] reported high metal extraction efficiency from carbon nanotubes using electrochemical pretreatment step with ethylenediaminetetraacetic acid (EDTA) electrolyte, in a three electrode setup with AgCl reference electrode. However, this method can be limited by onion shells formation around the metals preventing oxidation and effective metal extraction.

Inefficiencies of wet methods are attributed to high surface tension of liquids solvents. In this chapter, supercritical fluid carbon dioxide (sc-CO₂) is used to purify different types of carbon nanotubes from their inherent metal impurities at different temperatures and pressures. Multiple extractions are performed for optimum extraction condition, to enhance metal removal efficiency. The carbon nanotubes samples are analyzed by TGA, Raman spectroscopy and fluorescence to assess metal removal and properties of the carbon nanotubes. Transmission electron microscopy is used to evaluate metal size and distribution before and after purification.

Materials and Experimental

Materials. Tri-n-butylphosphate (TBP – 99% purity from Sigma-Aldrich), and hexafluoroacetylacetone (HFA – 95% purity from Sigma-Aldrich) were used as received. HiPco and Swan single wall carbon nanotubes (SWCNTs) were used as received. Carbon dioxide was received from Airgas and used as received. Micro Reactor MS-16 was purchased from High Pressure Company.

Experimental. HiPco and Swan carbon nanotubes were processed to remove metal impurities used in their synthesis by supercritical fluid extraction at temperatures

ranging from 35 to 65°C and pressures between 250 and 400 atm. TBP was used as an oxidizing agent and HFA was used as a chelating agents. Moreover, reagent and solubility limitation was probed by using TBP with an acid complex and 5 % ethanol as a co-solvent in supercritical carbon dioxide extraction. 0.5 ml HFA and 1.04 ml of TBP complex (1.5 ml TBP and 1.5 ml of 70 % HNO₃) were used for HiPco carbon nanotubes sc-CO₂ extraction at 60°C and at 200 atm. Static extraction was performed for 1 h and 30 min followed by dynamic extraction for 15 min. Also, the extent of metal oxidation was tested by an electrochemical pretreatment step. Pretreatment was performed in ethylenediaminetetraacetic acid (EDTA) electrolyte, ethanol and water solutions and 2-15 mg of CNTs. The three electrode setup included a platinum foil as the working electrode, platinum wire as the counter electrode and AgCl reference electrode. Chronoamperometry was run for 4000 seconds at 0.41 V. Solution was mixed for 5 min and then centrifuged for 1-2 h at 10,000 rpm. The effect of acid treatment on nanotube properties was shown by using the one pot method with a sample of HiPco carbon nanotubes. The tubes are dissolved in an aqueous mixture of hydrogen peroxide (H₂O₂) and hydrogen chloride (HCl) at 40-70°C for 4-8 h.

Sc-CO₂ extraction. Isco syringe pump was used to pressurize CO₂ to the micro reactor. The reactor (9/16" I.D. × 9" in length, 24 mL) of stainless steel was immersed in a water bath heated to the desired temperature by a temperature regulator in internal circulation mode, see Figure 2-1. Approximately 22 mg of Hipco and 40 mg and Swan carbon nanotubes and a small stir bar were wrapped in P8 filter paper and inserted into the reactor. A magnetic stirrer was used to stir the magnetic stir bar. The oxidizing and

chelating agents were loaded according to the raw carbon nanotube metal content (approximately at 2:1 ratio) into the reactor using a syringe with a leur lock connection.

The reactor was loaded with CO₂ to the desired pressure and allowed to reach equilibrium. CO₂ was again loaded until the desired pressure was reached. The reactor was held at the extraction conditions for an hour. The CO₂ was then slowly vented and bubbled through water, yielding purple droplets in the water solution [26-28]. The carbon nanotubes were recovered from the reactor and bath sonicated in ethanol for 30 min. The suspension was then filtered through a 0.1 µm PTFE membrane and washed with hexane. To simplify the filtration process, alternatively, the carbon nanotubes were flushed multiple times with sc-CO₂ at constant flow mode to flush out the used reagents. This method was tested with some hipco carbon nanotubes samples.

Characterization. Thermogravimetric (TGA) analysis was conducted in air up to 800°C at a ramp rate of 10°C/min. Inductively Coupled Plasma Spectroscopy (ICP) analysis was performed on homogenized collected effluent. Raman spectra were recorded on the solid carbon nanotubes using a Reinshaw Invia Bio Raman with excitation from a 785 nm diode laser. For fluorescence measurements, carbon nanotubes were dispersed in 1 wt % SDBS surfactant. The suspension was homogenized with 10,000 rpm for 1 hour followed by tip sonication for 10 min. Toluene was added to the suspension and then mixed with vortex at 1,500 rpm for 30 seconds. Finally, the suspension was allowed to settle for more than 2 h. The suspension was characterized using an Applied NanoFluorescence Nanospectrolyzer (Houston, TX) with excitation from 662 and 784 nm diode lasers.

Results and Discussion

Effect of pressure and temperature in sc-CO₂ extraction. Pretreatment of HiPco carbon nanotubes with an electrochemical technique showed small oxidation peaks from iron catalyst. This indicates inaccessibility of metals for oxidation due to poor penetration of the solvents in the carbon nanotubes. For the raw Hipco carbon nanotubes, initial metal content ranged from 25 to 30 %. TGA of purified Hipco carbon nanotubes showed final ash content ranging from 21.6 to 43.5 %, see Figure 2-2 and Table 2-1. This increase in ash content was attributed to residual amounts of reagents in samples, see Figure 2-3. Final ash content of Hipco carbon nanotubes treated with TBP was higher than that of TBP or HFA alone. Analysis using TGA results was performed to determine the actual amount of metal oxide left in each treated sample, see Table 2-2. TBP weight is the difference of weight between 110°C and 307°C; the first sample temperatures after the boiling points of water and TBP, respectively, during the TGA ramp program. The percentage of TBP left in a carbon nanotube sample was 11.87 %, see Figure 2-3. Based on these calculations, the final metal oxide content without TBP is found for each sample. The best removal efficiency was found at 325 atm, see Figure 2-4. ICP showed optimum iron removal of around 40 ppm at this pressure. The other metals present such as Mg, Mo and Ni are at low concentrations below 3.5 ppm, see Table 2-3. On the other hand, Swan carbon nanotubes, initial metal content ranged from 84 to 90 %. The treated samples at the range of temperatures and pressures showed best removal at 55°C and 325 atm, see Figure 2-5. ICP showed optimum magnesium removal of around 500 ppm at this condition. The other metals present such as Fe, Mo and Ni are at low concentrations, see Table 2-3.

Effect of multiple extractions and higher temperatures. Multiple extractions with fresh chelating agent and oxidant were performed at optimum conditions for both HiPco and Swan carbon nanotubes. Hipco carbon nanotubes did not show better metal removal efficiency at any of the conditions tested, see Figure 2-6. This confirms that efficiency limitation was not due to lack of reagents. Hence, a single extraction step was sufficient under these conditions.

However, swan carbon nanotubes showed enhanced metal removal efficiency at 45°C and 325 atm. The extraction was repeated twice at this condition and the final ash content was reduced from 30 % to 20 %, see Figure 2-7. The extraction at 55°C and 325 atm showed a similar final ash content of 20 % with a single extraction. Extraction was repeated 4 times at 55°C and 325 atm but did not show further reduction in metal content. Further, the efficiency was performed at 65°C and 325 with a single extraction and showed final ash content of 16.7 %. Extraction was repeated at that condition but did not show efficiency improvement. Moreover, the extraction was performed at 75°C and 325 atm. However, this showed reduction in efficiency with final ash content of 25 %. These results show the best extraction conditions are at higher temperatures around 65°C and 325 atm. This is primarily due to optimum oxidation and chelating conditions for removal of magnesium.

HiPco carbon nanotubes have higher density of metal impurities in the 3-5 nm range. On the other hand, Swan carbon nanotubes have impurities of different particle sizes; see Figure 2-8a and c. The high metal content in Swan carbon nanotubes allows high initial oxidization and removal of metals, which makes more inaccessible metal sites available for oxidization. Unlike Swan carbon nanotubes, HiPco low metal content

allows low removal which prevents solvents penetration to oxidize more metals sites. The difficulty in removing all metal content was due to the onion shell formation around the metals; see Figure 2-8b and d. Supercritical carbon dioxide extraction was very efficient in removing the majority of the metal impurities. Figure 2-9 shows impurity remaining in similar onion shell formation even with the one pot method using acid for treatment.

The solubility of the reagents in supercritical carbon dioxide was found to have no effect on further removal. Adding 5 % of ethanol as a co-solvent did not enhance extraction efficiency. Moreover, the processing condition of the carbon nanotubes had no effect on removal; two Hipco carbon nanotubes sample were processed with and without crushing and both samples showed the same final ash content. Finally, combining supercritical extraction with acid treatment did not enhance oxidation and metal removal. This shows that the supercritical fluid method was sufficient in a single extraction step when performed at optimum conditions.

Carbon nanotube integrity assessment. Raman spectra were performed on the solid carbon nanotubes. The Raman spectra for the HiPco nanotubes shows the characteristic peaks at 1594 and 1295 cm⁻¹. The low D/G ratio is indicative of high quality carbon nanotubes with few defects, see Figure 2-10. After purification using TBP and HFA in sc-CO₂, there are no changes to the Raman spectra. The Raman spectra of raw and treated Swan nanotubes are comparable, see Figure 2-11. These results show that there was no sidewall damage caused to the nanotubes during the supercritical carbon dioxide extraction process. The one pot method showed final ash content of 12 %. However, Raman spectra shows lower D/G ratio, indicative of nanotube defects.

Fluorescence is a sensitive analysis technique to probe any oxidative environment on the carbon nanotubes. The peaks of fluorescence of HiPco carbon nanotubes correspond to the different types of the carbon nanotubes. The spectra showed no decrease in intensity after purification, see Figure 2-12. Fluorescence of one pot treated carbon nanotubes show the least intensity compared with other treated samples. The fluorescence of treated Swan carbon nanotubes at 65°C and 325 atm was compared with the 10 % purified sample provided by the manufacturer. This was due to difficulty of taking fluorescence of the raw high metal content Swan carbon nanotubes. Fluorescence peaks correspond to different types of carbon nanotubes and show no decrease in intensity after purification, see Figure 2-13.

Closing Findings

Supercritical carbon dioxide extraction showed that metal impurities were most effectively removed at an intermediate pressure of 325 atm and at high temperatures for both HiPco and Swan carbon nanotubes. This was due to enhanced oxidation of the main metal catalyst in each carbon nanotube material. The effective extraction was due to sc-CO₂ low surface tension and high diffusivity. The carbon nanotubes were purified from their impurities without sidewall damage or decreased fluorescence intensity. The final metal oxide content of 16 % for both HiPco and Swan carbon nanotubes was attributed to the onion shell formation around the metals.

Table 2-1. HiPco carbon nanotubes metal oxide content (wt %) with residual tri-butyl phosphate (TBP) after supercritical carbon dioxide treatment with TBP and HFA.

Temp, Pressure	35°C	45°C	55°C
250 atm	31.01	32.22	43.49
325 atm	30.85	28.38	25.29
400 atm	21.64	30.97	35.46

Table 2-2. HiPco carbon nanotubes metal oxide content (wt %) after subtraction of residual tri-butyl phosphate TBP. TGA analysis is used to estimate the amount of residual TBP. TBP initial wt is the difference of wt between 110°C and 307°C (wt of CNT), the first sample temperatures after the boiling points of water and TBP. TBP wt % is 11.87 % (ratio of TBP in CNT from TGA) times the ratio of TBP/CNT of a sample. TBP final wt for each sample is found by multiplying TBP wt % by TBP initial wt. This value is subtracted from final wt reading of TGA to calculated adjusted final metal oxide content.

T (°C), P (atm)	ash wt (w/TBP)	wt at 110°C	wt at 307°C	TBP initial wt	TBP/CNT	TBP wt %	TBP final wt	final ash wt
35, 250	31.01	10.17	5.28	4.89	0.93	0.11	0.54	20.80
35, 325	30.85	7.47	3.72	3.75	1.01	0.12	0.45	18.69
35, 400	21.64	4.76	3.17	1.59	0.50	0.06	0.10	18.63
45, 250	32.22	11.00	5.45	5.55	1.02	0.12	0.67	19.81
45, 325	28.38	11.81	5.87	5.94	1.01	0.12	0.71	16.07
45, 400	30.79	11.26	5.67	5.59	0.99	0.12	0.65	19.15
55, 250	43.49	20.00	8.45	11.55	1.37	0.16	1.87	21.14
55, 325	25.29	8.28	5.20	3.08	0.59	0.07	0.22	21.09
55, 400	35.46	18.34	8.76	9.58	1.09	0.13	1.24	21.27

Table 2-3. Metal ions removed from HiPco and Swan SWCNTs. ICP analysis was performed on effluent from the different supercritical carbon dioxide extraction conditions. The detection level is 0.004, 0.003, 0.012 and 0.026 ppm (mg of metal/ Kg of solvent) for Mo, Ni, Fe and Mg, respectively. BDL stands for below detection level.

SWCNTs	T (°C), P (atm)	Mo (ppm)	Ni (ppm)	Fe (ppm)	Mg (ppm)
HiPco	35, 325	0.22	0.26	36.13	3.53
	45, 325	0.07	0.31	37.49	1.77
	55, 325	0.24	0.06	39.35	1.21
	45, 250	0.18	0.27	38.51	0.54
	45, 400	0.11	0.19	40.43	BDL
Swan	45, 325	BDL	61.64	8.57	124.31
	55, 325	0.05	0.18	5.14	292.34
	65, 325	BDL	0.31	9.24	500.92
	75, 325	BDL	0.17	11.37	258.65
	45, 400	BDL	0.42	4.02	72.33

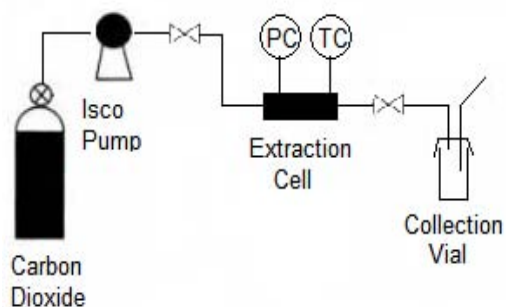


Figure 2-1. Setup of carbon nanotubes metal extraction using supercritical carbon dioxide. Sc-CO₂ is pressurized from isco pump to the cell with oxidizing and chelating agents. Static extraction is performed under pressure and temperature control before purging through a collection vial.

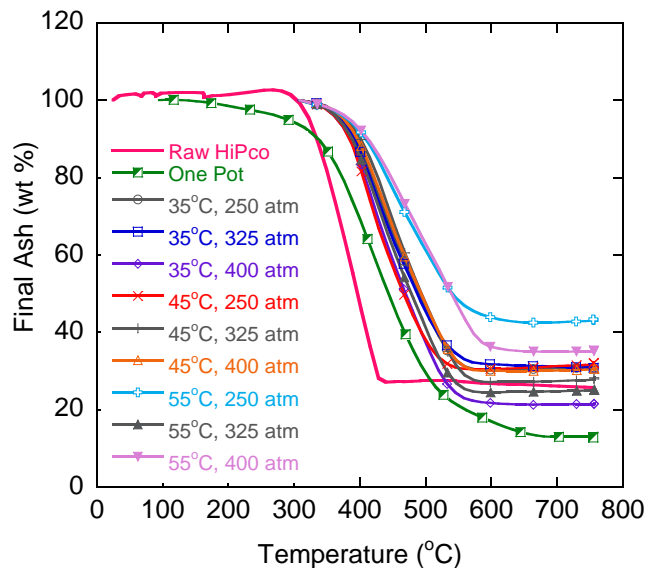


Figure 2-2. TGA of raw and treated HiPco carbon nanotubes. Supercritical carbon dioxide extraction was performed at temperature from 35 to 55°C and pressures from 250 to 300 atm. Raw HiPco shows metal oxide (ash) content of 25 wt %. Treated samples by sc-CO₂ show metal oxide of 20 to 40 wt % due to remaining tri-butyl phosphate (TBP) in carbon nanotubes. One pot purification shows final metal oxide content of 12 wt %.

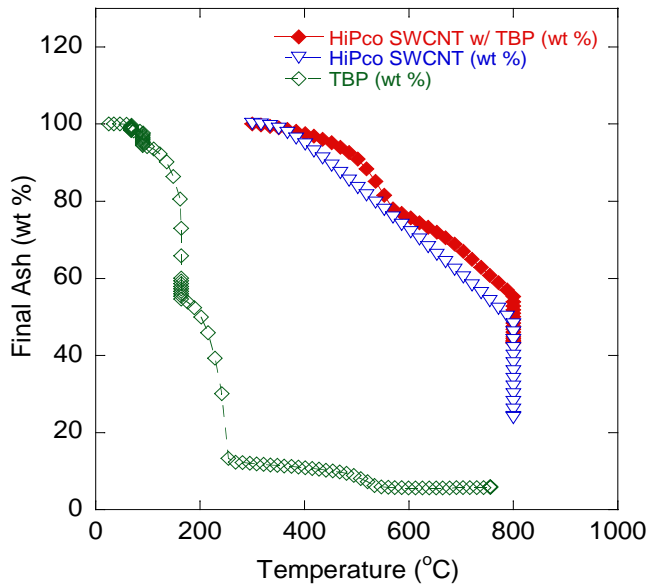


Figure 2-3. Tri-butyl phosphate (TBP) residuals in HiPco carbon nanotubes. TGA of carbon nanotubes with TBP shows final metal content of ~40 % compared with 25 % and 8.5 % of carbon nanotubes and TBP, respectively. This result indicates 11.87 % residuals of TBP in carbon nanotubes.

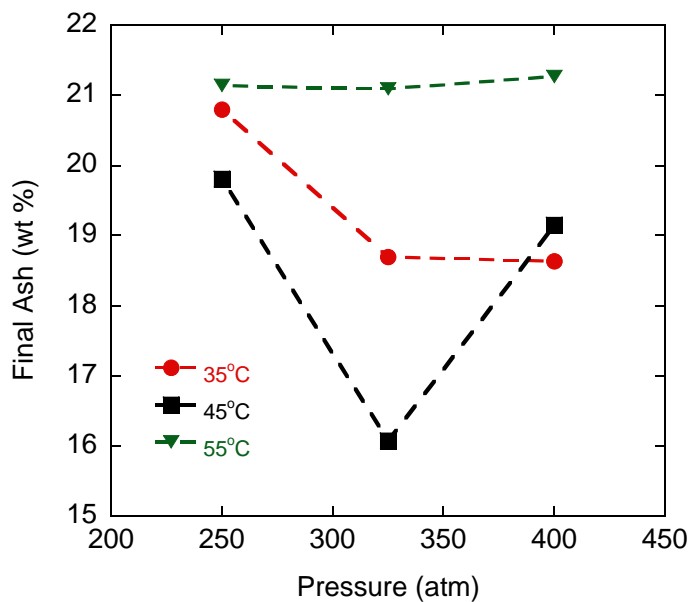


Figure 2-4. Final metal oxide content of treated HiPco carbon nanotubes. Supercritical carbon dioxide extraction was performed at temperature from 35 to 55°C and pressures from 250 to 400 atm. A single extraction at 45°C and 325 atm shows 16 % of final ash content.

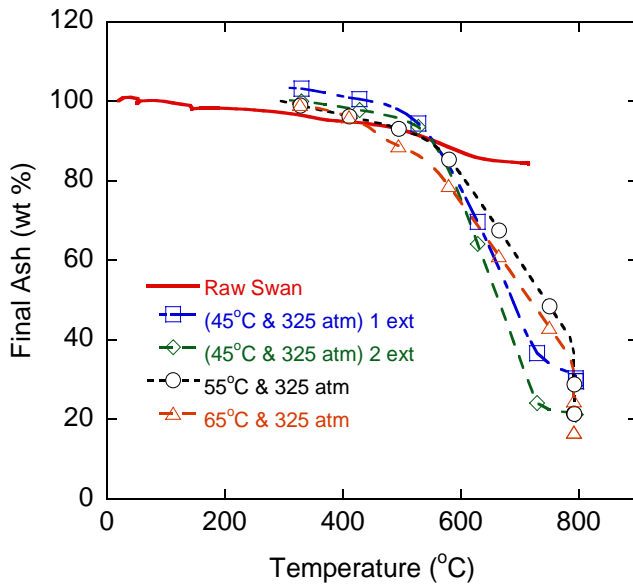


Figure 2-5. TGA of raw and treated Swan carbon nanotubes. Supercritical carbon dioxide was performed at temperature from 35 to 55°C and pressure from 250 to 400 atm. Raw Swan shows metal oxide of 84 wt %. Purified samples by sc-CO₂ show metal oxide of 20 to 30 wt %. A single extraction at 65°C and 325 atm shows 16.7 wt % of final ash content compared with 20 wt % for multiple extractions at 45°C and 325 atm.

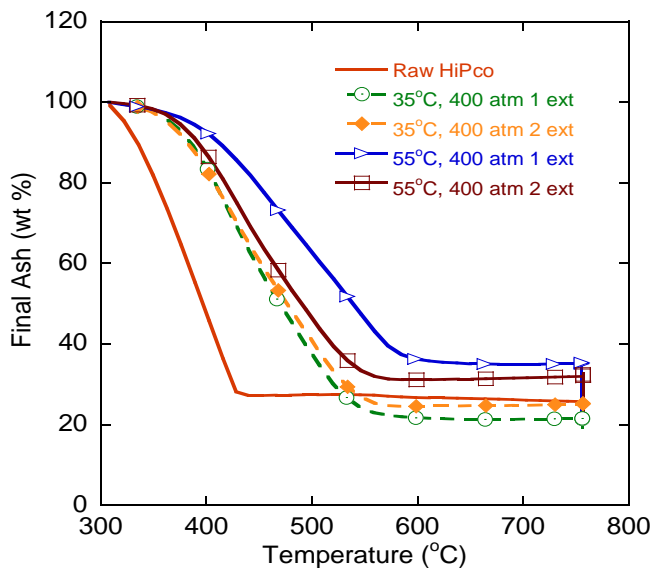


Figure 2-6. TGA of raw and treated HiPco carbon nanotubes by multiple extractions. Multiple extractions at 35 and 55°C and at 400 atm using supercritical carbon dioxide do not show significant metal removal. Raw HiPco shows metal oxide content of ~ 25 wt %.

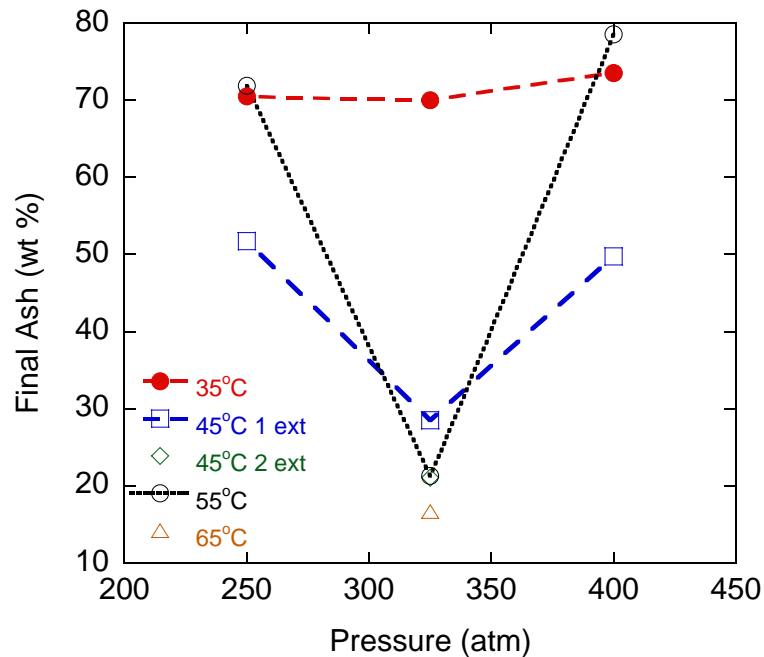


Figure 2-7. Final metal oxide content of treated Swan carbon nanotubes. Supercritical carbon dioxide extraction was performed at temperature from 35 to 65°C and pressures from 250 to 400 atm. A single extraction at 65°C and 325 atm shows 16.7 wt % of final ash content compared with 20 wt % for multiple extractions at 45°C and 325 atm.

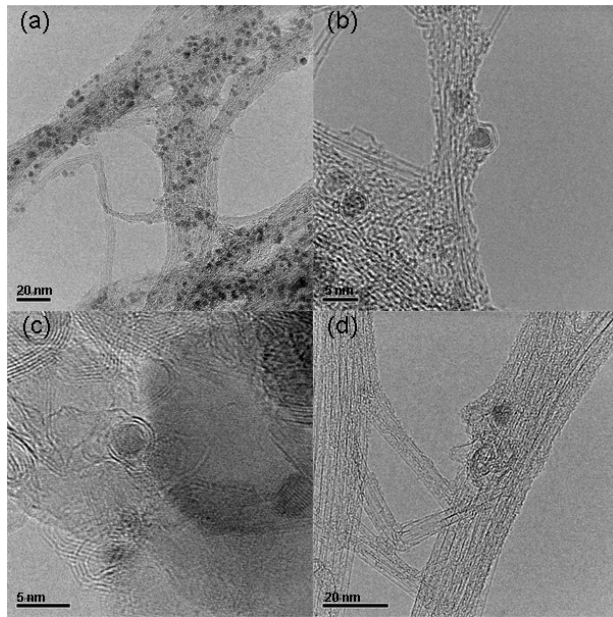


Figure 2-8. TEM images of raw HiPco (a) treated HiPco (b) raw Swan (c) and treated Swan carbon nanotubes (d). HiPco carbon nanotubes have higher density of metal impurities in the 3-5 nm range (a), whereas Swan carbon nanotubes have impurities of different particle sizes (c). Onion shell formation around the metals show prevents their removal (b) and (d).

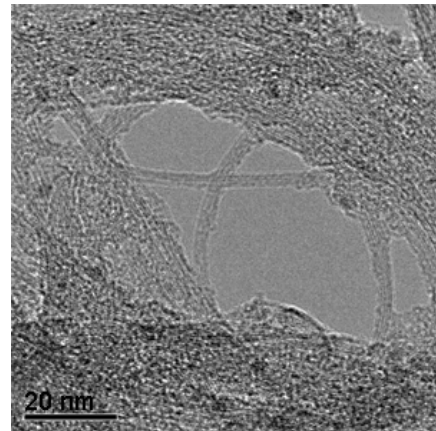


Figure 2-9. TEM image of HiPco carbon nanotubes treated by the one pot method. The sample shows remaining metal content.

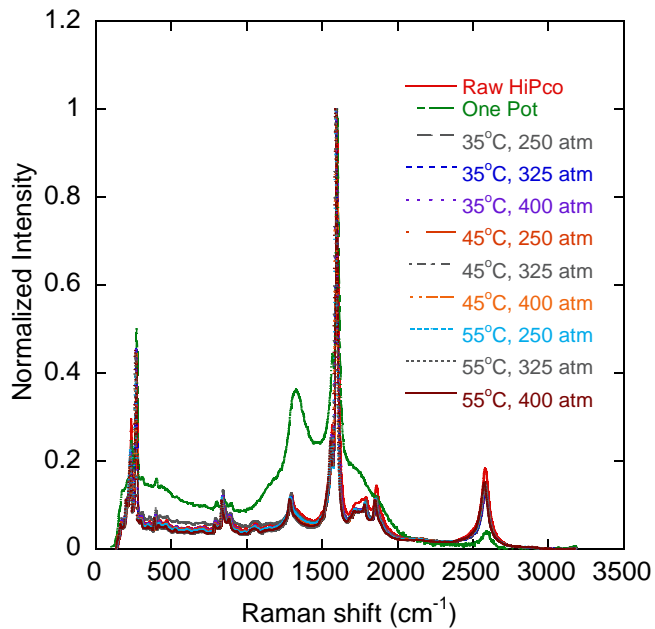


Figure 2-10. Raman spectroscopy of raw and treated HiPco carbon nanotubes. Supercritical carbon dioxide treated samples show comparable spectra to the raw sample suggesting no side wall damage to the nanotubes. One pot method shows lower D/G ratio (D peak at 1295 cm^{-1} , G peak at 1594 cm^{-1}), indicative of side wall damage.

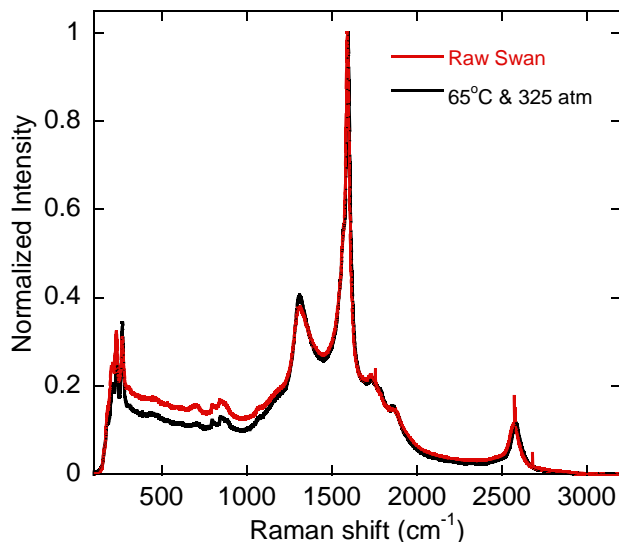


Figure 2-11. Raman spectra of raw and treated Swan carbon nanotubes. Supercritical carbon dioxide treated sample at 65°C and 325 atm shows comparable spectra to the raw sample indicating no side wall damage to the carbon nanotubes.

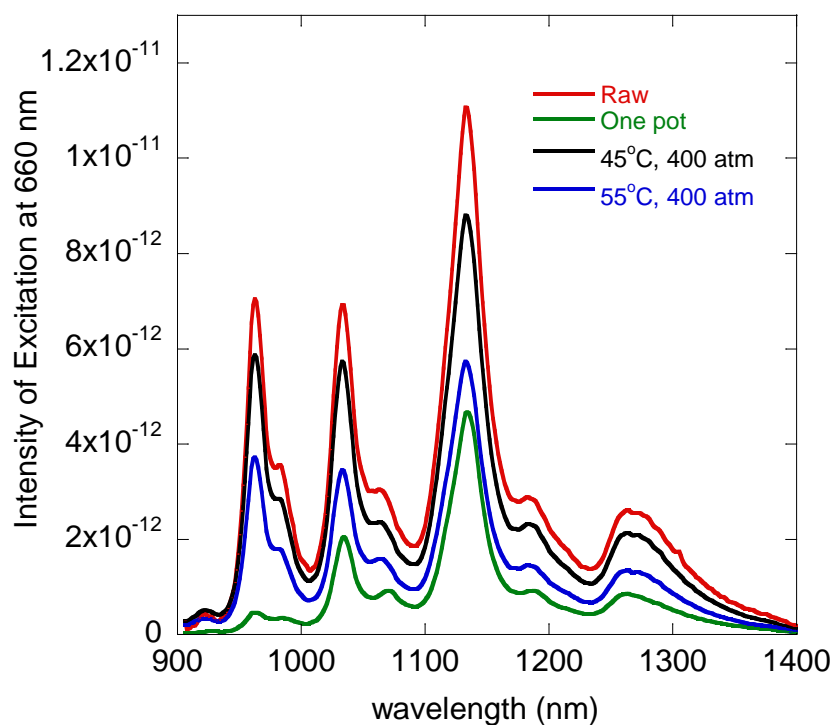


Figure 2-12. Fluorescence of raw and treated HiPco carbon nanotubes. Supercritical carbon dioxide extractions at 45 to 55°C and 400 atm show comparable intensity to the raw sample. One pot method shows least intensity.

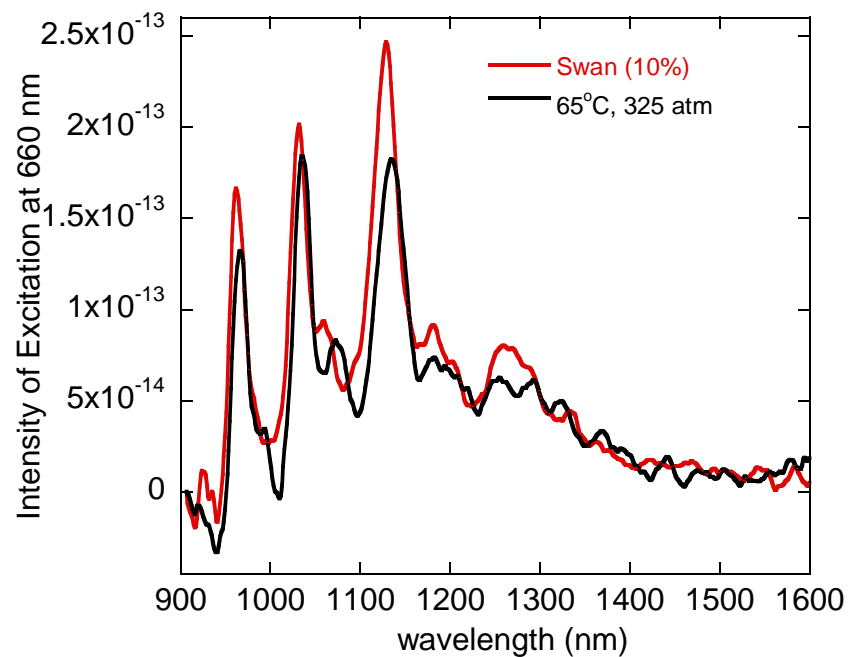


Figure 2-13. Fluorescence of (10 %) Swan and treated Swan carbon nanotubes. Supercritical carbon dioxide extraction at 65°C and 325 atm shows comparable intensity.

CHAPTER 3

PREPARING THICK, DEFECT-FREE FILMS OF ANATASE TITANIA FOR DYE SENSITIZED SOLAR CELLS

Preliminary Remarks

The anatase phase of titania receives the most interest out of the three polymorphs of titanium (IV) oxide because of its photo-catalytic activity. The unusual properties associated with nanostructured films of titania provide numerous applications in the fields of solar cells, optics, environmental remediation [29], antibacterial coatings [30], photo-catalytic reactors [31], electrochromic displays [32], and gas sensing.[33] Interestingly, titania also exhibits photo-induced superhydrophilicity when exposed to UV irradiation [34]; the titania reverts back to its hydrophobic nature once left in a dark state for several hours. Carp et al. [35]provide a good review of the interesting properties and applications of titania.

Titania films have been prepared by numerous techniques, including chemical vapor deposition [36] sputtering [37], atomic-layer deposition [38], and deposition of sols [39]. The structure and properties of titania films are strongly dependent on the substrate and preparation method. In many applications, the deposition of sols is preferred because it is cost effective and prepares porous films of titania. The conventional method used to prepare these porous TiO₂ films is to deposit the nanoparticles onto a substrate and heat the film to temperatures of 450 – 550°C. The heating step removes the solvent used to aid dispersion of the nanoparticles onto the substrate. As the solvent evaporates, the nanoparticles adhere to the substrate and form an electrically connected network. Multiple “coat and bake” [40] steps are often used to prepare thick films (~ 10 μm) of titania.

The difficulty in preparing thick films from multiple cycles comes from the stresses that are generated during the rapid heating and cooling cycles, resulting in widespread cracks in the film during the evaporation and annealing process [33]. Strain develops in the film because it is bonded to the substrate during the evaporation process [41]. Compressive or tensile stresses can then develop in the films because of different thermal expansion between the substrate and the film [41,42]. Once these stresses become too large, the film starts to crack and it becomes fragile. Typically, film delamination is attributed to compressive stresses while surface cracks are associated with tensile stress [43,44].

Several research groups have investigated different methods to avoid the formation of defects in the preparation of thick titania films. Carotta et al. showed that slowing the evaporation rate by polymerizing the solvent helped reduce the formation of cracks in titania films up to 10 μm thick [33]. Ito et al reported a repetitive coating technique to make $\sim 20 \mu\text{m}$ titania films by sintering multiple layers while the substrate was hot [34]. However, delamination and film cracking still readily occurred during solvent evaporation. In a similar approach, Halme et al prepared 3-22 μm thick films by depositing, drying, and mild pressing the TiO_2 film at 100 kg/cm^2 ; multiple cycles were used to build the film with a final press of 1000 kg/cm^2 [7]. However, some researchers have found that it is difficult to control the thickness and uniformity of the titania film prepared by this approach. For this reason, Grinis et al filled the void space between particles with a non-polar volatile liquid to maintain a uniform pressure on the particles during compression [45]. Although $\sim 25 \mu\text{m}$ thick titania films were prepared, numerous heating and pressing cycles were required.

A simple method for preparing thick and robust ($> 15 \mu\text{m}$) TiO_2 films on conducting substrates with minimal defects remains elusive. In this chapter, I use the simple doctor blade technique [39] to spread a sol onto substrates for the preparation of $\sim 25 \mu\text{m}$ thick films of titania. By controlling the evaporation of the solvent and the temperature cycling (heating and cooling rates), the stresses that cause film defects are reduced. This technique is applied to titania films of various thicknesses on both FTO- and ITO-coated glass substrates. The final titania films are stable and have significantly lower defect densities than films prepared by the conventional approach, i.e., without controlled evaporation or temperature cycling. These anatase titania films are utilized as the photoanode in dye-sensitized solar cells and show improvements in short-circuit current, open-circuit voltage and device efficiency.

Experimental Section

Materials. A paste containing ~ 18 wt % nanocrystalline titanium dioxide (Ti Nanoxide T/SP) was obtained from Solaronix [46]. According to the manufacturer, the size of the titania particles is 13 nm. ITO and FTO on glass substrates were obtained precut from Thin Film Devices, Inc. and had conductive film thicknesses of $450 \pm 15 \text{ nm}$ and $300 \pm 50 \text{ nm}$, and sheet resistances less than 5 and $10 \Omega/\text{cm}^2$, respectively. The surface roughness of the films was reported to be between 0.22-0.33 %. The optical transmission was 75 % and 78 % (measured at 550 nm) for FTO and ITO, respectively.

Deposition of TiO_2 film. Impurities were removed from the surface of the ITO and FTO substrates prior to TiO_2 deposition by sonicating in soapy de-ionized water, acetone and ethanol for 20 min each. Titania films of various thicknesses (7, 10, 20, and $25 \mu\text{m}$) on conductive glass were prepared by using one or more layers of adhesive 3M

Scotch® tape. The thickness of one tape layer is about 50 μm and typically results in a ~10 μm film after annealing. A variety of processing conditions were used to prepare titania films, as shown in Table 3-1 and Figure 3-1. The first step was to spread the titania paste onto the substrate using a doctor blade, as shown in Figure 3-1a. Three titania films with diameters of 7 mm (surface area of 0.38 cm^2) were deposited on a single ITO or FTO substrate. The adhesive tape was gently removed before sintering, leaving little residue on the glass.

Sintering of film. The film was sintered with either an ultra-high vacuum tube furnace (Barnstead type 79300 Thermolyne) or a high vacuum oven (Barnstead 3608), which have minimum pressure ratings of 8.0×10^{-3} and 1.3 kPa, respectively. The vacuum level was controlled by bleeding nitrogen (tube furnace) or air (high vacuum oven) into the chamber. As shown in 3-1b, sintering of the film was done in two stages at constant pressure ranging from 5.3×10^{-2} to 101.3 kPa. The heating rate (dT_i/dt) to each temperature set point (T_i) was controlled as well as the sintering time (t_i) at each stage of the heating cycle. Films were first placed in the vacuum chamber and then heated once the pressure was achieved. The heating rate to the first set point (dT_1/dt) is low (2 – 5°C/min) to prevent film failure due to rapid solvent evaporation. All films were cooled by convection at the same pressure.

Annealing of the film. Titania films sintered at lower pressures were discolored, likely due to a deficiency of oxygen in the titania [47]. However, the films became transparent by annealing at atmospheric pressure on a hot plate. The annealing rate was 28.3°C/min to a temperature of 450°C. Annealing time at this temperature ranged from 40 to 105 min depending on initial film color; the time required to achieve

transparent films was longer for darker films. After the films were transparent, the annealed films were cooled at a rate (dT_3/dt) that ranged from -1 to $-100^{\circ}\text{C}/\text{min}$, as shown in Figure 3-1d and Table 3-1.

Characterization techniques. X-ray diffraction (XRD Philips APD, Cu source) was used to verify the formation of anatase titania after annealing. Scanning electron microscopy images (JEOL JSM 6400) and profilometry were used to determine film thickness. Raman spectroscopy (Renishaw Invia Bio Raman with excitation from a 785 nm diode laser) was used to probe film strain and confirm the formation of anatase titania. Optical microscopy (Nikon Optiphot) equipped with a digital camera (Amscope MD800) was used to assess the defects within the films. Six images were taken for each of the three titania films on a substrate at each stage of film preparation. RGB/8 images were converted to black and white using Adobe Photoshop to estimate the defect density using the pixel count.

First, the high filter pass feature was used to improve the contrast of film defects. The threshold value (a tool to shift image coloration between black and white) was then adjusted to reflect the actual image defect density. The mode of the image was next changed to Black and White. Therefore, the color density was forced to black and white and a histogram plot obtained the relative amount of pixels associated with each. The defect density was defined as the ratio of pixels from film defects to the total pixel count. In addition, the surface area of the film was varied (0.38 , 1 , 2 , and 3 cm^2) for titania films on FTO (sintered at 5.3×10^{-2}) and found to have minimal changes to the defect density (7.7, 3.1, 5.1, and 2.9 %, respectively), yielding an average of 4.7 ± 2.23 % for all film surface areas.

DSSC device fabrication. The titania films are impregnated in 3.0×10⁻⁴ M solution of the N-749 dye in acetonitrile and t-butanol (1:1 vol %) for 24-168 h. Counter electrodes are painted with Platisol (Solaronix) using a brush and fired in a tube furnace at 400°C for 10 min. A 40 μm thick surolyn spacer (DuPont) was cut and placed between the electrodes and the electrolyte was injected into the cell by capillary action. The current voltage characteristics of the prepared DSSC were measured under simulated AM 1.5 solar light using a source meter (VersaSTAT 3 type from Princeton Applied Research) and a solar simulator (Solar Light Co.). Open circuit voltage decay measurements are used to assess the recombination processes in DSSCs [48]. After full sun illumination on the DSSC at open circuit (for 5 sec), illumination is shut off and voltage decay is measured with time. The voltage decay is fit to a decay function and the derivative is evaluated at (t = 30 sec) to calculate electron lifetime from equation (3-1):

$$\tau_n = \frac{k_B T}{e} \left(\frac{\partial V}{\partial t} \right)^{-1} \quad (3-1)$$

where KB is the Boltzmann constant, T is temperature and e is the electron charge. The parameter KBT/e is thermal voltage, which is 0.026 V at room temperature.

Results

Characterization of titania films. Scanning electron microscopy was used to measure the thickness of titania on FTO and ITO substrates. As shown in Figure 3-2, the films are uniform with a maximum thickness of ~ 25 μm. X-ray diffraction (XRD) was used to determine the final phase of titania formed at different processing conditions. Figure 3-3 shows the XRD peaks for titania films sintered at atmospheric pressure

(101.3 kPa) and vacuum (8.0×10^{-3} kPa). XRD peaks between 20 and 70 degrees correspond to anatase peaks, confirming that both films are anatase titania. The XRD also shows that the particle size of the titania does not change when sintered in vacuum. The Raman spectra of the titania films in Figure 3-4 show peaks at 400, 514 and 640 cm^{-1} . These peaks are known to correspond to the anatase phase of titania. This data also shows that the phase does not change with film thickness. Furthermore, there are no peak shifts in the spectra that are associated with strain in the film [41,49].

Table 3-1 presents a summary of the results for each processing condition. Control samples of ITO and FTO substrates (i.e., no titania film) show no defects, confirming that defects are due to titania film formation. In addition, 20 μm titania films on ITO and FTO were prepared at atmospheric pressure and annealed directly to 450°C for comparison. These control samples had defect densities of 38.3 and 14.2 %, respectively. The defect density of each film was measured at each stage of the process. The most critical steps for minimizing the defect density were found to be the sintering pressure and annealing cooling rate. In general, FTO films have lower defect densities than ITO substrates. For example, under optimized conditions, the defect densities for 20 μm thick titania are 2.5 and 7.8 % for FTO and ITO substrates, respectively.

Effect of sintering conditions on defect density. The optical images in Figure 3-5 show the effect of the sintering pressure on the defect density of the titania films. The films show a significant amount of defects at atmospheric pressure. However, the amount of defects steadily decreases as the sintering pressure is lowered. These changes in defect density are summarized in Figure 3-6 for the titania films on both FTO

and ITO substrates. The defect densities after sintering of titania films on FTO and ITO substrates decayed exponentially as the sintering pressure decreased; defect densities ranged from 0.4 – 15.0 and 0.1 – 12.6 % for FTO and ITO substrates, respectively. A significant increase in defect density was seen for titania on both FTO- and ITO-based substrates after the annealing step. However, the effect of the sintering pressure is still observed in the defect density of titania on FTO substrates. The films prepared at the lowest pressure had a final defect density of 2.5 %. On the other hand, the final defect density of titania on ITO was nearly constant, despite the significant differences in defect density after sintering. Although the defect density was weakly dependent on pressure, controlling the sintering step for titania on ITO does significantly improve the defect density from the control sample (16.3 vs. 38.3 %, see Table 3-1). These differences indicate that the slower heating rate during controlled sintering of titania films on ITO helps reduce the defect density. Setting the heating rates and the temperature set points slightly higher during sintering at the lowest pressure of 5.3×10^{-2} kPa had minor changes to the defect density of titania films on ITO and FTO, respectively (see Table 3-1).

Effect of annealing conditions on defect density. Figures 3-7 and 3-8 show the effect of the cooling rate (dT_3/dt) after the films sintered at low pressure are annealed at 450°C. While the defect density associated with the titania films on FTO was constant within experimental error, the titania films on ITO had defect densities more sensitive to this processing step. The defect density decreased from 21.9 to 7.8 % as the cooling rate (dT_3/dt) was reduced from –100 to –1°C/min.

Discussion

The results indicate that the mechanisms of defect formation in titania films are different on ITO and FTO substrates. The critical step for maintaining defect-free films of titania on FTO is the sintering step, which is highly dependent on the sintering pressure. While lower pressure improved defect density, a majority of the benefits can be achieved at a pressure of 20 kPa, as seen in Figure 3-6a. The reduced pressure and controlled heating rate during sintering offers some benefits to the titania films prepared on ITO; however, the cooling rate from the annealing step was the most crucial step in determining the final defect density.

The formation of defects or cracks in the film during heating and cooling are associated with compressive or tensile stresses that build in the film because of differences in thermal expansion between the film and substrate. The thermal expansion coefficients of the film and substrate should be comparable so they can expand and contract together to avoid mechanical failure from the stresses. The consistent trend of defect density with sintering pressure shown in Figure 3-6 for titania films before and after annealing indicates that defects formed during the sintering step propagate across the film once it is subjected to stronger stresses during cooling. Therefore, the forces that generate defects in the titania films occur at the initial stages of the sintering process.

Titania films sintered at low pressures on both ITO and FTO substrates show significant decreases in defect density after the sintering step (circles in Figure 3-6). These changes indicate that the stresses in titania films on both substrates has been reduced at low pressure. Jagtap et al. have shown that the thermal expansion coefficient of anatase titania at low pressures can be approximately twice the values at

atmospheric pressure [50]. Therefore, the sintering in vacuum could allow the titania film to match the thermal expansion of the ITO or FTO substrate better, reducing the stresses generated in the film during sintering. This conclusion is supported by the fact that titania films still show a dependency on pressure after annealing (squares in Figure 3-6), indicating that this step has helped to reduce the stresses within the film.

Although improvements to the defect density of titania on ITO substrates are observed from thermal expansion differences at low pressure, these films still have a significant amount of residual stress that is generated in the film during sintering. This stress is released during the cooling step of the annealing process, causing widespread defects across the film. For this reason, the heating and cooling steps become much more important for titania films on ITO. This effect is first observed by comparing (see Table 3-1) the titania films prepared at atmospheric pressure on ITO with either a slower (controlled) or faster heating rate (control sample). The slower heating rate allows the stresses generated within the film to relax during sintering. The lower stored stresses within the film after sintering results in less defects created by the subsequent release of the stress during cooling. Similarly, the slower cooling rates after annealing provide more time for the stresses generated within the film to be dissipated before they generate defects or cracks, as shown in Figure 3-8.

These results provide a guide for preparing thicker titania films with minimal defects. It is clear that a low pressure and slower heating rate should be maintained during sintering to reduce the defect density generated within the film. The cooling rate was also controlled (chosen to be $-1^{\circ}\text{C}/\text{min}$) for ITO-based films because of the strong dependency of the cooling rate after annealing on defect density. These conditions

yielded 25 μm titania films on ITO and FTO with defect densities of 22.8 and 6.0 %, respectively (see Table 3-1). Interestingly, the defect density on FTO substrates was found to be almost linearly dependent on the titania thickness (see Table 3-1).

Finally, DSSCs were fabricated using the titania films prepared under controlled sintering and annealing as the photoanode. The short-circuit current and efficiency steadily improve as the thickness of the titania increases from 7 to 20 μm , which is attributed to the additional surface area of the device. As shown in Figure 3-9, the titania fabricated under vacuum yield better device characteristics than the standard method for making photoanodes (control). The titania photoanodes fabricated under vacuum have higher short-circuit current and open-circuit voltage but lower fill factors. The vacuum pressure used to prepare the photoanodes also has an effect on the device characteristics, as seen in Figure 3-9b-f. The best performance is seen at intermediate vacuum levels. These results indicate that the lowest pressures used to make the photoanode are good for minimizing defect density but not optimizing device performance. It is likely that the lowest pressures reduce the porosity of the film, see Figure 3-10. Films with lower porosity may prevent adequate impregnation of the photoanode with dye, resulting in more back reactions between the titania and electrolyte. This conclusion is supported by the fact that the lowest pressure (5.3×10^{-2} kPa) has about the same open-circuit voltage as the highest pressure (71.3 kPa) but lower short-circuit current and shorter electron lifetime. Similar behavior is observed with DSSCs made with 10 μm films, see Table 3-2. Further improvements to device efficiency may be possible if better dye impregnation can be achieved, which is discussed in chapter 5.

Conclusionary Findings

TiO₂ films were prepared on transparent conducting oxide (TCO) substrates using a simple deposition technique with controlled sintering and annealing conditions. XRD and Raman spectroscopy confirmed the formation of anatase titania films after the annealing step. Stresses generated within the film during sintering and annealing cause defects or cracks to form within the film. These defects are initiated during the sintering step and continue to propagate once the film is subjected to stronger stresses during cooling. Reducing the stresses within the film results in better quality films that can be used for various photo-applications. Sintering the titania films at low pressures reduces the stresses on both ITO and FTO substrates. The effect is more prominent in titania films prepared on FTO, resulting in significantly lower defects in the films. The preparation of defect-free titania films on ITO requires further control of the heating and cooling steps. Titania films up to 25 µm thick with minimal defects could then be prepared on both ITO and FTO substrates by minimizing the stresses generated during film preparation. Defect-free films of titania on FTO were used as the photoanode in DSSCs. The photoanodes prepared under vacuum had better overall device characteristics than those made by the standard method. Therefore, the larger surface area provided by the thicker films increased the efficiency of the cells. The pressure during sintering also affected the device performance, which was attributed to lower dye coverage because of porosity changes.

Table 3-1. Experimental conditions for preparing thick, defect-free titania films on ITO and FTO substrates.

TCO	Thickness	Sintering								Annealing		
		(μm)	dT_1/dt	T_1	t_1	dT_2/dt	T_2	t_2	P	Defect density	dT_3/dt	Defect density
			($^{\circ}\text{C}/\text{min}$)	($^{\circ}\text{C}$)	(min)	($^{\circ}\text{C}/\text{min}$)	($^{\circ}\text{C}$)	(min)	(kPa)	(%)	($^{\circ}\text{C}/\text{min}$)	(%)
ITO	20	–	–	–	–	–	–	–	–	–	–10	38.3
FTO	20	–	–	–	–	–	–	–	–	–	–10	14.2
ITO	20	2.4	120	1	2	220	30	101.3	12.5	–10	26.1	
ITO	20	2.4	120	1	2	220	30	71.3	12.6	–10	18.9	
ITO	20	2.4	120	1	2	220	30	34.7	2.2	–10	16.3	
ITO	20	2.4	120	1	2	220	30	21.3	0.8	–10	16.7	
ITO	20	2.4	120	1	2	220	30	5.3×10^{-2}	0.1	–10	17.7	
FTO	20	2.4	120	1	2	220	30	101.3	15.0	–10	15.2	
FTO	20	2.4	120	1	2	220	30	71.3	8.5	–10	9.6	
FTO	20	2.4	120	1	2	220	30	34.7	2.7	–10	5.7	
FTO	20	2.4	120	1	2	220	30	21.3	0.7	–10	4.2	
FTO	20	2.4	120	1	2	220	30	5.3×10^{-2}	0.4	–10	2.5	
ITO	20	5	180	15	10	450	30	5.3×10^{-2}	0.2	–10	14.0	
FTO	20	5	180	15	10	450	30	5.3×10^{-2}	1	–10	7.7	
ITO	20	5	180	15	10	450	30	5.3×10^{-2}	0.3	–1	7.8	
ITO	20	5	180	15	10	450	30	5.3×10^{-2}	0.5	–100	21.9	
FTO	20	5	180	15	10	450	30	5.3×10^{-2}	0.8	–1	3.5	
FTO	20	5	180	15	10	450	30	5.3×10^{-2}	0.4	–100	9.1	
ITO	25	5	180	15	10	450	30	1.2×10^{-2}	–	–1	22.8	
FTO	7	5	180	15	10	450	30	5.3×10^{-2}	–	–10	1.9	
FTO	10	5	180	15	10	450	30	5.3×10^{-2}	–	–10	2.7	
FTO	25	5	180	15	10	450	30	8.0×10^{-3}	–	–10	6.0	

Table 3-2. Efficiency of DSSCs made with 10-20 μm titania films on FTO substrates sintered at varied pressures at 450°C. The films are impregnated in 3.0×10^{-4} M of N-719 in ethanol for 30 h.

Pressure (kPa)	Thickness (μm)	Isc (mA/cm 2)	Voc (V)	FF	Efficiency (%)	τ (s)
101.3	20	4.83	0.62	0.6	1.8	0.851
71.3	20	7.78	0.68	0.43	2.27	1.786
34.7	20	10.1	0.76	0.34	2.62	0.121
5.3×10^{-2}	20	6.16	0.68	0.46	1.92	0.080
101.3	10	1.37	0.58	0.52	0.42	0.809
5.3×10^{-2}	10	3.52	0.62	0.65	1.43	0.019

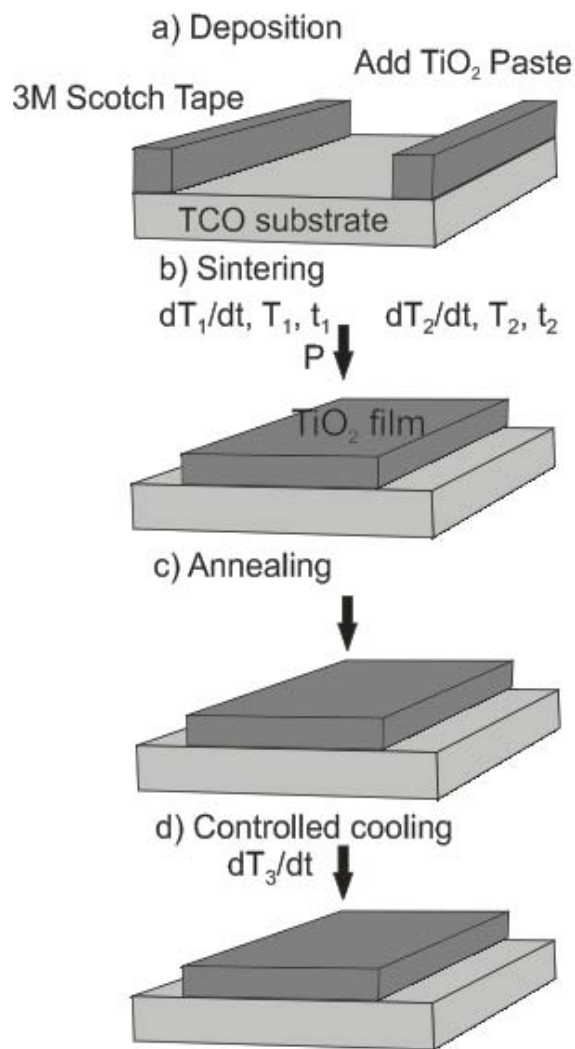


Figure 3-1. The preparation steps for making thick titania films on transparent conductive oxide (TCO) substrates. Titania is deposited using the doctor blade technique (a), followed by sintering at pressures ranging from 8.0×10^{-3} to 101.3 kPa (b), annealing at 450°C (c), and controlled cooling rates ranging from -1 to $-100^\circ\text{C}/\text{min}$ (d).

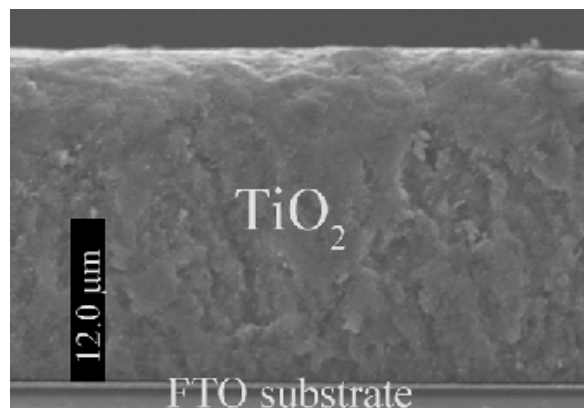


Figure 3-2. SEM image of titania film (~25 μm thick) sintered at 8.0×10^{-3} kPa and 450°C and cooled at 10°C/min.

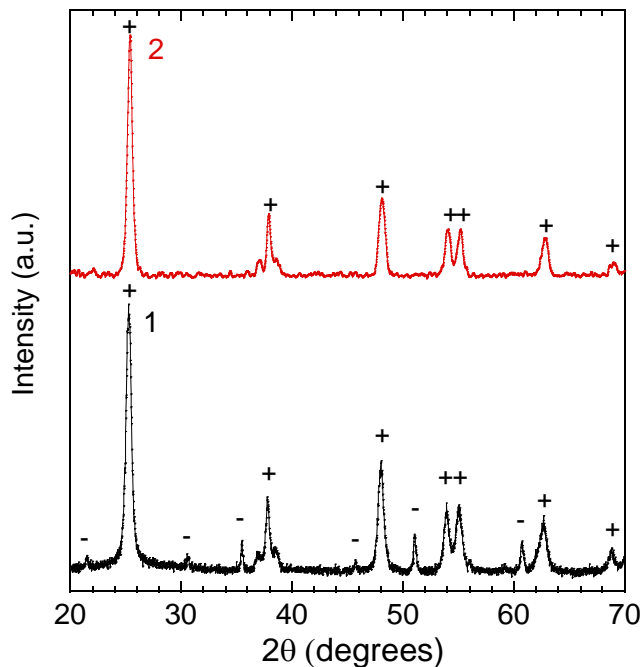


Figure 3-3. X-ray diffraction of 20 μm thick titania films annealed at atmospheric pressure at 450°C on an ITO substrate (1) and sintered in vacuum at 220°C at 8.0×10^{-3} kPa on a FTO substrate (2). The peaks correspond to anatase titania (+) and ITO (-). In (2), the titania film was removed from the FTO substrate so that only titania peaks were observed.

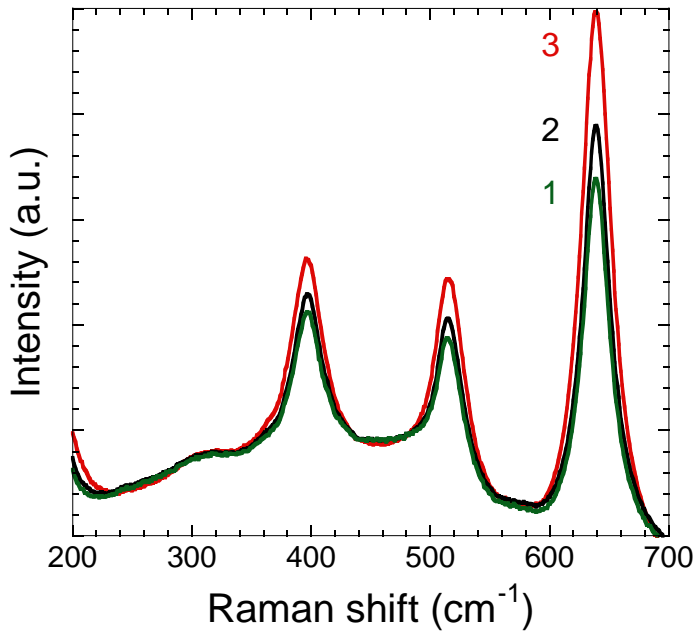


Figure 3-4. Raman spectra of 7 (1), 10 (2) and 25 (3) μm titania films on FTO substrates. The peaks at 400, 514 and 640 cm^{-1} confirm the formation of anatase titania and the spectra show no changes in position associated with strain.

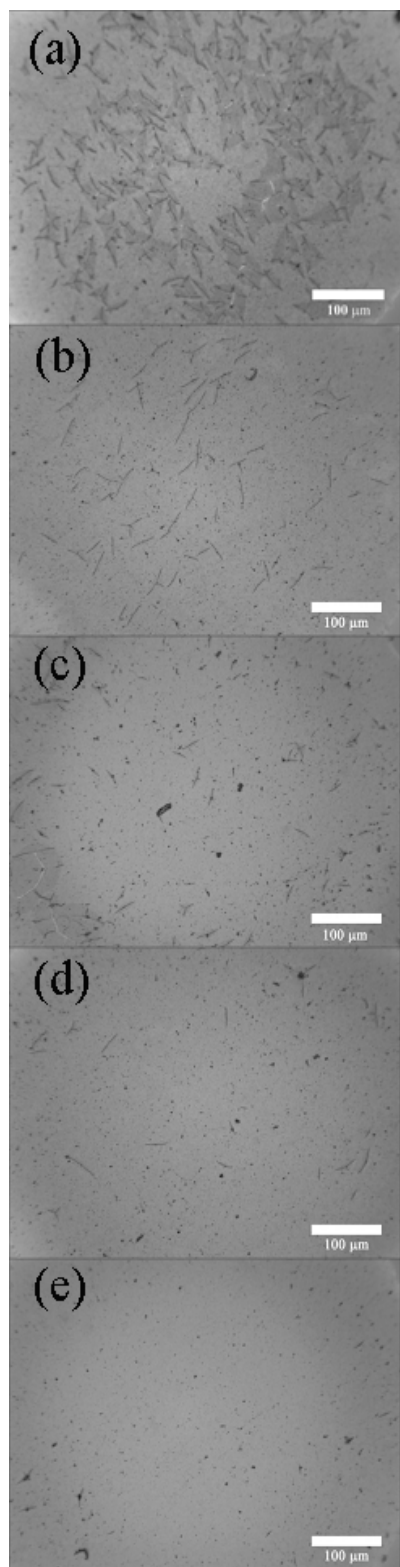


Figure 3-5. Microscopic images of the final titania films on FTO, which were sintered at 220°C and a pressure of 101.3 (a), 71.32 (b), 34.66 (c), 21.32 (d), and 5.3×10^{-2} (e) kPa. The dark regions in the images are defects.

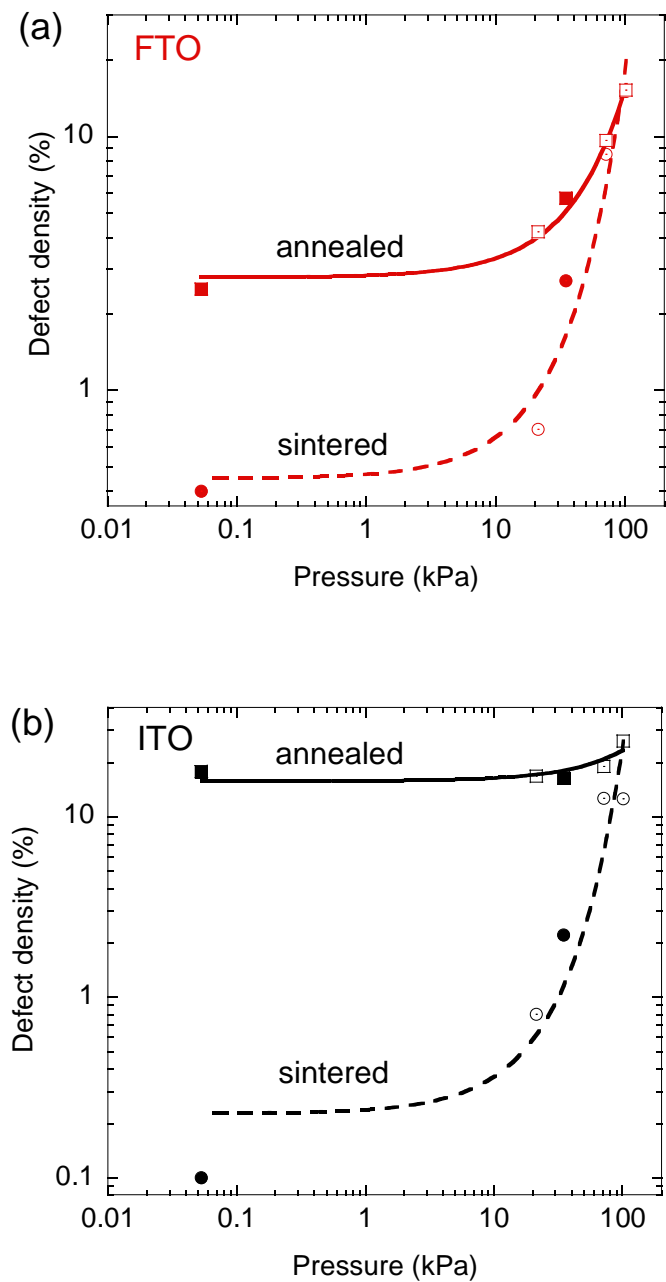


Figure 3-6. The effect of sintering pressure on the defect density of titania films on FTO (a) and ITO (b). The films were prepared using a sintering temperature of 220°C and a cooling rate of -10°C/min. The circles and squares indicate defect densities after sintering and annealing, respectively. The shaded and open symbols correspond to sintering in the tube furnace and vacuum oven, respectively. The lines show exponential fits to the data.

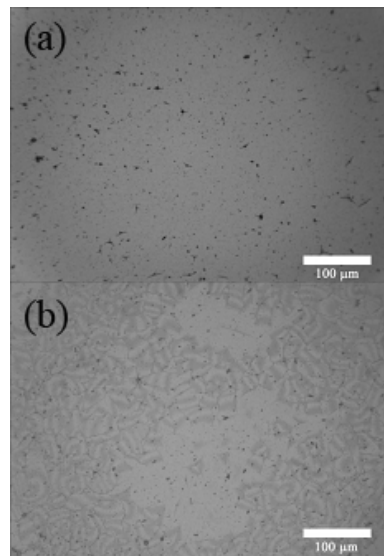


Figure 3-7. Microscopic images of the final titania films on FTO (a) and ITO (b), which were sintered at 450°C and 5.3×10^{-2} kPa and then cooled at a rate of –1°C/min. The defect densities of these films are 3.5 and 7.8 %, respectively.

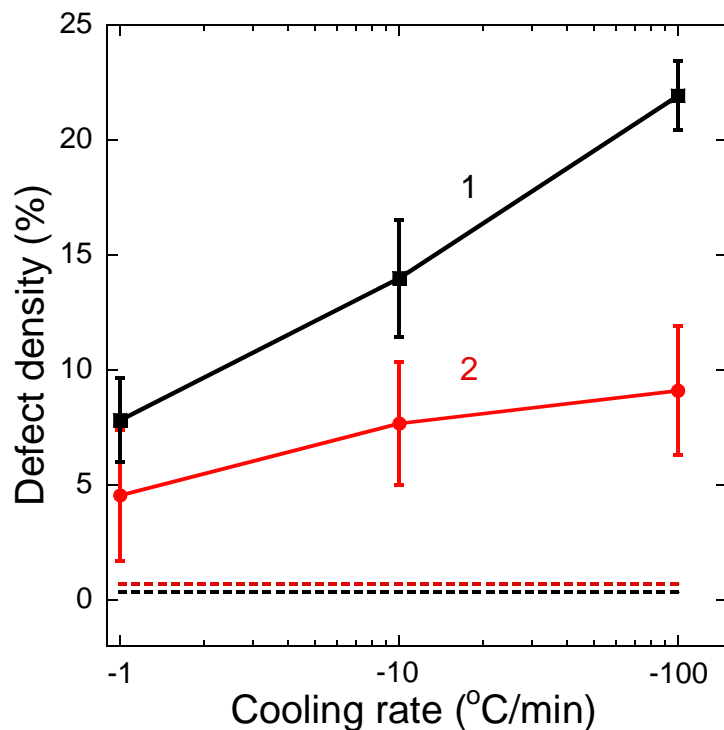


Figure 3-8. The effect of the cooling rate during annealing on the defect density of titania films on ITO (1) and FTO (2), which were sintered at 5.3×10^{-2} kPa and 450°C. The dashed lines indicate the defect density after sintering.

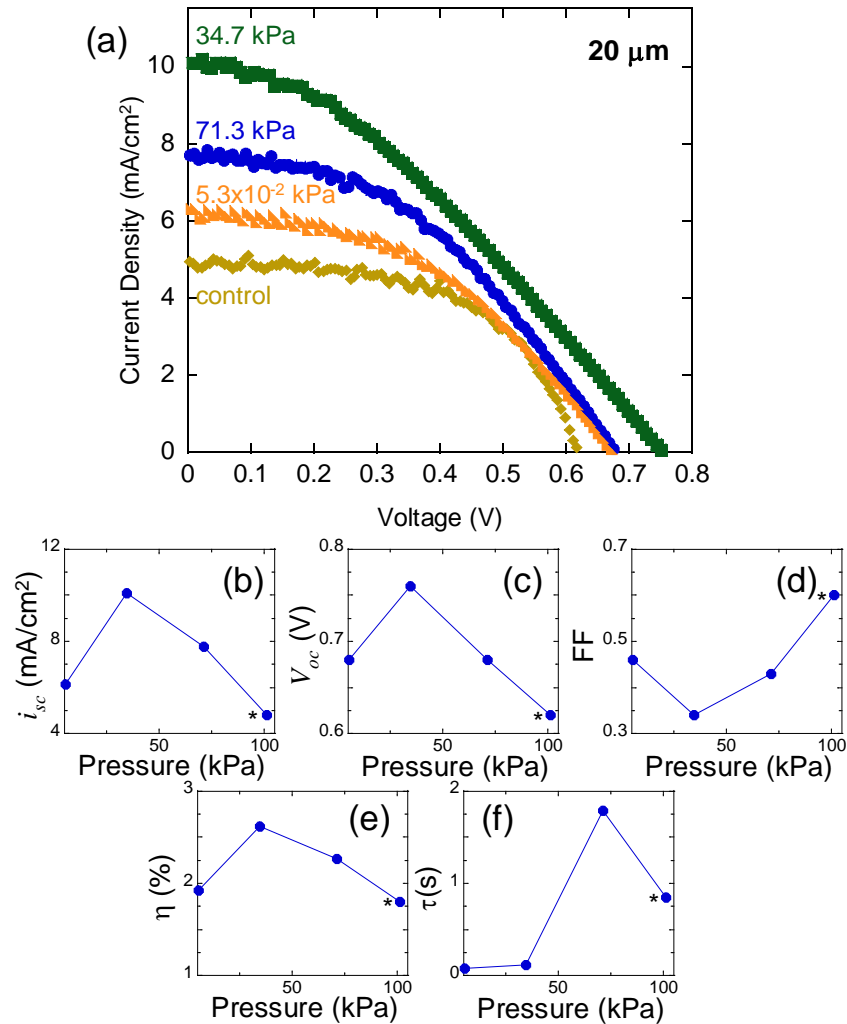


Figure 3-9. Performance characteristics of DSSCs fabricated from photoanodes sintered at different pressures compared to the standard preparation method (control). (a) Current-voltage measurements; (b) Short-circuit current; (c) Open-circuit voltage; (d) Fill factor; (e) Efficiency; (f) Electron lifetime. All titania photoanodes are 20 μm thick and the control experiment is designated by the * in (b) – (f).

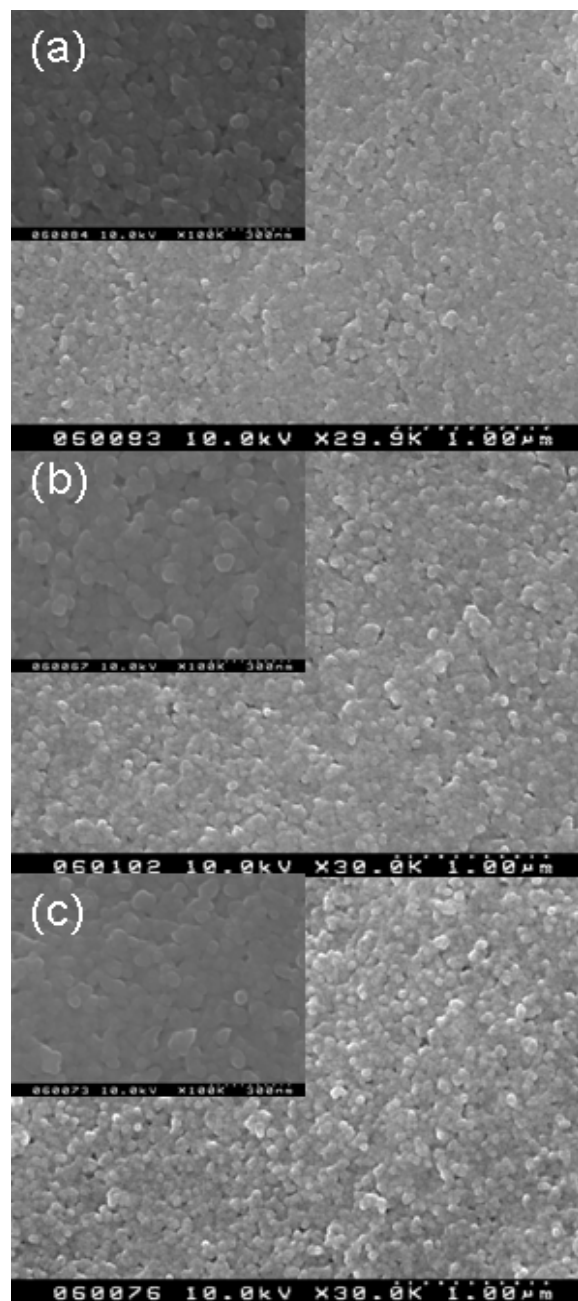


Figure 3-10. SEM images of 20 μm titania films sintered at varied pressures. The films are sintered at 101.3 (a), 34.7 (b) and 5.3×10^{-2} (c) kPa at 450°C for 30 min followed by annealing at atmospheric pressure for transparency. The films sintered at lower pressures show closer particles and lower porosity.

CHAPTER 4

NONDESTRUCTIVE MEASUREMENT OF DYE ADSORPTION ONTO TITANIA FILMS

Preliminary Remarks

Dye-sensitized solar cells (DSSCs) are not limited by the high purities and, consequently, high capital costs associated with silicon-based devices [51]. These devices are centered around a chromophore sensitizer, typically a ruthenium-based dye, that harvests photons. Photons adsorbed by the dye are excited to the lowest unoccupied molecular orbital where the electron can then be injected into the conduction band of a large band gap semiconductor, which is typically titania. A majority of the research of DSSCs has focused on the use of N-719 [bis(tetrabutylammonium)-cis-di(thiocyanato)-N,NA-bis(4-carboxylato-4A-carboxylic acid-2,2A-bipyridine) ruthenium (II)] or N-749 [(2,2':6',2"-terpyridine-4,4',4"-tricarboxylate) ruthenium (II) tris (tetrabutylammonium) tris(isothiocyanate)] as the photosensitive dyes.

The impregnation of the dye into the titania photoanode occurs by soaking the matrix in a solution of the dye for several hours. The dye is adsorbed to the surface of titania by carboxylate groups which bind in different anchoring modes [52]. It is important to obtain uniform dye coverage on titania for enhanced electron transfer and low recombination. Excess dye loading can lead to multilayer formation, which cause quenching of the photoexcited electrons and reduction of charge injection. On the other hand, poor dye coverage leads to low photoactive surface area and electron trap sites.

Although the dye is critical to the operation of DSSCs, often the dye concentration is not reported or correlated to device performance. The reason for this lack of valuable information is that the dye concentration can only be obtained by dissolving the dye in a base solution, destroying the cell. This destructive method is simple but the expensive

dyes are wasted in the process. In many cases, undissolved dye remains on the films after dissolution of the titania, which is an inherent source of error in determining the concentration or dye coverage from the destructive method. This destructive method also provides no information about the uniformity of dye coverage. Finally, the fractional coverage and distribution of dye are also important parameters in models that describe the performance of DSSCs [53,54]. Obtaining accurate measurements of dye coverage that correlate to specific device performance will be important to developing more accurate models.

In this chapter, I discuss a nondestructive method to quantify the concentration of N-719 and N-749 dyes adsorbed onto titania photoanodes. The method is able to characterize the concentration in photoanodes ranging between 7 and 20 μm in thickness. Spatial profiles of dye adsorption can also be correlated to local performance. The results show that the dye coverage is often non-uniform and that excessive dye concentrations lead to lower short-circuit currents.

Materials and Methods

Materials. A paste containing ~18 wt % nanocrystalline titanium dioxide (Ti Nanoxide T/SP) as well as the N-719 and N-749 Ruthenium-based dyes [55] were purchased from Solaronix. The particle size of the titanium dioxide is reported to be 13 nm. FTO on glass substrates were obtained precut from Thin Film Devices, Inc. Acetonitile and ethanol were purchased from Fisher Scientific. Sodium hydroxide (97 %) was purchased from Sigma Aldrich.

Titania film preparation and dye impregnation. Titania films of various thicknesses were pasted onto FTO substrates, as described in chapter 3. Briefly, titania

paste is used to make 7, 10 and 20 μm thick films (surface area of 0.384 cm^2) using a simple doctor blade method. After the titania is pasted onto FTO, the films are sintered in a tube furnace (Barnstead type 79300 Thermolyne tube furnace) at a pressure of 5.3×10^{-2} kPa at 450°C for 30 minutes. The films are then annealed at the same temperature on a hot plate until they become transparent. Finally, the films are cooled to room temperature at a controlled rate of 10°C/min. This method was shown to prepare defect-free titania films for thicknesses ranging from 7 to 25 μm . Solutions of the N-749 and N-719 dyes (1.68×10^{-4} M) were dissolved in acetonitrile and ethanol, respectively. Titania films were impregnated by soaking in the dye solution for times ranging between 6 hours and 1 week.

Determining the molar extinction coefficient of the dyes in the NaOH

solution. The liquid extinction coefficient $\epsilon_{\text{dye},l}$ was obtained experimentally. N-719 and N-749 dyes are dissolved in a mixture of sodium hydroxide and ethanol (1:1 vol %). The spectra is taken for each sample by dilution with 0.5 ml of NaOH:EtOH mixture to collect absorbance of different dye concentrations. The pH of the solutions did not change in these measurements. The absorbance at the peak was plotted as a function of concentration (see Figure 4-1a and b), which yielded straight lines as expected by Beer's Law. The slope of the line was used as the molar extinction coefficient of each dye.

Measurement of molar extinction coefficients in the solid state. SEM and profilometry were used to measure the film thickness. UV-vis spectroscopy of the titania films or dye solutions were collected from 350 to 650 nm on a Perkin-Elmer Lambda 9 UV/VIS/NIR spectrometer. The spectra for dyes in the titania films were measured first.

The titania films were mounted to an X-Z translational stage (Newport) and multiple measurements (~15) of the initial and impregnated titania film were obtained. The spectra of the initial and impregnated titania films were averaged for analysis. The titania films were then dissolved in 4 mL of 0.1 M NaOH and ethanol (1:1 vol %) for 30 minutes for spectral analysis. It is worth noting that the spectra used to obtain the molar extinction coefficients were taken from a set of data that showed complete dissolution of the film and no residual dye remaining on the substrate.

Spatial profiles. The spectra for dyes in the titania films were measured in a grid by moving the X-Z translational stage across the titania film in 0.5 mm increments. Absorbance values at the peak position are collected and rescaled with values between 0 and 1 and assigned a color between blue and white, where blue corresponds to the highest concentrations. The assigned colors are used to create a square mesh to represent the concentration profile in the titania film.

The titania film was then covered with a iodide/triiodide electrolyte solution (purchased from Solaronix) in an open cell, which was completed with a platinum wire (diameter of 0.3 mm) as the working electrode. The platinum wire was used to measure the short-circuit current at local points under simulated AM 1.5 solar light using a source meter (VersaSTAT 3 type from Princeton Applied Research) and a solar simulator (Solar Light Co.). Once again, the values were scaled and assigned a color to obtain the short-circuit current profile.

Results and Discussion

The absorption spectra for N-719 and N-749 dyes in the NaOH solution are shown in Figure 4-2, respectively. The N-719 dye shows characteristic peaks at 375 and 512 nm (see Fig. 4-2a) while the N-749 dye has characteristic peaks at 397 and 586 nm

(see Fig. 4-2b). The molar extinction coefficients of each dye were determined using the 512 and 586 nm peak for N-719 and N-749 (see supplementary data), respectively, as shown in Table 4-1. The spectra for each dye red-shifts once they are adsorbed onto the titania film, as shown in Figure 4-2. For example, the peaks used to determine the molar extinction coefficients of each dye shifted to 525 and 620 nm for N-719 and N-749, respectively. Shifts in peak position can be expected because of the effect of the localized environment on the excited state [56].

Although the spectra of each dye adsorbed onto the titania has shifted, Beer's Law can still be used to measure the concentration provided there are no other optical effects that alter the transmission of light. A comparison of the absorbance for each dye measured in the NaOH solution and titania show a nearly constant ratio, as shown in Figure 4-3. The slope of the curve yields the absorbance ratio, $A_{\text{dye},l} / A_{\text{dye},s}$, where the subscripts l and s correspond to the liquid NaOH and solid titania film, respectively. $A_{\text{dye},l} / A_{\text{dye},s}$ equals ~3 and ~9 for the N-719 and N-749 dyes, respectively. The linearity of this ratio indicates that any optical effects are negligible. Therefore, Beer's Law given by equation (4-1):

$$A_{\text{dye}} = \varepsilon_{\text{dye}} \cdot l \cdot \frac{N_{\text{dye}}}{V} \quad (4-1)$$

can be applied to the absorbance of the dye in both the NaOH solution and titania films. In writing this expression, A_{dye} is the absorbance from the dye, $\varepsilon_{\text{dye},l}$ is the molar extinction coefficient of the dye, l is the path length for light, N_{dye} is the moles of dye that absorb light, and V is the volume of the medium hosting the dye. If the dye adsorbed onto the titania film is dissolved completely in the NaOH solution, then the

moles of dye in NaOH must be equal to the number of moles in the solid titania film as in equation (4-2):

$$N_{dye,l} = \frac{A_{dye,l} \cdot V_l}{\varepsilon_{dye,l} \cdot l} = \frac{A_{dye,s} \cdot V_s}{\varepsilon_{dye,s} \cdot t} = N_{dye,s} \quad (4-2)$$

where t is the thickness of the titania film.

By rearranging equation (4-2) and substituting $V_s = t \cdot a_s$, where a_s is the planar surface area of the film, an expression for the molar extinction coefficient of the dye adsorbed onto the solid titania films is obtained,

$$\varepsilon_{dye,s} = \left(\frac{A_{dye,s}}{A_{dye,l}} \right) l \left(\frac{a_s}{V_l} \right) \varepsilon_{dye,l} \quad (4-3)$$

Equation (4-3) shows that the molar extinction coefficient for the dye adsorbed onto the titania films, $\varepsilon_{dye,s}$, is a function of the constants l , a_s , V_l , and $\varepsilon_{dye,l}$, and the ratio of dye absorbance, $A_{dye,s} / A_{dye,l}$

Equation (4-3) was then used to determine the molar extinction coefficients of each dye adsorbed onto the titania films, as shown in Table 4-1. These molar extinction coefficients can be used to calculate the concentration of dye adsorbed onto the titania film. As shown in Figure 4-4, the molar extinction coefficients are able to accurately determine the amount of dye adsorbed at a variety of concentrations and film thicknesses.

Once the molar extinction coefficient is known for the dye, spatial profiles of dye adsorption can be obtained. The X-Z translational stage was used to collect the absorbance in a grid using steps of 0.5 mm. Spatial profiles show significant deviation in

the adsorption of dye across the film. As shown in Figure 4-5(a) for a 7 μm film impregnated with N-719 dye, the difference in concentration across the film can be quite significant, ranging between 4.3×10^{-6} and 1.2×10^{-5} mol cm^{-3} . The spatial distribution shows that there is a higher concentration of dye in the center of the film. Profilometry shows that the titania film thickness was higher at the center than the edges of the film (ranges between 6.2 and 6.8 μm).

This spatial technique provides valuable information about surface coverage and impregnation uniformity. This information cannot be provided in the typical destructive method and may help explain variations in DSSC device efficiency within the film. To demonstrate, the short-circuit current was probed with a platinum wire for this film along a similar grid. Comparison of parts (a) and (b) of Figure 4-5 shows that higher short-circuit current typically corresponds to intermediate dye concentrations in the film. These trends can be associated with the effect that the dye coverage has on device performance. If the dye coverage is too low, then excessive back reactions between the electrons in the titania and the electrolyte occur, reducing the current generated. On the other hand, higher concentrations of dye can influence electron transfer. Ono et al showed that DSSCs exhibited high charge transfer resistance with multilayer adsorption of dye on the surface of the photoanode [57]. Photo-excited electrons are quenched as multiple layers of the dye build up on the surface, reducing the injection of electrons into the conduction band of the semiconductor.

Concluding Remarks

The molar extinction coefficients of both N-719 and N-749 dyes adsorbed onto titania were determined. These molar extinction coefficients can be used to determine

the concentration of dye adsorbed in films of varying thickness without destroying the film. This nondestructive technique provides an accurate measurement of the dye adsorbed onto titania and can be used to relate the local concentrations with device performance through spatial profiling.

Table 4-1. Measured molar extinction coefficients for N-719 and N-749 dyes.

	N-719		N-749	
	λ (nm)	ε (L cm ⁻¹ mol ⁻¹)	λ (nm)	ε (L cm ⁻¹ mol ⁻¹)
NaOH/ethanol solution (pH =13.09)	512	12406	586	6320.5
titania film	525	6916	620	6454

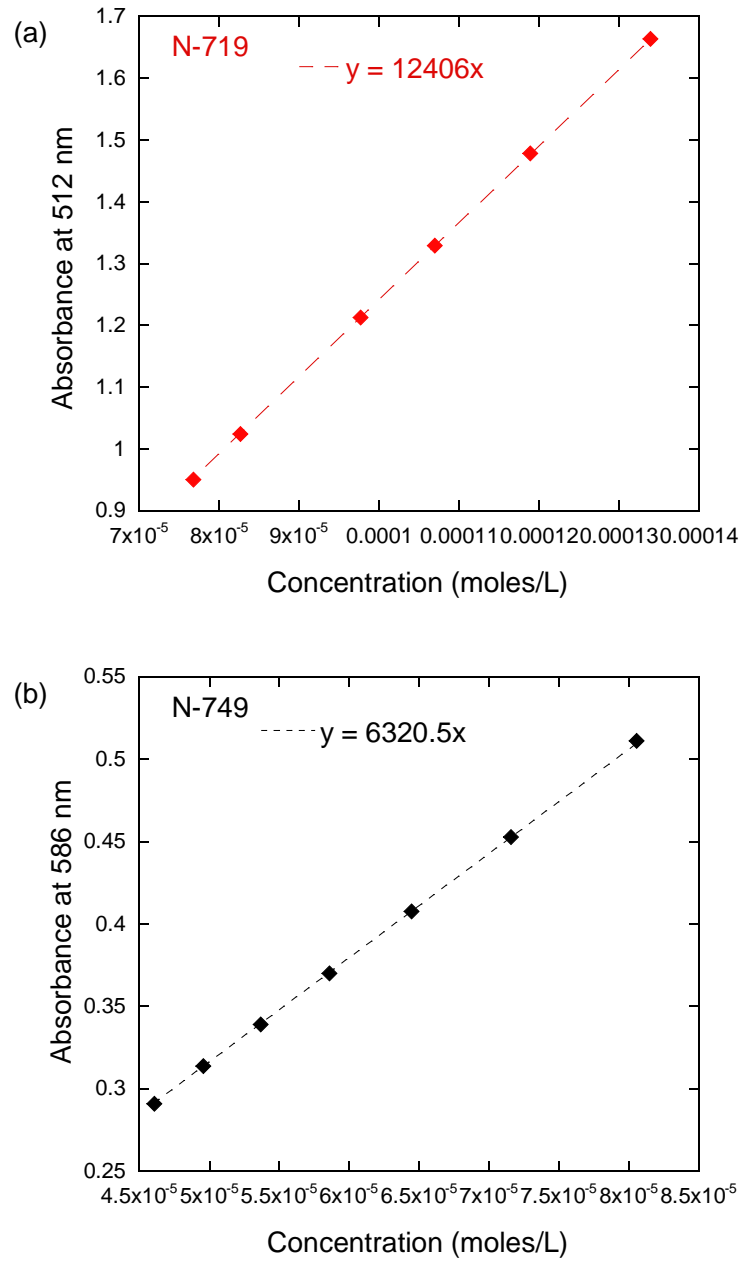


Figure 4-1. N-719 and N-749 dye extinction coefficient in NaOH. The liquid extinction coefficient was obtained experimentally using calibration data in NaOH and equation (4-1). The areas of the various thick films is $3.85 \times 10^{-5} \text{ m}^2$, l is 1 cm and the volume of the NaOH solution is $4 \times 10^{-3} \text{ L}$.

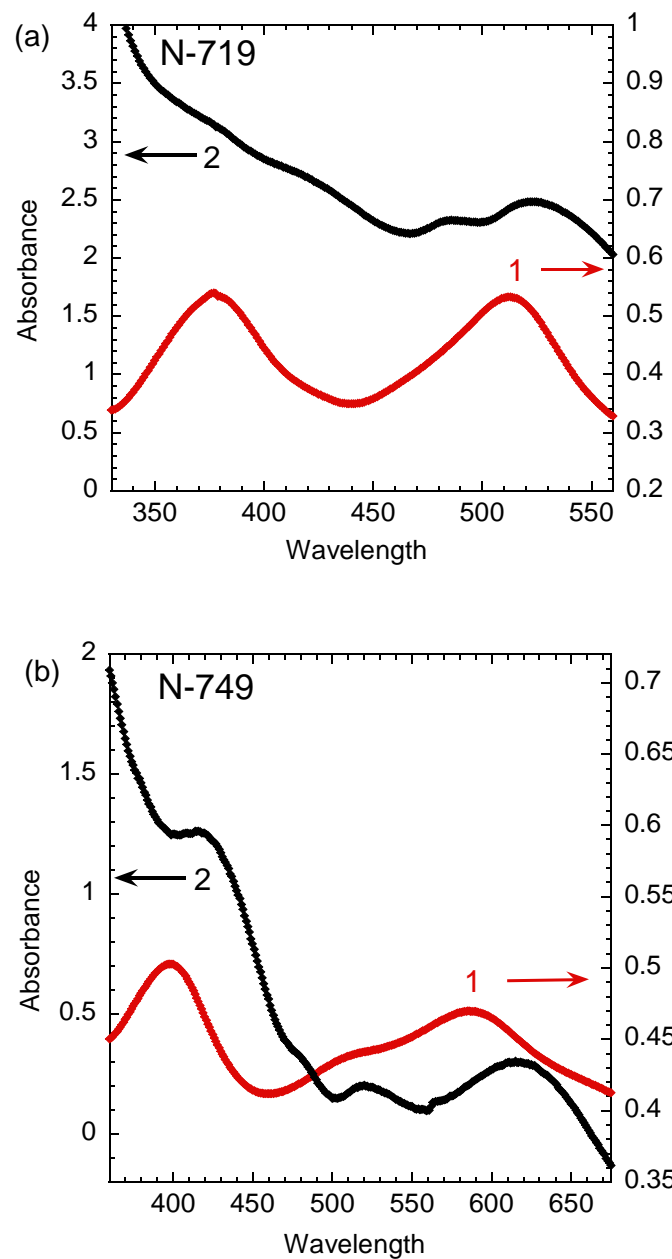


Figure 4-2. Spectroscopic peaks of N-719 and N-749 dyes in NaOH solution (a) and in solid titania (b).

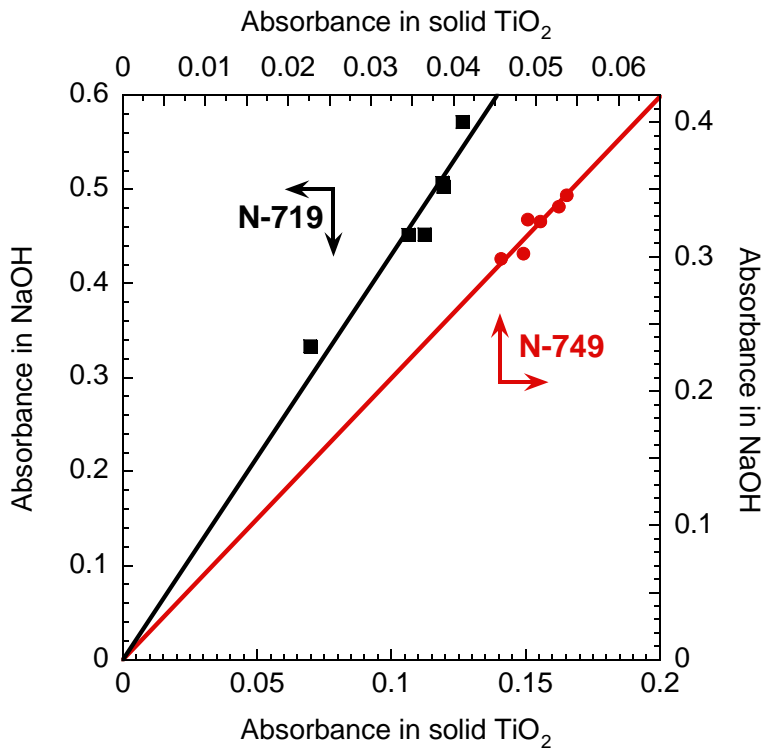


Figure 4-3. Absorbance of N-719 and N-749 dyes adsorbed onto the solid titania film or dissolved in NaOH .

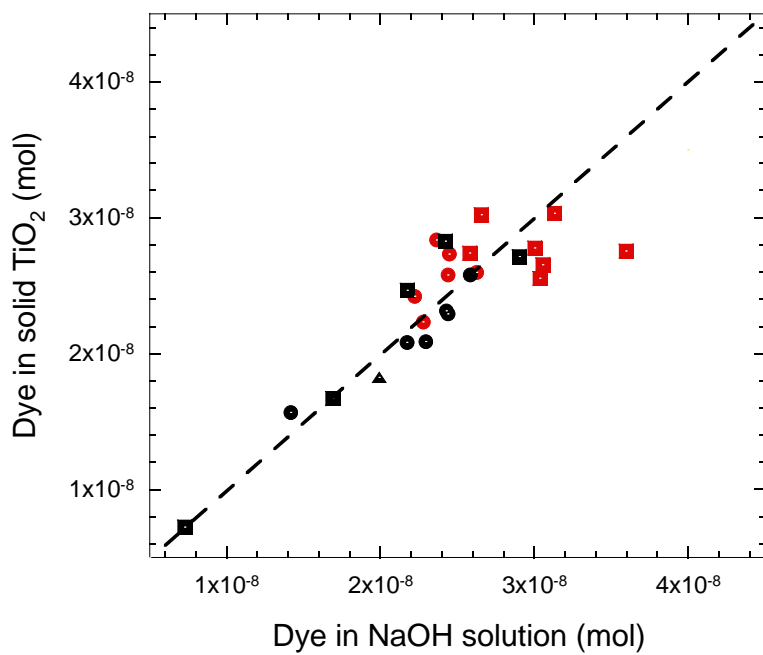


Figure 4-4. Comparison of the concentration of N-719 (red symbols) and N-749 (black symbols) dye determined by measuring the absorbance in the solid state (nondestructive) or NaOH solution (destructive) for titania films ranging in thickness from 7 to 20 μm; Symbols represent (●) 7 μm; (■) 10 μm; and (▲) 20 μm thick films. The dashed line represents equimolar values.

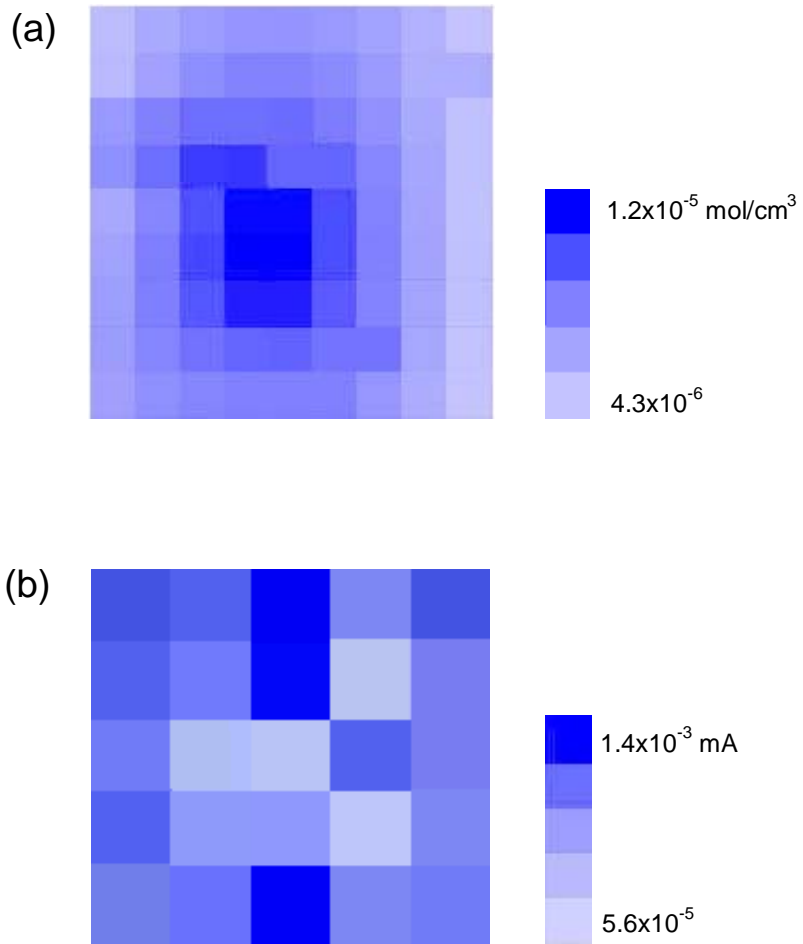


Figure 4-5. Spatial profile of N-719 dye absorption in 10 μm titania film by performing 0.5 mm step measurements using X-Z stage over a square area (a). Scale bar shows concentration ranges from 4.3×10^{-6} (white) to 1.2×10^{-5} mol/cm³ (blue). Short circuit current profile of N-719, 10 μm film. Scale bar shows short circuit current ranges from 5.6×10^{-5} to 1.4×10^{-3} mA (b).

CHAPTER 5

ENHANCING THE PHOTO ACTIVE SURFACE AREA OF DYE SENSITIZED SOLAR CELLS

Initial Remarks

The most important factor for enhancing DSSC efficiency is to increase the photoactive surface area of the semiconductor. Enhancing dye coverage for DSSCs can enhance the photon generation and electron collection efficiency. The incident photon to current conversion efficiency is given by equation (5-1)

$$IPCE(\lambda) = LHE(\lambda) \cdot \varphi_{inj} \cdot n_{coll} \quad (5-1)$$

where $LHE(\lambda)$ is the light harvesting efficiency for photons of wavelength λ , φ_{inj} is the quantum yield for electron injection from the excited sensitizer in the conduction band of the semiconductor oxide and n_{coll} is the electron collection efficiency [4]. To improve IPCE (λ) for a semiconductor material, $LHE (\lambda)$ must be increased. For a high density nanowire structure or nanoparticle film, dye uptake becomes essential in harvesting of photons and higher IPCE efficiency.

It should be stated that it is enhanced monolayer and uniform dye coverage that is required to enhance performance. Multilayer formation and poor dye coverage hinders kinetics of electron transfer. Ono el al shows formation of agglomeration of dyes molecules on TiO_2 surfaces causes high charge transfer resistance [57]. Dye aggregates cause quenching of photoexcited electrons which can prevent injection in the semiconductor, and causes recombination of electrons with the electrolyte. The electron diffusion length is the distance in which injected electrons in the conduction band of the semiconductor will travel before they will likely recombine with holes in the semiconductor, with the dye in its ground state or back-react with the electrolyte, see

Figure 5-1. The electron diffusion length is limited by dynamic competition between electron diffusion and lifetime as given by equation (5-2)

$$L_n = \sqrt{D_n \cdot \tau_n} \quad (5-2)$$

where L_n is electron diffusion length, D_n is electron diffusion and τ_n is electron lifetime. It is understood that the measured lifetime does not in general correspond to the free carrier lifetime but is rather an average of characteristic times for survival of free and trapped electrons [48]. Peter et al. showed optimum electron diffusion length for typical DSSCs to be 10 μm [58].

In order to achieve higher device efficiency, it is important to utilize thicker titania films while maintaining higher diffusion length and low recombination. Thicker semiconductor films can ideally enhance the photoactive surface area. However, poor penetration and dye aggregation in thicker films causes recombination and electron traps due to transport limitation with liquid solvents. Reduced electron diffusion coefficient and increased recombination will not allow electron diffusion length to increase beyond 10 μm .

Supercritical fluids (SCFs) have low surface tension and high diffusivities [59] and are expected to deliver dye to small pore sizes and inaccessible spaces and enhance uptake. Ogomi et al. [60] showed that dye injection in SCFs can yield 20 % increase in efficiency compared with conventional dip coating processes.

In this chapter, solubility measurements of ruthenium dyes were performed using a spectroscopic technique to confirm dye dispersion in a SCF at a range of temperatures and pressures. Dye coating of the semiconductor by wet and gas methods is investigated for up to 20 μm thick titania with different solvent mixtures including sc-

CO_2 . DSSCs are tested to obtain short circuit current, open circuit voltage, efficiency and electron lifetime.

Materials and Methods

Materials. A paste containing ~18 wt % nanocrystalline titanium dioxide (Ti Nanoxide T/SP), N-719 and N-749 Ruthenium-based dyes, as well as Iodolyte AN-50 and Platisol were purchased from Solaronix. The particle size of the titanium dioxide is reported to be 13 nm. FTO on glass substrates were obtained precut from Thin Film Devices, Inc. Acetonitrile, ethanol and t-butanol were purchased from Fisher Scientific. Surolyn was donated from DuPont Company and extruded to 40 μm thick sheets by Ran Castle Co.

Titania film preparation. Titania films of various thicknesses were pasted onto FTO substrates as described in chapter 3. Briefly, titania paste was used to make 7, 10 and 20 μm thick films (surface area of 0.384 cm^2) using a simple doctor blade method. After the titania was pasted onto FTO, the films were sintered in a tube furnace (Barnstead type 79300 Thermolyne tube furnace) at pressure in the range of 5.3×10^{-2} to 101.3 kPa at 450°C for 30 min. The films were then annealed at the same temperature on a hot plate until they become transparent [61]. Finally, the films were cooled to room temperature at a controlled rate of 10°C/min. This method was shown to prepare defect-free titania films for thicknesses ranging from 7 to 25 μm .

Dye solubility in sc-CO₂. N-749 and N-719 ruthenium dyes were dissolved in a co-solvent for solubility in sc-CO₂ [62]. The amount of co-solvent was limited to less than 5 % (vol %) with sc-CO₂. 3.0×10^{-4} M of dye in a co-solvent was injected in the volume variable view cell (purchased from Metallic Creations Co.) at a given

temperature. Then, Isco syringe pump was used to pressurize sc-CO₂ to the view cell at the desired pressure while stirring using an egg shaped stir bar to reach equilibrium. The view cell was aligned vertically with the UV-VIS spectrometer light source for UV-VIS measurements. N-719 and N-749 dyes solubility in sc-CO₂ were determined at temperatures ranging from 35 to 55°C and at pressures ranging from 100 to 400 atm. Cloud point measurements were collected at the same conditions by varying pressure at a given temperature.

Dye impregnation by dipping. 3.0×10⁻⁴ M solutions of N-719 and N-749 were prepared in ethanol and acetonitrile-t-butanol (1:1 vol %), respectively. The effect of t-butanol as a co-solvent on device performance was tested by preparing different N-719 and N-749 dip samples in ethanol-t-butanol (1:1 vol %) and acetonitrile, respectively. These films were impregnated by dipping at room temperature from 6 h to 1 week. The optimum impregnation time for the various thick films was found to vary depending on film thickness, see Figure 5-2. The 7, 10 and 20 µm films were impregnated at 24, 48, and 180 h, respectively for optimum dye coverage.

Dye impregnation by sc-CO₂. The ruthenium dye concentration in a co-solvent was increased to 30 % for film coverage. The optimum concentration of the dye in sc-CO₂ ranged from 0.50×10⁻⁴ to 0.9×10⁻⁴ M at pressures ranging from 10 to 15 MPa [63]. 7 ml of the 3.0×10⁻⁴ M solutions of N-719 and N-749 in ethanol and acetonitrile-t-butanol (1:1 vol %), respectively, was injected in the view cell. Isco syringe pump was used to deliver pressurized carbon dioxide to the view cell using a 6-way valve injection loop at 40°C and 100 atm and was allowed to reach equilibrium. Cell pressure was increased to 250 atm by injecting sc-CO₂ from the back of the view cell to maintain dye molality in the

solvent mixture. Titania films placed in the view cell were impregnated for times ranging between 1 to 1.5 h.

Characterization. Profilometry and SEM were used to measure the film thickness. Dye solubility was measured using the Perkin-Elmer Lambda 9 UV/VIS/NIR spectrometer in situ. Cloud point measurements were obtained at the operating conditions. Dye concentration was measured using a nondestructive technique instead of destructive dye adsorption in NaOH [64] as described in chapter 4. Briefly, UV-VIS spectroscopy of the titania films were collected from 350 to 650 nm on a Perkin-Elmer Lambda 9 UV/VIS/NIR spectrometer. The spectra for dyes in the titania films were measured first. The titania films were mounted to an X-Z translational stage (Newport) and multiple measurements (~15) of the initial and impregnated titania film were obtained. The spectra of the initial and impregnated titania films were averaged for analysis.

DSSC device fabrication and testing. FTO counter electrode was painted with Platisol (Solaronix) using a brush and fired in the tube furnace at 400°C for 5 min. Surolyn spacer was cut and placed between electrodes and the electrolyte was injected by capillary action. The current-voltage characteristics of the prepared DSSC were measured under simulated AM 1.5 solar light using a source meter (VersaSTAT 3 type from Princeton Applied Research) and a solar simulator (Solar Light Co.) Open-circuit voltage decay measurements were used to assess the recombination processes in DSSCs [48]. When illumination was shut off at open circuit, electrons transferred by recombination only and voltage decay was related to electron lifetime. The voltage

changes were fit to a decay function and the derivative was used to calculate electron lifetime using equation (5-3):

$$\tau_n = \frac{k_B T}{e} \left(\frac{\partial V}{\partial t} \right)^{-1} \quad (5-3)$$

where K_B is Boltzmann constant, T is temperature and e is electron charge. $K_B T/e$ is thermal voltage and at room temperature is 0.026 V. It has been shown [3,65,66] that the recombination reaction in DSSCs is nonlinear and is of second order with respect to concentration of electrons, e.g. U is proportional with n^2 . In general,

$$U = -k_r n^\beta \quad (5-4)$$

where U is the rate of recombination, K_r is the net recombination rate constant, n is electron concentration and β is recombination order. The recombination order can be calculated using equation (5-5) [48]:

$$\beta = 1 + \frac{d}{dt} (\tau_n) \quad (5-5)$$

It has been suggested that the value of β increases when interfacial potential drop increases in DSSCs. Deviation of the β value toward unity suggests reduction of electron recombination.

Results and Discussion

Solubility using sc-CO₂. Ruthenium dyes have low solubility in sc-CO₂ with up to 5 % (vol %) of ethanol as a co-solvent. UV-VIS spectroscopy measurements at different pressures and temperatures showed dye solubility is in the range of $\sim 10^{-7}$ moles, see Figure 5-3. This was attributed to the weak solvent strength of the non polar carbon dioxide. Cloud point measurements confirmed solubility of dye increases at higher

pressures and lower temperatures, see Figure 5-4a. This shows that solubility is proportional with carbon dioxide density; see Figure 5-4b.

Dip vs. sc-CO₂ impregnation. 7, 10 and 20 µm thick titania films on FTO substrates, impregnated by dip and sc-CO₂ methods in both N-719 and N-749, were probed for film concentration using the nondestructive technique, described in chapter 4. The sc-CO₂ method showed comparable absorbance to the dip methods with much lower time scales. Effective coverage with sc-CO₂ can be achieved in 1-1.5 h compared with up to 180 h for the dip method. The films impregnated in the alternative co-solvent mixture for N-719 in ethanol-t-butanol showed higher absorbance than those in ethanol, see Figure 5-5a. The films impregnated in N-749 in acetonitrile showed comparable absorbance to those in acetonitrile-t-butanol, see Figure 5-5b.

N-749-DSSC device performance. Current-voltage characteristics of DSSCs with photoanodes of different thicknesses prepared at 5.3×10^{-2} kPa and impregnated in N-749 using different solvent mixtures are shown in Figure 5-6a. The increase in short circuit current in the thicker films for both dip and SCF films was due to higher photoactive surface areas. The fill factors ranged from 0.54 to 0.58 for all the cells, see Figure 5-6b. The three (co)solvents mixtures used with N-749 showed increase in efficiency from 2.2-3.5 % to 4.7-5.8 % going from 7 to 10 µm in film thickness; see Figure 5-7a. The higher efficiency of the DSSCs prepared with acetonitrile-t-butanol was likely due to reduced recombination. However, when film thickness was increased to 20 µm, the efficiency of the two liquid (co)solvent mixtures dropped to 2.5-3.5 %. This was due to poor penetration of solvents in the small pore sizes reducing coverage, electron generation and collection efficiency. The 20 µm SCF showed lower absorbance, see

Figure 5-5b. This was likely due to better coverage of the film using sc-CO₂ with a monolayer of dye on most of the film surface. The relatively lower electron lifetime indicate overall better coverage of the thicker films; see Figure 5-7b. The thicker films gave highest efficiency of 6.57 % due to improved absorption of light between 700-900 nm [67], which N-749 is capable of sensitizing efficiently.

N-719-DSSC device performance. Current-voltage characteristics of DSSCs with photoanodes of different thicknesses prepared at 5.3×10^{-2} kPa and impregnated in N-719 using different solvent mixtures are shown in Figure 5-8a. N-719 in ethanol gave efficiency around 1.77 % for all the thicknesses, see Figure 5-8b. N-719 in ethanol and sc-CO₂ gives 4.83 % at 7 μm. However, at higher thickness of 10-20 μm efficiency drops to around 1.5 %. In a similar trend but with much higher efficiency, N-719 in ethanol-t-butanol gave 9.43 % at 7 μm and dropped to 6.42 % at 20 μm. This increase in efficiency for the co-solvent mixtures of ethanol-t-butanol was due to reduced recombination. The higher efficiency at the 7 μm thick films for the co-solvent mixtures was because N-719 dye sensitized efficiently up to 750 nm and thinner films provided higher electron collection efficiency.

The effect of t-butanol was probed by changing the percentage of ethanol to t-butanol from 25 % to 100 %. DSSCs prepared with 7 μm titania flms impregnated in ethanol-t-butanol (25:75 %) showed best device performance. This was likely due to minimized recombination. It is understood that t-butanol reacts with titania surface and reduces recombination between electrons and the electrolyte. The effect of multilayer dye formation on titania was probed by changing the concentration of N-719 in ethanol-t-butanol (25:75 %) from 1.0×10^{-4} to 4.0×10^{-4} M. Efficiency was enhanced by increasing

concentration of dye and was found optimum at 3.0×10^{-4} M. However, it dropped at 4.0×10^{-4} M and this was likely due to multilayer formation of dye molecules on titania surface, see Figure 5-9. The lower efficiency of the 50:50 vol % compared with the previous result in Figure 5-8b was related to FTO reduced transmission. The properties of the best dye sensitized solar cells fabricated in different solvent mixtures are summarized in Table 5-1. DSSCs made with the 7 μm films impregnated with N-719 showed best efficiency of 9.44 % and 4.84 %. DSSCs made with thick films of 20 and 10 μm impregnated with N-749 showed best efficiency of 6.57 % and 5.82 %.

Concluding Remarks

DSSCs made with thick photoanodes using N-749 showed high efficiency due to improvement of absorption of light between 700 to 900 nm. Although using tert-butanol helped enhance efficiency of the 10 μm films by reducing recombination, it was only sc- CO_2 mixture that allowed enhancing the photoactive surface area and higher efficiency for the 20 μm thick films. DSSCs made with 7 μm thick photoanodes using N-719 dye showed higher efficiency because N-719 dye sensitizes efficiently up to 750 nm and it is likely that the thinner films allow higher electron collection efficiency. This shows importance of dye sensitization for enhancing performance of DSSCs.

Table 5-1. The efficiency of the best DSSCs made with FTO substrates with titania films of various thicknesses with N-719 and N-749 dissolved in various solvent mixtures.

Dye	Solvents	Thickness (μm)	Isc (mA/cm ²)	Voc (V)	FF	Efficiency (%)	τ (s)
N-719	Ethanol:t-But	7	22.43	0.77	0.55	9.44	0.018
N-749	CO ₂ :AcN:t-But	20	16.92	0.73	0.53	6.57	0.029
N-749	AcN:t-But	10	13.27	0.77	0.57	5.82	0.509
N-719	CO ₂ :Ethanol	7	10.16	0.74	0.64	4.84	0.076

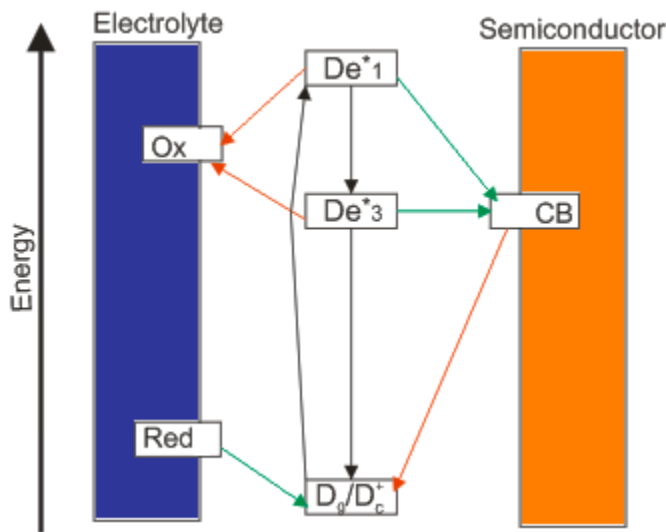


Figure 5-1. Electron transport and recombination paths between the semiconductor and the electrolyte. After light has excited dye molecules to states of different energy (black), electrons are injected into the conduction band of the semiconductor and complete the circuit to reduce oxidized electrolyte (green). Electrons can recombine with the oxidized species of the electrolyte or with unexcited dye molecules (red).

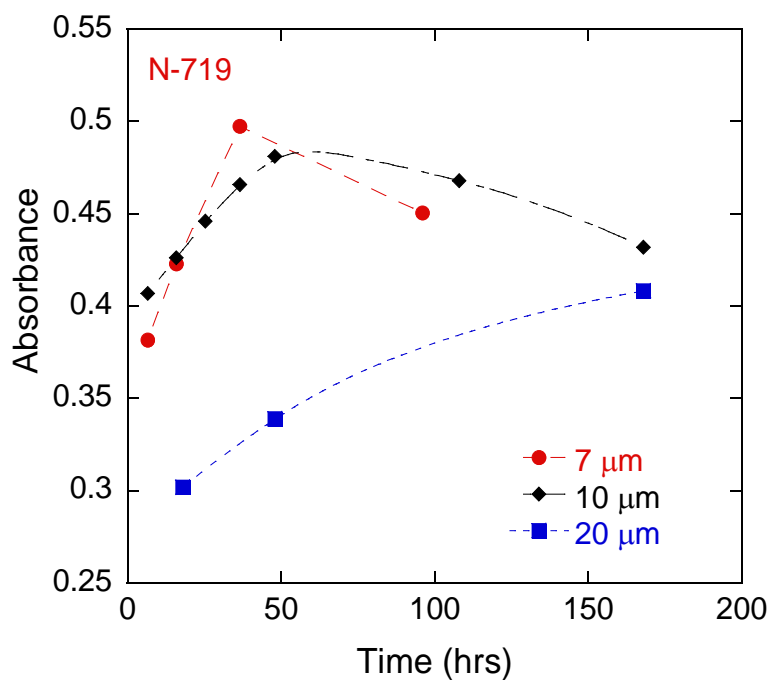
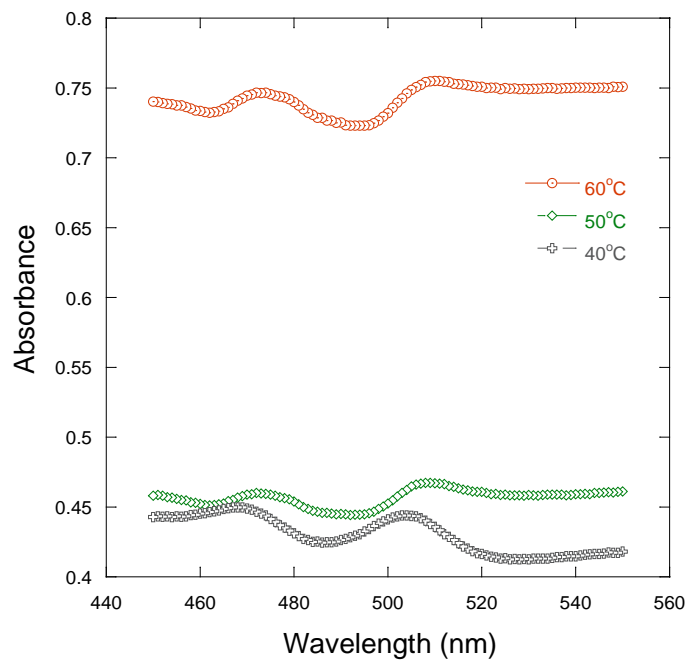


Figure 5-2. Absorbance of 7, 10 and 20 μm titania films in N-719 dye. The adsorption peaks vary depending on film thickness.

(a)



(b)

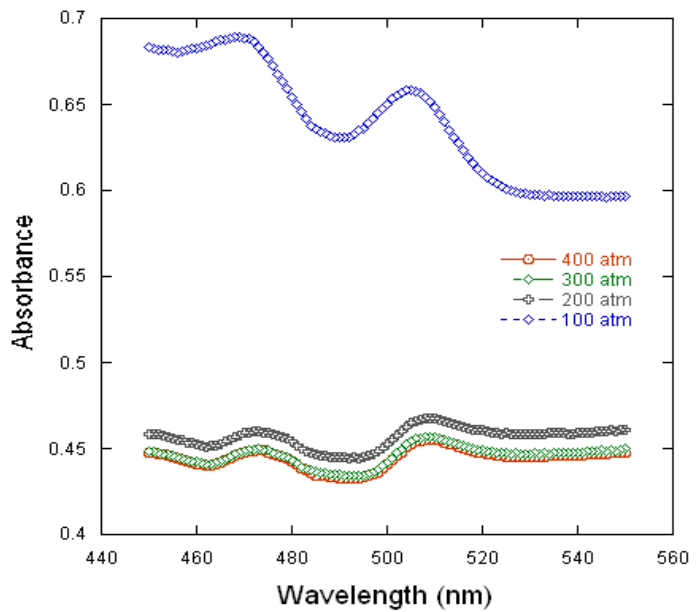


Figure 5-3. Solubility of N-719 dye in sc-CO₂ and 4-5 % of ethanol as a co-solvent using in situ UV-VIS measurements. Solubility at 200 atm and temperatures ranging from 40 to 60°C showing higher absorbance (lower solubility) at 60°C (a). Solubility at 50°C and pressures ranging from 100 to 400 atm showing higher absorbance (lower solubility) at 100 atm (b)

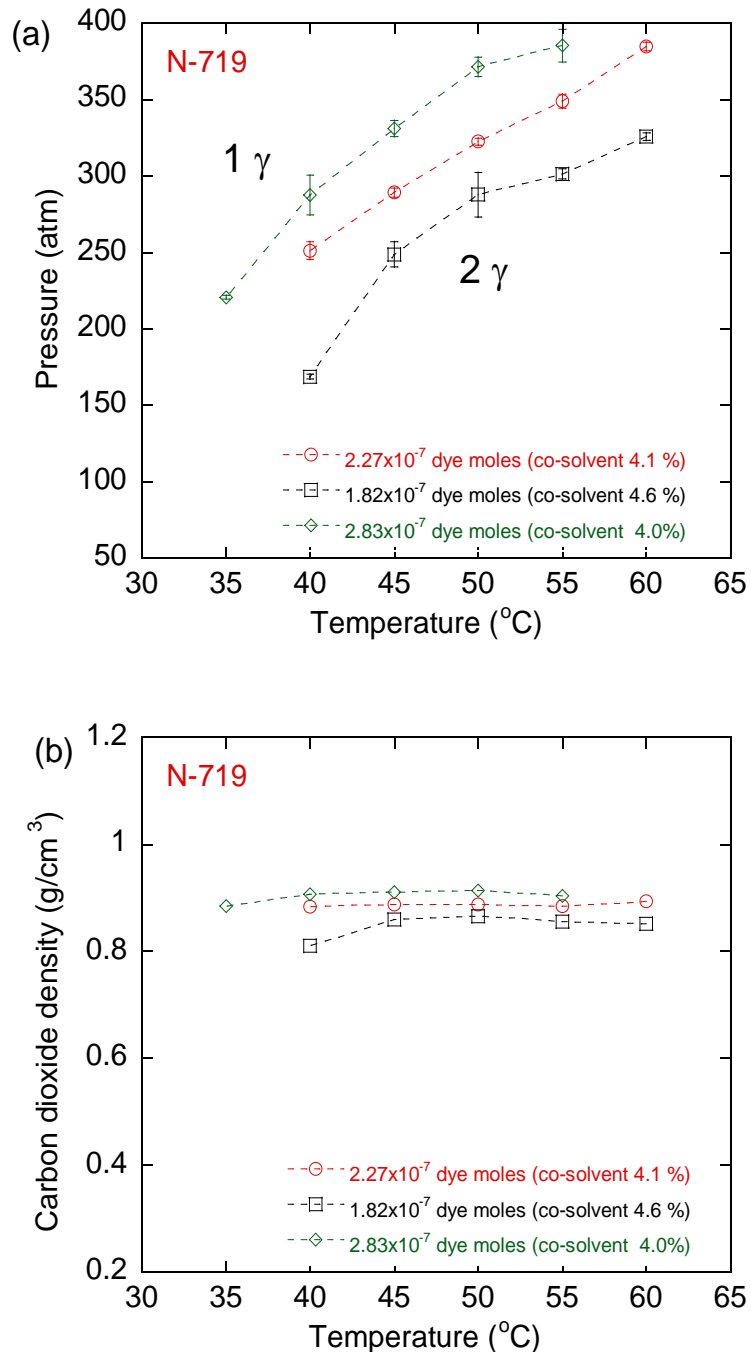


Figure 5-4. Solubility of N-719 in carbon dioxide using ethanol as a co-solvent. Cloud point measurements of N-719 in sc-CO₂ and less than 5 % of ethanol as a co-solvent (a). Solubility of N-719 is proportional to density of carbon dioxide (b).

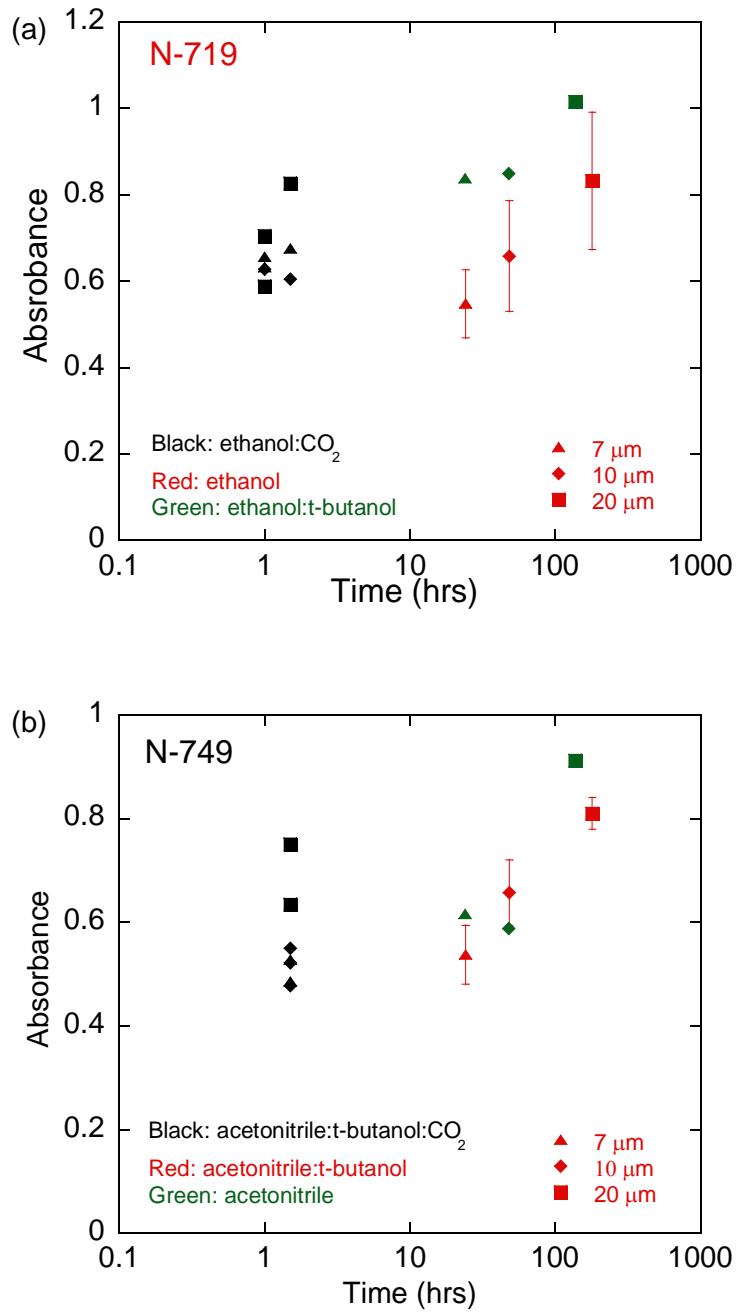


Figure 5-5. Absorbance of impregnated titania films by UV-VIS spectroscopy.

Absorbance of 7,10 and 20 μm anatase titania film in N-719 dye dissolved in solvent mixtures of ethanol, t-butanol and sc-CO₂ (a). Absorbance of similar titania films in N-749 dye dissolved in solvent mixtures of acetonitrile, t-butanol and sc-CO₂ (b)

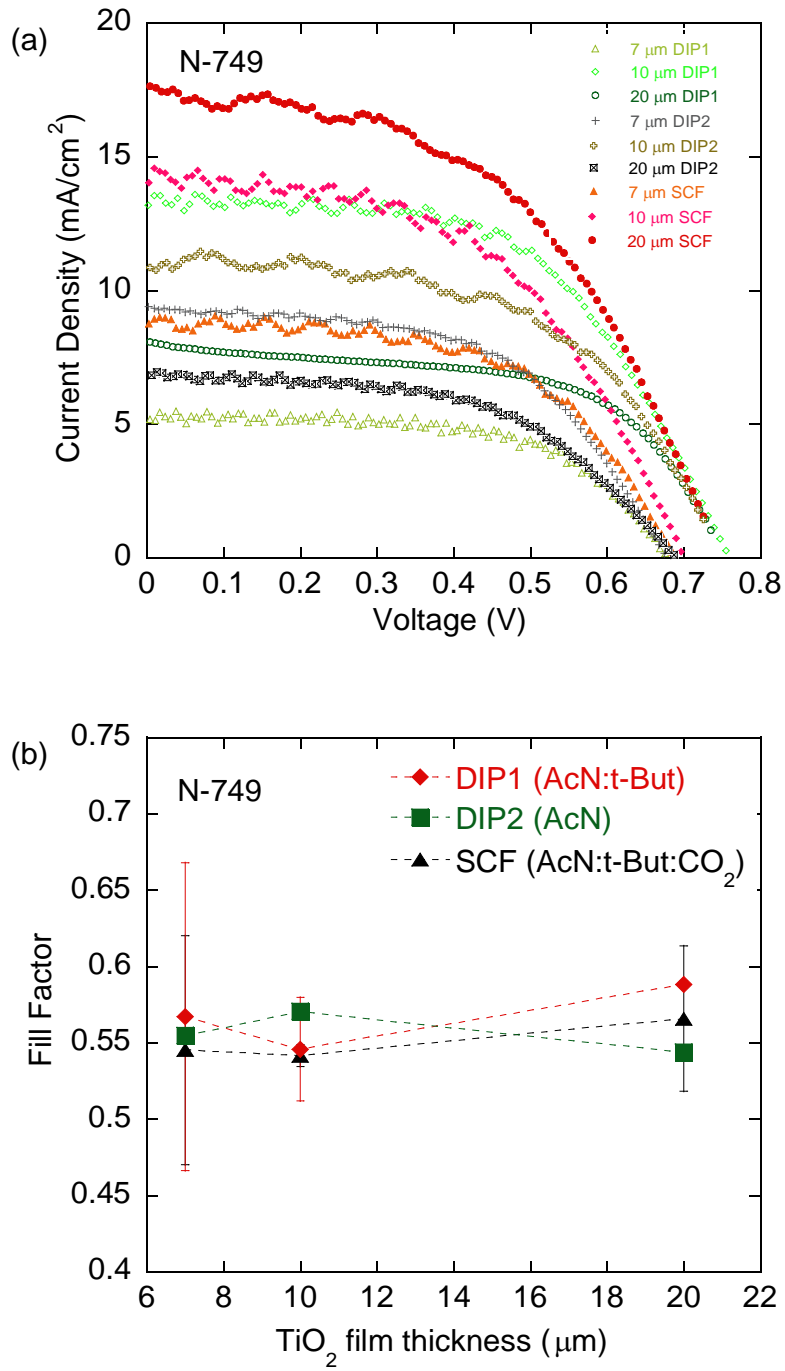


Figure 5-6. Performance characteristics of DSSCs fabricated from photoanodes in N-749. IV curves of DSSCs prepared with 7, 10 and 20 μm thick titania films impregnated with N-749 dye in acetonitrile, t-butanol and sc-CO₂ (a). Fill factors of the DSSCs at various film thicknesses (b).

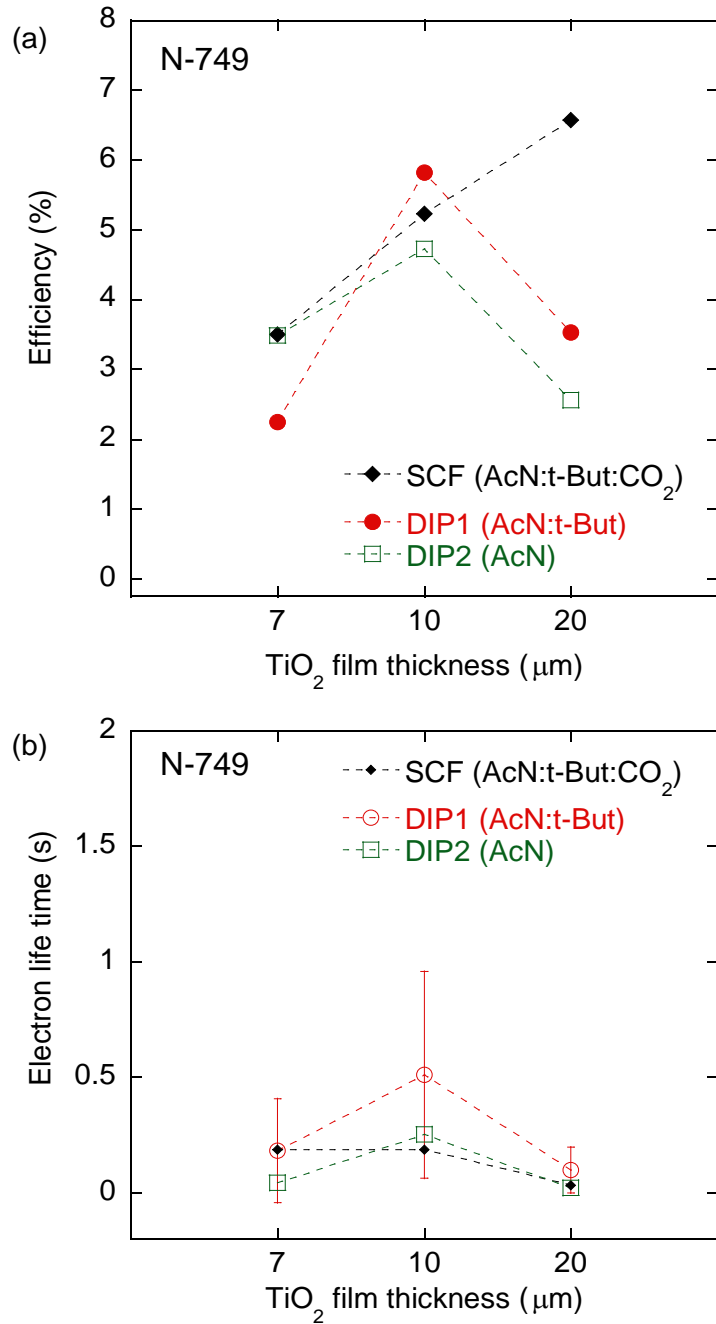


Figure 5-7. Efficiency and electron life time of DSSCs fabricated from photoanodes in N-749. Efficiency (a) and electron life time (b) of DSSCs made with titania films of various film thicknesses impregnated with N-749 in acetonitrile, t-butanol and sc-CO₂.

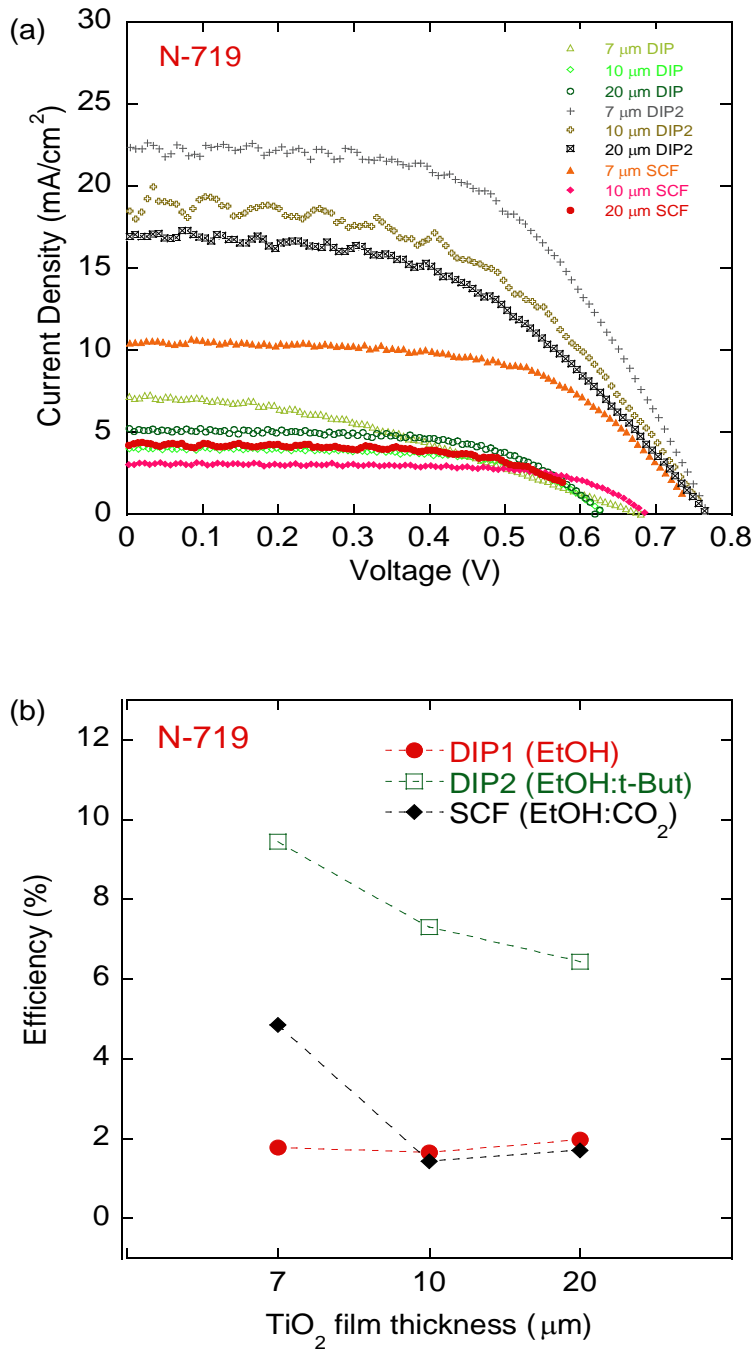


Figure 5-8. Performance characteristics of DSSCs fabricated from photoanodes in N-719. IV curves of DSSCs prepared with 7, 10 and 20 µm thick titania films impregnated with N-719 dye in ethanol, t-butanol and sc-CO₂. Efficiency of the DSSCs at various film thicknesses (b).

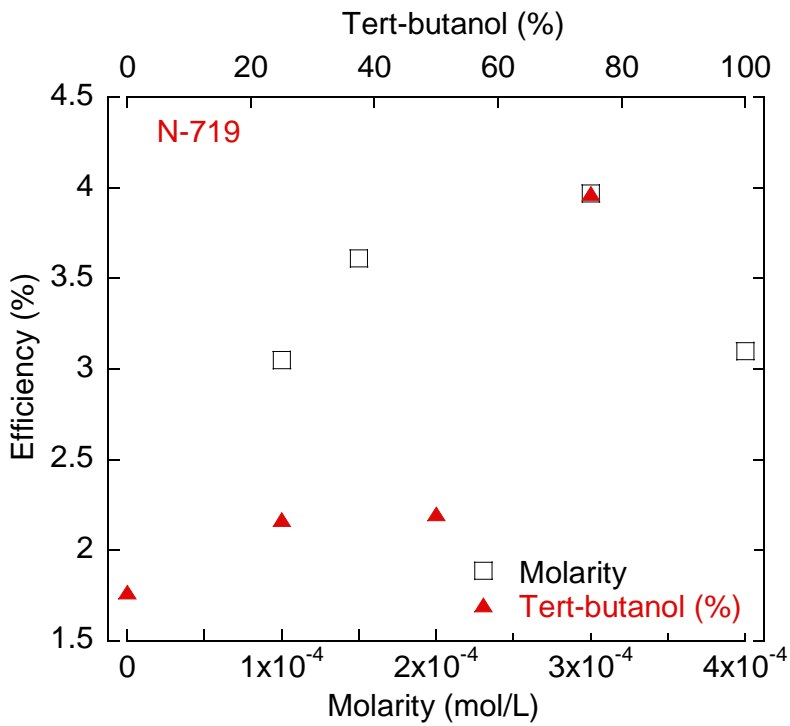


Figure 5-9. The effect of t-butanol and concentration of N-719 on the efficiency of DSSCs. The DSSCs are made with 7 μm titania films sintered at 2.3 kPa and at 450°C. The optimum concentration is 3.0×10^{-4} M in ethanol and t-butanol at (25:75 vol %).

CHAPTER 6 CONCLUSION

The work in this dissertation explores a unique approach to transport in nanomaterials utilizing supercritical carbon dioxide as an alternative co-solvent. The improved transport in carbon nanotubes allowed their benign purification without altering their unique properties. The extraction efficiency of carbon nanotubes made with different processes was related to the nonotube properties and accessibility of metal catalyst for oxidation.

Thick titania films on FTO and ITO substrates were prepared to increase the semiconductor surface area. The effect of sintering pressures and cooling rates were probed to avoid film defects. Sintering the titania films at low pressures reduced the stresses on both ITO and FTO substrates. The effect was more prominent in titania films prepared on FTO, resulting in significantly lower defects in the films. The preparation of defect-free titania films on ITO required further control of the heating and cooling steps. DSSCs fabricated under vacuum yield better device characteristics than the standard method for making photoanodes. DSSCs fabricated with these FTO films showed best performance at intermediate vacuum levels. These results indicate that the lowest pressures used to make the photoanode are good for minimizing defect density but not optimizing device performance.

The nondestructive method for analysis of dye adsorption was developed for device analysis with respect to dye coverage. The molar extinction coefficients of both N-719 and N-749 dyes adsorbed onto titania were determined. These molar extinction coefficients can be used to determine the concentration of dye adsorbed in films of varying thicknesses without destroying the film.

The photoactive surface area of DSSCs thick semiconductor films was increased by performing wet and gas impregnation at optimal adsorption times for both N-719 and N-749. Utilizing supercritical carbon dioxide for impregnation of thick films overcame transport limitation by wet methods. Device characteristics such as efficiency and electron lifetime were analyzed with respect to film surface area, porosity, and dye coverage. While DSSCs made with thicker photoanodes worked better with N-749, those made with thinner photoanodes worked better with N-719 due to sensitization properties of the different dyes.

APPENDIX A
SUPERCritical FLUID PURIFICATION OF (PRE-PURIFIED) SINGLE WALL
CARBON NANOTUBES (SWCNTS)

Introduction

Supercritical carbon dioxide is shown to be a good solvent environment for removing metal impurities from carbon nanotube samples. The best processing conditions tested were at the moderate conditions of 45°C and 400 atm using hexafluoroacetylacetone as a chelating agent, yielding a final ash (metal oxide) content of 2.4 wt % or an estimated metal content of 1.5 wt % or less. Not only did these conditions efficiently remove the metal from the carbon nanotubes, the process had no effect on the inherent properties of the carbon nanotubes. Both Raman and fluorescence spectroscopy are sensitive to impurities and showed no increase in sidewall damage or reduction in emission intensity. Triton X-100 was demonstrated as an alternative chelating agent.

Experimental Procedure

Materials and Reagents. Tri-n-butylphosphate (TBP – 99 % purity from Sigma-Aldrich), Triton X-100, and hexafluoroacetylacetone (HFA – 95 % purity from Sigma-Aldrich) were used as received. Carbon nanotubes were used as received. Carbon dioxide was received from Praxair and used as received.

Procedure. The stainless steel extraction cell (9/16" I.D. × 9" in length, 24 mL) was immersed in a water bath and temperature controlled using a recirculating bath. Pressure was controlled to ± 2 bar using a 260 mL Isco syringe pump (Lincoln, NE). An external magnetic stirrer drove a PTFE-coated magnetic stir bar. Approximately 20 mg of carbon nanotubes were wrapped in Whatman filter paper and inserted into the reaction cell. The chelating agent and oxidizing agent were loaded into a boat and

inserted into the chamber. The chelating agent and oxidizing agent were added at a 1:1 ratio for Triton X-100 and 1:2 ratio for HFA. The cell was loaded with CO₂ to approximately 100 atm and then heated to the desired temperature. Once equilibrium was achieved, CO₂ was again loaded until the desired pressure was reached. The chamber was held at the extraction conditions for 1 h. The CO₂ was then slowly vented and bubbled through water, yielding a turbid, purple solution. The nanotubes were recovered from the chamber and bath sonicated in ethanol for 30 min. The suspension was then filtered through a 0.1 µm PTFE membrane and washed with hexane.

Characterization. Thermogravimetric (TGA) analysis was conducted in air up to 800°C at a ramp rate of 10 °C/min. Raman spectra were recorded on the solid carbon nanotubes using a Reinshaw Invia Bio Raman with excitation from a 785 nm diode laser. For fluorescence measurements, carbon nanotubes were dispersed in 1 wt % SDBS surfactant using a probe tip ultrasonicator and characterized using an Applied NanoFluorescence Nanospectrolyzer (Houston, TX) with excitation from 662 and 784 nm diode lasers.

Results

Effect of Pressure and Temperature on Extraction. The ash (metal oxide) content of the asreceived carbon nanotubes before purification was 9.3 %. Carbon nanotubes collected from the extraction chamber were analyzed using TGA to measure the remaining metal content in the sample. All purification conditions showed reduced metal content in the carbon nanotubes. Figure A-1 shows the effect of temperature and pressure on the final ash content of carbon nanotubes purified using HFA as the chelating agent. As can be seen in the figure, higher pressures and temperatures yield

better metal removal. The lowest ash (metal oxide) content achieved to date is 2.4 wt %. Without knowing the exact atomic content of the catalyst, it is difficult to convert this to the true metal content. However, it is estimated that this corresponds to a metal content of 1.5 wt % or less.

Multiple extraction steps. The carbon nanotubes were first purified at 45°C and 400 atm. The extraction was then repeated with fresh chelating agent and oxidant at the same operating conditions. The final metal content after the second extraction did not improve (results not shown). The lack of any changes suggests that a single-step extraction is feasible provided the ratios of all components are optimized.

Assessment of carbon nanotube damage. The most critical parameter to characterize in the purification of carbon nanotubes is the damage to the sidewall and the amount of residual compounds remaining that affect their properties. Most purification processes use strong acids or oxidative environments to remove the impurities, which can oxidize the carbon nanotube sidewalls. Raman spectroscopy provides a measure of the sp₃/sp₂ carbon atoms (~1300 and ~1600 cm⁻¹, respectively) in the carbon nanotube sidewall. This ratio of bands, also known as the D/G band ratio, is often used to describe the quality of the carbon nanotubes. The Raman spectra for the raw nanotubes in Figure A-2 show a low D/G ratio indicative of high quality carbon nanotubes with few sp₃ defects. After purification using HFA in sc-CO₂, there are no changes to the Raman spectra. These results indicate that there has been no sidewall damage introduced to the nanotubes during the purification process. While Raman spectroscopy is an accurate means of indicating changes to the structure of the nanotubes, some carbon nanotube properties, such as fluorescence, are very sensitive

to the presence of even small amounts of impurities. Most purification processes result in substantial reductions in the fluorescence emission of carbon nanotubes. These reductions are possibly due to the remaining acid, which tends to quench the fluorescence. In many purification processes, the reduction in emission intensity can be an order of magnitude or more. Figure A-3 shows the fluorescence spectra for the raw and the highest purity carbon nanotubes obtained using HFA as a chelating agent. As can be seen, both have good fluorescence spectra with peaks corresponding to different types of carbon nanotubes. The purified nanotubes show similar fluorescence intensity to the raw sample.

Triton X-100 as a chelating agent. Triton X-100 was tested as a cheaper alternative to HFA for the chelating agent in the removal of metal impurities in sc-CO₂. TX-100 was capable of removing the metal from the as-received carbon nanotubes. While this chelating agent did not perform as well as HFA, it did remove a considerable amount of the metal impurities. The differences in extraction efficiency are likely related to the reduced solubility of the surfactant in sc-CO₂. It is anticipated that better metal removal could be obtained with multiple extraction steps or optimized extraction conditions.

Conclusions

Carbon nanotubes were purified in supercritical CO₂ using an oxidant and chelating agent. The carbon nanotubes were characterized to determine the amount of metal remaining and the effect of purification on the final properties of the nanotubes. The metal content was reduced at all extraction conditions using a single-step extraction. However, it was found that higher pressures and temperatures yielded the

lowest metal content. The best extractions were obtained when using HFA as the chelating agent at 45°C and 400 atm. The final ash content was 2.4 wt % or an estimated metal content of 1.5 wt % or less. The purified carbon nanotubes showed no changes to their inherent properties during processing. Raman spectra, especially the D band which measures the amount of sidewall defects, showed no changes. The fluorescence of the carbon nanotubes also showed no decrease in intensity after purification. Therefore, the purification of carbon nanotubes using chelating agents and oxidants in a supercritical environment provides a benign process capable of achieving nanotubes with low metal content.

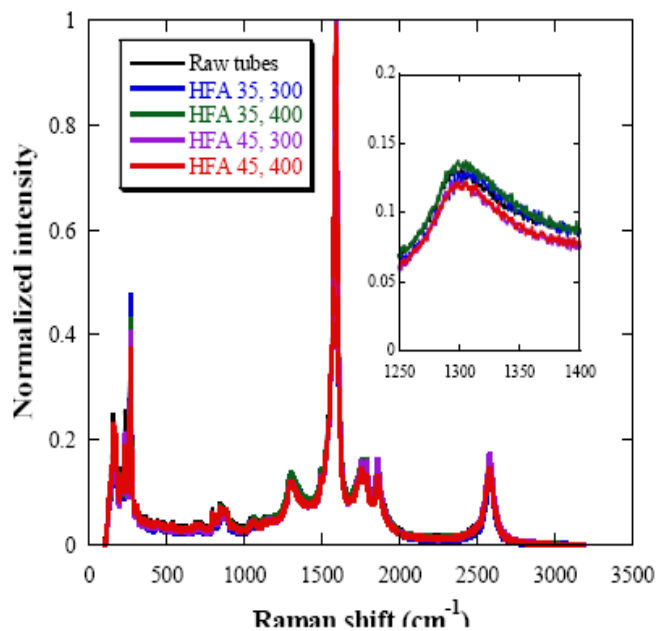


Figure A-1. Raman spectra of raw and treated carbon nanotubes. Supercritical carbon dioxide treated sample at 35 to 45°C and 300 to 400 atm show comparable spectra to the raw sample indicating no side wall damage to the carbon nanotubes.

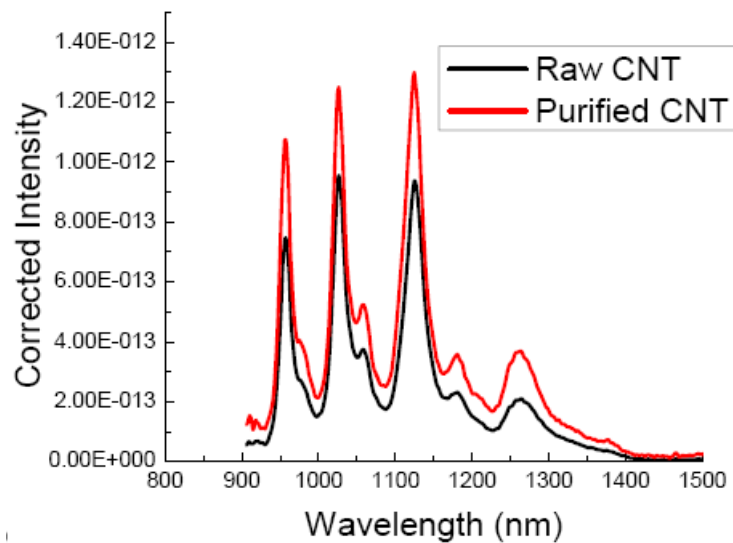


Figure A-2. Fluorescence of raw and treated carbon nanotubes. Supercritical carbon dioxide extraction shows comparable intensity.

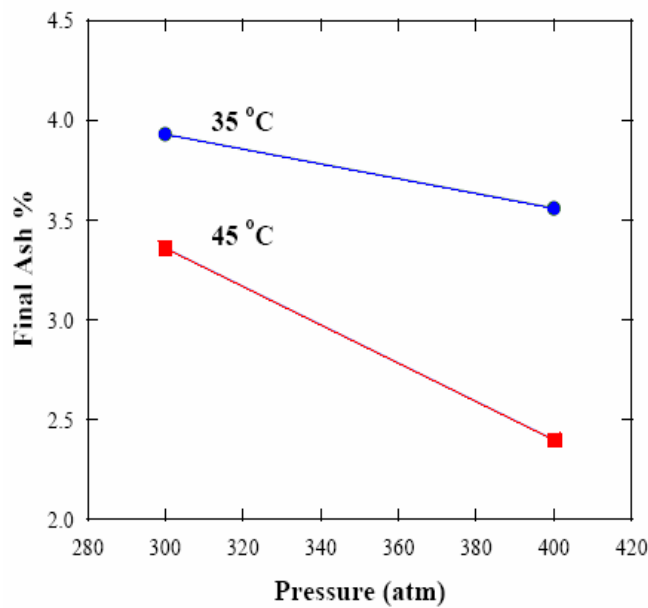


Figure A-3. Final metal oxide content of treated carbon nanotubes. Supercritical carbon dioxide extraction was performed at temperature from 35 to 45°C and pressures from 300 to 400 atm. A single extraction at 45°C and 400 atm shows 2.4 wt % of final ash content.

APPENDIX B
ELECTRO-DEPOSITION AND TEMPLATE REMOVAL USING SUPERCRITICAL
CARBON DIOXIDE

Nanowire Electrodeposition Using Supercritical Carbon Dioxide

The main factor for efficiency in DSSCs is the high photo active surface area of the semiconductor. Semiconductor nanoparticle films have high surface area but electron diffusion is low. In nanowire dye sensitized solar cells, electron diffusion is increased by replacing the nanoparticle film with an array of oriented single-crystalline nanowires. Electron transport in crystalline wires was found to be several orders of magnitude faster than percolation through a random polycrystalline network due to excellent crystallinity and radial electric field in each nanowire which helps in repelling electrons from the surrounding electrolyte [1,6]. Nanowires enable faster electron transport but lack the high surface area. Therefore, synthesis of high density nanowires is essential for achieving both faster electron transfer and high surface area. Template synthesis by electrodeposition has been the best method for synthesis of highly ordered nanomaterials. However, this technique can lead to incomplete pore inclusion and pin holes formation due to hydrogen hydrolysis. Moreover, it can produce polycrystalline materials with larger grain sizes.

CO₂ in water miniemulsions. Miniemulsions are defined as aggregates of one phase dispersed in another phase with sizes between microemulsions and emulsions. Sc-CO₂-in-water miniemulsions can be used in electrodeposition for synthesizing arrays of high aspect ratio nanowires with better inclusion and conductivity. Psathas et al. showed that sc-CO₂-in-water miniemulsions of 175 nm droplets can be formed with the phase inversion temperature (PIT) emulsification method with low shear followed by

rapid cooling. The temperature-induced inversion in the curvature of the system occur with a minimum in interfacial tension [68]. Pore inclusion has been problematic in nanomaterials synthesis by techniques such as chemical vapor deposition (CVD) or electrodeposition. This can be due to release of hydrogen during hydrolysis that can block or plug pores entrances in electrodeposition. Miscibility of hydrogen in SCF can prevent hydrogen hydrolysis and allow complete inclusion. Yoshida et al. showed that pin holes formation in the order of microns can be eliminated in nickel electroplating using sc-CO₂ [69,70].

Electrodeposition using sc-CO₂. Electrodeposition in SCF miniemulsions is similar to pulse electrodeposition; nucleation and crystal growth cannot occur when SCF comes in contact with the cathode, therefore grain size is limited and better crystalline materials are formed. Tian et al. have prepared Ag, Au and Cu single crystal nanowires by template electrodeposition utilizing a slow multi step nucleation and growth mechanism by lower over-potential and higher temperature and a gelatin additive to enhance the growth of single crystal metal nanowires [71,72]. These conditions can enhance surface diffusion of atoms and favors the growth of existing crystal nuclei.

Anodized alumina oxide templates. The best method for synthesis of highly ordered nanowire arrays has been utilizing the ordered templates of anodized alumina oxide (AAO), which are available commercially in 50 to 200 nm in diameter and up to 60 microns in length. Alumina oxide is anodized in phosphoric acid to enlarge pore size and then etched in phosphoric, oxalic or sulfuric acids [72,73] at different temperatures to form cylindrical channels of varying diameters. Electrodeposition is confined to the walls of the AAO template.

Equipment Built. To perform electrodepositioin using a SCF, a high temperature and pressure system was designed, high pressure chamber (HPC) insulated safety box was built and initial experiments were performed. Isco pump is used to deliver pressurized carbon dioxide from a CO₂ tank to the HPC. A homogenizer pump should be used to homogenize sc-CO₂ and the electrolyte solution and circulate the fluids to the high pressure chamber through the volume variable view cell as seen in Figure B-1a. Volume variable view cell with side sapphire windows can be used with UV-vis spectroscopy for phase verification.

For safety, a double-wall aluminum box was constructed for the 1L high pressure chamber (Autoclave engineering). High temperature insulation blanket was installed between the double walls of the chamber box. The set up of our chamber includes temperature controller and solid state relays connected by high temperature wiring to six heating bands (Tempco) on the chamber, a thermocouple inserted in the cap of the chamber for temperature control and a potentiostat, which can be used to ensure a constant applied voltage for a three electrode cell configuration, see Figure B-1b. Two 12" electrodes and two sample holders were coated with a micron of platinum against corrosion, see Figure B-1c. Electrodes length enables minimum separation distance between the electrodes during electrodeposition. A thin platinum wire in 1/16" tubing can be used as a reference electrode. Temperature controller PID values were manually tuned for our system. Inert beads are to be used as volume fillers inside the high pressure chamber to minimize working volume by 50 %.

Experimental. Sc-CO₂-in-water environment are utilized by formation of emulsions or miniemulsions [70,74-78] using ionic or non-ionic surfactants. The steric

forces between the head groups of molecules of an ionic surfactant are stronger than those in a non-ionic surfactant. Therefore, they should form stronger and more stable emulsions. AOT and decane as a co-solvent (99.0 % purity- Fisher Scientific Co.) and Octaethylene Glycol Monododecyl Ether-OGME (99.7 % purity- Wako Pure Chemicals Co.) have been used to make emulsions as ionic and non-ionic surfactants, respectively [79-81]. Sc-CO₂-in-water miniemulsions of 175 nm can be formed by using a triblock copolymer of poly-(dimethylsiloxane) (PDMS) and poly (ethylene oxide) (PEO), PEO-PDMS-PEO [68].

Emulsion formation by an ionic surfactant. Emulsions of sc-CO₂-in-water were formed in a volume variable view cell (volume 23 ml). 1.0 g of AOT, an ionic surfactant, was dissolved in 15 ml of double di-water by stirring at 70°C. Then, 0.2 ml of decane was added as a co-solvent to the volume variable view cell, which was set in the water bath at 45°C. After system reached equilibrium, 8 ml of supercritical CO₂ at 75 atm was injected. After agitation by stirring using cross shaped stir bar, emulsions started to form. Complete emulsions of sc-CO₂-in-water were formed in 10 min.

Electrodeposition of metal nanowires. Nickel was chosen for initial studies of electrodeposition [69,77,79,82,83]. Nickel electrolyte watt bath was prepared by using nickel chloride, nickel sulphate and boric acid. Nickel electrodeposition was performed on 0.1 micron AAO Whatman template at atmospheric pressure and room temperature [69,82], see Figure B-2. Brass and nickel metal electrodes were used as a cathode and an anode, respectively. The current density used was 2.0 mA/dm². Deposition time was 40 min based on template thickness of 13 microns. After experiment was completed, nickel was plated on brass metal and templates were taken for analysis. AAO template

was dissolved in 25 % phosphoric acid for 24 h. TEM confirms deposition of nickel, see Figure B-3. However, deposits are less than 0.1 micron, less than pore diameter, which is attributed to etching of the deposits in the phosphoric acid.

Template Removal Using Supercritical Carbon Dioxide

Capillary evaporation and surface forces can cause aggregation of nanowires when a template is dissolved and dried in air. Zheng et al. observed small cracks in ZnO nanowires arrays and suggested that the cause is the mechanical forces during the processes of dissolution and drying [84]. Pressure drop across the interface is related to surface curvature and wetting angle according to Young's equation:

$$\Delta P = \frac{2\gamma \cos \theta}{a} \quad (\text{B-1})$$

where P is pressure, γ is surface tension of the interface, a is radius, and θ is the contact angle. As the wetting angle decreases during evaporation, the pressure drop rises and the surface forces cause the nanowires to be pulled closer and aggregate. This hinders their use in DSSCs applications where a uniform structure is required for optimum photon collection and electron transport.

Conclusions and Future Avenues of Research

Electrodeposition can be controlled better without ionic species transfer by stirring. However, aggregation formation requires agitation. Therefore, miniemulsions stability in the view cell using PEO-PDMS-PEO surfactant is required to ensure that experiments can be carried out in stable miniemulsions [68,78,85,86] prior to electrodeposition of nanomaterials. Homogenizer pump should be run initially for homogenization of the fluids. Then it can be stopped during electrodeposition. Miniemulsion stability study can be performed using the phase inversion method (PIT) [87] with 50:50 C/W (CO₂-in-

water) at initial temperatures between 40 and 90°C, cooling times between 5 and 10 min and pressures between 300 to 150 atmospheres. Metal and semiconductor nanowires such as ZnO [88] and Ni of 200 nm in diameter and 30 to 60 microns in length can be synthesized using AAO templates to study the effect of hydrogen hydrolysis and miniemulsions on pore inclusion, pin hole formation and crystallinity. Pore inclusion and conductivity of individual nanowires can be tested using conductive AFM.

The widely used wide band gap semiconductors for electron transport in DSSCs, titania (TiO_2) and zinc oxide (ZnO), should ideally be single crystalline to enhance electron transfer and reduce entrapment events and percolation in the semiconductor. However, they can hardly be synthesized as single crystalline due to their high melting points. Single crystalline materials require high temperature or low time for atoms to preferentially probe most favorable sites, which cannot be achieved by electrodeposition in an aqueous environment. Alternatively, a single or polycrystalline metal coated with a small layer of semiconductor can be used for faster electron diffusion. Dobrev et al. synthesized single crystal nanowires such as Cu, Pb, Bi, Ag and Sb by pulsed electrodeposition [72]. Polycrystalline metals such as Co, Ni, Rh and Pt can be synthesized. Deposition of titania on metal nanowires by electrophoretic deposition can be utilized for DSSC's fabrication [45,89-91].

Capillary evaporation and surface forces effects on aggregation can be studied using SCF drying with nanowire arrays of 50 to 100 nm in diameter and 10 to 30 microns in length. Nanowire arrays of can be placed in a micro chamber immersed in a water bath set to a desired temperature by a thermoregulator. Carbon dioxide can be supplied to a micro reactor to the desired pressure by isco pump. Drying using sc- CO_2

can be performed in a static process at temperatures between 35 and 55°C and pressures between 100 and 200 atm. Then sc-CO₂ can be vented slowly out of the system. Analysis can be carried out by scanning electron microscopy.

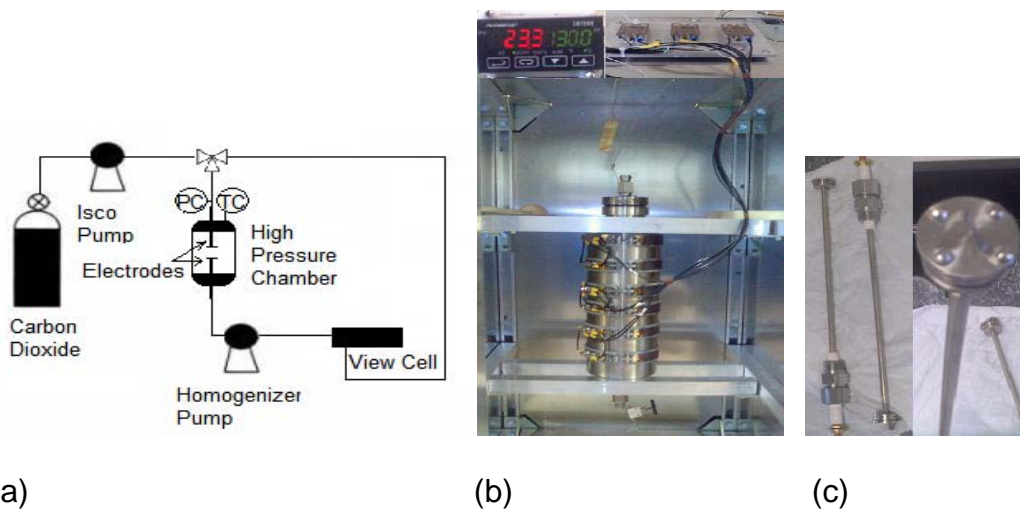


Figure B-1. High pressure system for electrodeposition. Setup for electrodeposition using sc-CO₂ in high pressure chamber (a). High pressure chamber and temperature control system (b). Electrodes coated for corrosion (c).

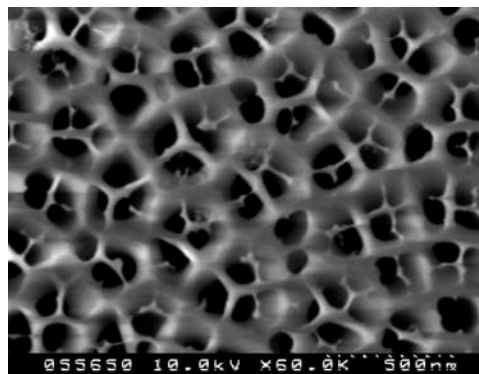


Figure B-2. SEM image of 200 nm whatman anodisc 13.

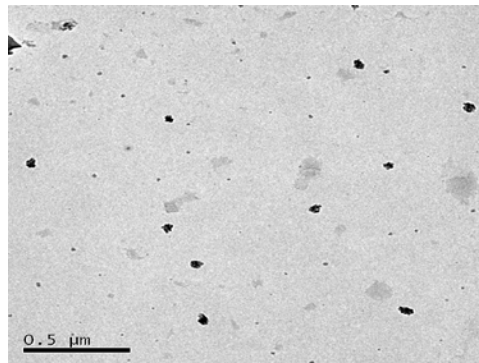


Figure B-3. TEM image of nickel deposits from a watt bath solution.

APPENDIX C

ANODIZING ALUMINUM AND NANOWIRE ELECTRO-DEPOSITION

Electrodeposition in electrolyte solution using anodized alumina templates was investigated as an alternative structure for dye sensitized solar cells. First, ITO substrates are degreased in soapy water, acetone and ethanol for 30 min each to remove contamination. Then, deposition of chromium or titanium interlayers, along with aluminum onto ITO substrates is performed using Ebeam evaporator at Microfab facility. These aluminum substrates are then anodized to make AAO on ITO for the templated deposition of nanowires.

The procedure includes deposition of 10 nm titanium or chromium layer to enhance adhesion, 2 to 10 μm thick aluminum layer and 10 μm silica layer strip on the film near the top of the substrate to prevent excessive oxidation during anodization at the air-solution interface, see Figure C-1. The materials used in this procedure are 99.99 % aluminum shots (9.5 mm), titanium, chromium and silica (glass pieces), and sample graphite crucibles, all provided by Microfab.

Reproducibility of these substrates was problematic due to variability in ITO substrates quality as well as Ebeam operations. However, the successful films were anodized in 11 wt % phosphoric acid. Some films failed either at the beginning or end of the anodization due to poor adhesion. The properly anodized films were pore widened in 5 wt % phosphoric solution for 5 min and 30 seconds. Electrodeposition of gold nanowires was performed. Most films showed uneven deposition possibly due to uneven anodization. The AAO template was then removed by etching in 25 wt % phosphoric acid. The nanowires remained in solution until they were taken for electrostatic repulsion to prevent nanowire aggregation. This method was developed in

the lab. However, non aggregated nanowires could not be synthesized with this method. This could be due to all the variability in the process. The operation of the Ebeam evaporator was changed after major maintenance and Al deposition at the 200-300 angstroms per second could not be achieved. The rate of deposition was related to good adhesion of Al on the ITO substrates.



Figure C-1. Substrates after deposition of Cr and Al layers, wrapped in Al foil for silica deposition.

LIST OF REFERENCES

- [1] M. Law, L.E. Greene, J.C. Johnson, R. Saykally, P.D. Yang, Nanowire dye-sensitized solar cells, *Nat. Mater.* 4 (2005) 455-459.
- [2] P.V. Kamat, Meeting the clean energy demand: Nanostructure architectures for solar energy conversion, *J. Phys. Chem. C.* 111 (2007) 2834-2860.
- [3] A.C. Fisher, L.M. Peter, E.A. Ponomarev, A.B. Walker, K.G. Wijayantha, Intensity dependence of the back reaction and transport of electrons in dye-sensitized nanocrystalline TiO₂ solar cells, *J. Phys. Chem. B.* 104 (2000) 949-958.
- [4] M. Gratzel, Solar energy conversion by dye-sensitized photovoltaic cells, *Inorg. Chem.* 44 (2005) 6841-6851.
- [5] M. Adachi, M. Sakamoto, J.T. Jiu, Y. Ogata, S. Isoda, Determination of parameters of electron transport in dye-sensitized solar cells using electrochemical impedance spectroscopy, *J. Phys. Chem. B.* 110 (2006) 13872-13880.
- [6] M. Law, L.E. Greene, A. Radenovic, T. Kuykendall, J. Liphardt, P.D. Yang, ZnO-Al₂O₃ and ZnO-TiO₂ core-shell nanowire dye-sensitized solar cells, *J. Phys. Chem. B.* 110 (2006) 22652-22663.
- [7] J. Halme, G. Boschloo, A. Hagfeldt, P. Lund, Spectral characteristics of light harvesting, electron injection, and steady-state charge collection in pressed TiO₂ dye solar cells, *Journal of Physical Chemistry C.* 112 (2008) 5623-5637.
- [8] K. Hara, Y. Dan-Oh, C. Kasada, Y. Ohga, A. Shinpo, S. Suga, K. Sayama, H. Arakawa, Effect of additives on the photovoltaic performance of coumarin-dye-sensitized nanocrystalline TiO₂ solar cells, *Langmuir.* 20 (2004) 4205-4210.
- [9] E. Reverchon, R. Adami, Nanomaterials and supercritical fluids, *J. Supercrit. Fluids.* 37 (2006) 1-22.
- [10] X.G. Ye, C.M. Wai, Making nanomaterials in supercritical fluids: A review, *J. Chem. Educ.* 80 (2003) 198-204.
- [11] B. Xu, K. Nagashima, J.M. DeSimone, C.S. Johnson, Diffusion of water in liquid and supercritical carbon dioxide: An NMR study, *J. Phys. Chem. A.* 107 (2003) 1-3.
- [12] B. Chehroudi, Supercritical fluids: Nanotechnology and select emerging applications, *Combustion Science and Technology.* 178 (2006) 555-621.

- [13] H. Kanda, M. Miyahara, K. Higashitani, Condensation model for cylindrical nanopores applied to realistic porous glass generated by molecular simulation, *Langmuir*. 16 (2000) 6064-6066.
- [14] H. Kanda, M. Miyahara, T. Yoshioka, M. Okazaki, Verification of the condensation model for cylindrical nanopores. Analysis of the nitrogen isotherm for FSM-16, *Langmuir*. 16 (2000) 6622-6627.
- [15] M. Miyahara, H. Kanda, T. Yoshioka, M. Okazaki, Modeling capillary condensation in cylindrical nanopores: A molecular dynamics study, *Langmuir*. 16 (2000) 4293-4299.
- [16] T. Uchida, T. Ebinuma, S. Takeya, J. Nagao, H. Narita, Effects of pore sizes on dissociation temperatures and pressures of methane, carbon dioxide, and propane hydrates in porous media, *J. Phys. Chem. B*. 106 (2002) 820-826.
- [17] A.J. Bard, L.R. Faulkner, *Electrochemical Methods : Fundamentals and Applications*, 2nd ed., Wiley, New York, 2001.
- [18] M. Paunovic, M. Schlesinger, *Fundamentals of Electrochemical Deposition*, 2nd ed., Wiley-Interscience, Hoboken, N.J., 2006.
- [19] J. van de Lagemaat, T.M. Barnes, G. Rumbles, S.E. Shaheen, T.J. Coutts, C. Weeks, I. Levitsky, J. Peltola, P. Glatkowski, Organic solar cells with carbon nanotubes replacing In₂O₃:Sn as the transparent electrode *Appl. Phys. Lett.* 88 (2006) 233503.
- [20] T.V. Sreekumar, Tao Liu, S. Kumar, L.M. Ericson, R.H. Hauge, R.E. Smalley, Single-wall carbon nanotube films, *Chemistry of Materials*. 15 (2003) 175-178.
- [21] Y.Q. Xu, H. Peng, R.H. Hauge, R.E. Smalley, Controlled multistep purification of single-walled carbon nanotubes *Nano Lett.* 5 (2005) 163-168.
- [22] J.L. Blackburn, T.J. McDonald, W.K. Metzger, C. Engtrakul, G. Rumbles, M.J. Heben, Protonation effects on the branching ratio in photoexcited single-walled carbon nanotube dispersions *Nano Lett.* 8 (2008) 1047-1054.
- [23] Y.H. Wang, H.W. Shan, R.H. Hauge, A Highly Selective, One-Pot Purification Method for Single-Walled Carbon Nanotubes, *Journal of Physical Chemistry B*. 111 (2007) 1249-1252.
- [24] J. Wiltshire, L. Li, A. Khlobystov, C. Padbury, g. Briggs, R. Nicholas, Magnetic separation of Fe catalyst from single-walled carbon nanotubes in an aqueous surfactant solution, *Carbon*. 43 (2005) 1151-1155.

- [25] I.W. Chiang, B.E. Brinson, A.Y. Huang, P.A. Willis, M.J. Bronikowski, J.L. Margrave, R.E. Smalley, R.H. Hauge, Purification and Characterization of Single-Wall Carbon Nanotubes (SWNTs) Obtained from the Gas-Phase Decomposition of CO (HiPco Process), *The Journal of Physical Chemistry B.* 105 (2001) 8297-8301.
- [26] J.S. Wang, C.M. Wai, K. Shimizu, F. Cheng, J.J. Boeckl, B. Maruyama, G. Brown, Purification of single-walled carbon nanotubes using a supercritical fluid extraction method, *J. Phys. Chem. C.* 111 (2007) 13007-13012.
- [27] J.P. Hanrahan, K.J. Ziegler, J.D. Glennon, D.C. Steytler, J. Eastoe, A. Dupont, J.D. Holmes, pH switching for the selective extraction of metal ions into supercritical CO₂, *Langmuir.* 19 (2003) 3145-3150.
- [28] S.W. Joanna, M.W. Chien, J.B. John, B. Gail, M. Benji, Removal of catalytic metal impurities from SWCNTs by in situ chelation/SFE in supercritical carbon dioxide, *Air Force Research Laboratory, Materials and Manufacturing Directorate.* (2006) 694-697.
- [29] S. Ikezawa, F. Mutsuga, T. Kubota, R. Suzuki, K. Baba, S. Koh, T. Koshioka, A. Nishiwaki, K. Kida, Y. Ninomiya, K. Wakita, Basic characteristics of TiO₂ film for environmental purification deposited by electron-beam-excited plasma, *Vacuum.* 59 (2000) 514-521.
- [30] K. Sunada, Y. Kikuchi, K. Hashimoto, A. Fujishima, Bactericidal and detoxification effects of TiO₂ thin film photocatalysts, *Environ. Sci. Technol.* 32 (1998) 726-728.
- [31] H. Lindstrom, R. Wootton, A. Iles, High surface area titania photocatalytic microfluidic reactors, *AICHE J.* 53 (2007) 695-702.
- [32] X. Marguerettaz, D. Fitzmaurice, Heterosupramolecular Chemistry - Long-Lived Charge Trapping by Vectorial Electron Flow in a Heterotriad, *J. Am. Chem. Soc.* 116 (1994) 5017-5018.
- [33] M.C. Carotta, M. Ferroni, V. Guidi, G. Martinelli, Preparation and characterization of nanostructured titania thick films, *Adv Mater.* 11 (1999) 943-946.
- [34] A.G. Kontos, A.I. Kontos, D.S. Tsoukleris, V. Likodimos, J. Kunze, P. Schmuki, P. Falaras, Photo-induced effects on self-organized TiO₂ nanotube arrays: the influence of surface morphology *Nanotechnology.* 20 (2009) 045603.
- [35] O. Carp, C.L. Huisman, A. Reller, Photoinduced reactivity of titanium dioxide, *Progress in Solid State Chemistry.* 32 (2004) 33-177.

- [36] N. Shibata, Plasma-Chemical Vapor-Deposited Silicon Oxide/Silicon Oxynitride Double-Layer Antireflective Coating for Solar-Cells, *Jpn J Appl Phys* 1. 30 (1991) 997-1001.
- [37] B.S. Jeong, J.D. Budai, D.P. Norton, Epitaxial stabilization of single crystal anatase films via reactive sputter deposition, *Thin Solid Films.* 422 (2002) 166-169.
- [38] M. Schuisky, K. Kukli, J. Aarik, J. Lu, A. Harsta, Epitaxial growth of TiO₂ films in a hydroxyl-free atomic layer deposition process, *J. Cryst. Growth.* 235 (2002) 293-299.
- [39] S. Ito, T. Kitamura, Y. Wada, S. Yanagida, Facile fabrication of mesoporous TiO₂ electrodes for dye solar cells: chemical modification and repetitive coating, *Solar Energy Mater. Solar Cells.* 76 (2003) 3-13.
- [40] A. Mills, N. Elliott, G. Hill, D. Fallis, J.R. Durrant, R.L. Willis, Preparation and characterisation of novel thick sol-gel titania film photocatalysts, *Photochemical & Photobiological Sciences.* 2 (2003) 591-596.
- [41] I.A. Alhomoudi, G. Newaz, Residual stresses and Raman shift relation in anatase TiO₂ thin film, *Thin Solid Films.* 517 (2009) 4372-4378.
- [42] F.Z. Zhao, B. Wang, X.F. Cui, N. Pan, H.Q. Wang, J.G. Hou, Buckle delamination of textured TiO₂ thin films on mica, *Thin Solid Films.* 489 (2005) 221-228.
- [43] F. Vaz, L. Rebouta, P. Goudeau, J.P. Riviere, E. Schaffer, G. Kleer, M. Bodmann, Residual stress states in sputtered Ti_{1-x}Si_xN_y films, *Thin Solid Films.* 402 (2002) 195-202.
- [44] Q.H. Fan, A. Fernandes, E. Pereira, J. Gracio, Evaluation of biaxial stress in diamond films, *Diamond and Related Materials.* 8 (1999) 645-650.
- [45] L. Grinis, S. Dor, A. Ofir, A. Zaban, Electrophoretic deposition and compression of titania nanoparticle films for dye-sensitized solar cells, *J Photoch Photobio B.* 198 (2008) 52-59.
- [46] G. Syrrakostas, M. Giannouli, P. Yianoulis, Effects of paste storage on the properties of nanostructured thin films for the development of dye-sensitized solar cells, *Renew Energ.* 34 (2009) 1759-1764.
- [47] M.E. Straumanis, T. Ejima, W.J. James, The TiO₂ Phase Explored by the Lattice Constant and Density Method, *Acta Cryst.* 14 (1961) 493-497.

- [48] A. Zaban, M. Greenshtein, J. Bisquert, Determination of the Electron Lifetime in Nanocrystalline Dye Solar Cells by Open-Circuit Voltage Decay Measurements, *ChemPhysChem.* 4 (2003) 859-864.
- [49] G. Ruani, C. Ancora, F. Corticelli, C. Dionigi, C. Rossi, Single-step preparation of inverse opal titania films by the doctor blade technique, *Solar Energy Mater. Solar Cells.* 92 (2008) 537-542.
- [50] N. Jagtap, M. Bhagwat, P. Awati, V. Ramaswamy, Characterization of nanocrystalline anatase titania: an in situ HTXRD study, *Thermochimica Acta.* 427 (2005) 37-41.
- [51] B. O'Regan, M. Grätzel, A low-cost, high-efficiency solar cell based on dye-sensitized colloidal TiO₂ films, *Nature.* 353 (1991) 737-740.
- [52] M.K. Nazeeruddin, R. Humphry-Baker, P. Liska, M. Grätzel, Investigation of Sensitizer Adsorption and the Influence of Protons on Current and Voltage of a Dye-Sensitized Nanocrystalline TiO₂Solar Cell, *The Journal of Physical Chemistry B.* 107 (2003) 8981-8987.
- [53] M. Penny, T. Farrell, C. Please, A mathematical model for interfacial charge transfer at the semiconductor-dye-electrolyte interface of a dye-sensitised solar cell, *Solar Energy Mater. Solar Cells.* 92 (2008) 11-23.
- [54] M. Penny, T. Farrell, G. Will, A mathematical model for the anodic half cell of a dye-sensitised solar cell, *Solar Energy Mater. Solar Cells.* 92 (2008) 24-37.
- [55] E.M.J. Johansson, M. Hedlund, H. Siegbahn, H. Rensmo, Electronic and molecular surface structure of Ru(tctery)(NCS)(3) and Ru(dcbpy)(2)(NCS)(2) adsorbed from solution onto nanostructured TiO₂: A photoelectron spectroscopy study, *Journal of Physical Chemistry B.* 109 (2005) 22256-22263.
- [56] P. Suppan, N. Ghoneim, Royal Society of Chemistry, Solvatochromism, Royal Society of Chemistry, Cambridge, England, 1997.
- [57] T. Ono, T. Yamaguchi, H. Arakawa, Influence of Dye Adsorption Solvent on the Performance of a Mesoporous TiO₂ Dye-Sensitized Solar Cell Using Infrared Organic Dye *Journal of Solar Energy Engineering.* 132 (2010) 021101.
- [58] L. Peter, Transport, trapping and interfacial transfer of electrons in dye-sensitized nanocrystalline solar cells, *J Electroanal Chem.* 599 (2007) 233-240.
- [59] T. Clifford, J.R. Williams, Supercritical Fluid Methods and Protocols, Humana Press, Totowa, NJ, 2001.

- [60] Y. Ogomi, S. Sakaguchi, T. Kado, M. Kono, Y. Yamaguchi, S. Hayase, Ru dye uptake under pressurized CO₂ improvement of photovoltaic performances for dye-sensitized solar cells, *J. Electrochem. Soc.* 153 (2006) A2294-A2297.
- [61] T. Oekermann, D. Zhang, T. Yoshida, H. Minoura, Electron transport and back reaction in nanocrystalline TiO₂ films prepared by hydrothermal crystallization, *J. Phys. Chem. B.* 108 (2004) 2227-2235.
- [62] T.T. Ngo, D. Bush, C.A. Eckert, C.L. Liotta, Spectroscopic measurement of solid solubility in supercritical fluids, *Aiche J.* 47 (2001) 2566-2572.
- [63] Y. Ogomi, Y. Kashiwa, Y. Noma, Y. Fujita, S. Kojima, M. Kono, Y. Yamaguchi, S. Hayase, Photovoltaic performance of dye-sensitized solar cells stained with black dye under pressurized condition and mechanism for high efficiency, *Solar Energy Mater. Solar Cells.* 93 (2009) 1009-1012.
- [64] D. Zhao, T.Y. Peng, L.L. Lu, P. Cai, P. Jiang, Z.Q. Bian, Effect of annealing temperature on the photoelectrochemical properties of dye-sensitized solar cells made with mesoporous TiO₂ nanoparticles, *J. Phys. Chem. C.* 112 (2008) 8486-8494.
- [65] G. Schlichthorl, S.Y. Huang, J. Sprague, Band Edge Movement and Recombination Kinetics in Dye-Sensitized Nanocrystalline TiO₂ Solar Cells: A Study by Intensity Modulated Photovoltage Spectroscopy, *Journal of Physical Chemistry B.* 101 (1997) 8141-8155.
- [66] N.W. Duffy, L.M. Peter, R.M.G. Rajapakse, K.G.U. Wijayantha, Investigation of the Kinetics of the Back Reaction of Electrons with Tri-Iodide in Dye-Sensitized Nanocrystalline Photovoltaic Cells, *The Journal of Physical Chemistry B.* 104 (2000) 8916-8919.
- [67] J.J. Pietron, A.M. Stux, R.S. Compton, D.R. Rolison, Dye-sensitized titania aerogels as photovoltaic electrodes for electrochemical solar cells, *Solar Energy Mater. Solar Cells.* 91 (2007) 1066-1074.
- [68] P.A. Psathas, M.L. Janowiak, L.H. Garcia-Rubio, K.P. Johnston, Formation of Carbon Dioxide in Water Miniemulsions Using the Phase Inversion Temperature Method, *Langmuir.* 18 (2002) 3039-3046.
- [69] H. Yoshida, M. Sone, H. Wakabayashi, H. Yan, K. Abe, X.T. Tao, A. Mizushima, S. Ichihara, S. Miyata, New electroplating method of nickel in emulsion of supercritical carbon dioxide and electroplating solution to enhance uniformity and hardness of plated film, *Thin Solid Films.* 446 (2004) 194-199.

- [70] S.R.P. da Rocha, P.A. Psathas, E. Klein, K.P. Johnston, Concentrated CO₂-in-water emulsions with nonionic polymeric surfactants, *J. Colloid Interface Sci.* 239 (2001) 241-253.
- [71] M. Tian, J. Wang, J. Kurtz, T.E. Mallouk, M.H.W. Chan, Electrochemical Growth of Single-Crystal Metal Nanowires via a Two-Dimensional Nucleation and Growth Mechanism, *Nano Letters.* 3 (2003) 919-923.
- [72] M. Lai, D.J. Riley, Templated electrosynthesis of nanomaterials and porous structures, *J. Colloid Interface Sci.* 323 (2008) 203-212.
- [73] S. Inoue, S. Chu, K. Wada, D. Li, H. Haneda, New routes to formation of nanostructures on glass surface through anodic oxidation of sputtered aluminum, *Science and Technology of Advanced Materials.* 4 (2003) 269-276.
- [74] J. Eastoe, S. Gold, D.C. Steytler, Surfactants for CO₂, *Langmuir.* 22 (2006) 9832-9842.
- [75] W. Ryoo, S.E. Webber, K.P. Johnston, Water-in-carbon dioxide microemulsions with methylated branched hydrocarbon surfactants, *Ind. Eng. Chem. Res.* 42 (2003) 6348-6358.
- [76] V.V. Dhanuka, J.L. Dickson, W. Ryoo, K.P. Johnston, High internal phase CO₂-in-water emulsions stabilized with a branched nonionic hydrocarbon surfactant, *J. Colloid Interface Sci.* 298 (2006) 406-418.
- [77] H. Yan, M. Sone, A. Mizushima, T. Nagai, K. Abe, S. Ichihara, S. Miyata, Electroplating in CO₂-in-water and water-in-CO₂ emulsions using a nickel electroplating solution with anionic fluorinated surfactant, *Surf. Coat. Technol.* 187 (2004) 86-92.
- [78] C.T. Lee, W. Ryoo, P.G. Smith, J. Arellano, D.R. Mitchell, R.J. Lagow, S.E. Webber, K.P. Johnston, Carbon dioxide-in-water microemulsions, *J. Am. Chem. Soc.* 125 (2003) 3181-3189.
- [79] H. Yoshida, M. Sone, A. Mizushima, H. Yan, H. Wakabayashi, K. Abe, X.T. Tao, S. Ichihara, S. Miyata, Application of emulsion of dense carbon dioxide in electroplating solution with nonionic surfactants for nickel electroplating, *Surf. Coat. Technol.* 173 (2003) 285-292.
- [80] J.M. DeSimone, J.S. Keiper, Surfactants and self-assembly in carbon dioxide, *Curr. Opin. Solid State Mat. Sci.* 5 (2001) 333-341.
- [81] D. Shen, B.X. Han, Y. Dong, J.W. Chen, T.C. Mu, W.Z. Wu, J.L. Zhang, Z.H. Wu, B.Z. Dong, Compressed CO₂ in AOT reverse micellar solution: Effect on stability, percolation, and size, *J. Phys. Chem. B.* 109 (2005) 5796-5801.

- [82] H. Yoshida, M. Sone, A. Mizushima, K. Abe, X.T. Tao, S. Ichihara, S. Miyata, Electroplating of nanostructured nickel in emulsion of supercritical carbon dioxide in electrolyte solution, *Chem. Lett.* (2002) 1086-1087.
- [83] H. Yan, M. Sone, N. Sato, S. Ichihara, S. Miyata, The effects of dense carbon dioxide on nickel plating using emulsion of carbon dioxide in electroplating solution, *Surf. Coat. Technol.* 182 (2004) 329-334.
- [84] M.J. Zheng, L.D. Zhang, G.H. Li, W.Z. Shen, Fabrication and optical properties of large-scale uniform zinc oxide nanowire arrays by one-step electrochemical deposition technique, *Chemical Physics Letters.* 363 (2002) 123-128.
- [85] F. Triolo, A. Triolo, R. Triolo, J.D. Londono, G.D. Wignall, J.B. McClain, D.E. Betts, S. Wells, E.T. Samulski, J.M. DeSimone, Critical micelle density for the self-assembly of block copolymer surfactants in supercritical carbon dioxide, *Langmuir.* 16 (2000) 416-421.
- [86] J.L. Dickson, P.A. Psathas, B. Salinas, C. Ortiz-Estrada, G. Luna-Barcenas, H.S. Hwang, K.T. Lim, K.P. Johnston, Formation and growth of water-in-CO₂ miniemulsions, *Langmuir.* 19 (2003) 4895-4904.
- [87] M. Saitou, S. Oshiro, S.M.A. Hossain, Effect of temperature on nickel electrodeposition from a nickel sulfamate electrolyte, *J. Appl. Electrochem.* 38 (2008) 309-313.
- [88] M. Lai, D.J. Riley, Tempered Electrosynthesis of Zinc Oxide Nanorods, *Chemistry of Materials.* 18 (2006) 2233-2237.
- [89] Y. Ueno, H. Minoura, T. Nishikawa, M. Tsuiki, Electrophoretically Deposited Cds and Cdse Anodes for Photo-Electrochemical Cells, *J. Electrochem. Soc.* 130 (1983) 43-47.
- [90] G.Z. Cao, Growth of oxide nanorod arrays through sol electrophoretic deposition, *J. Phys. Chem. B.* 108 (2004) 19921-19931.
- [91] S.J. Limmer, S. Seraji, Y. Wu, T.P. Chou, C. Nguyen, G.Z. Cao, Template-based growth of various oxide nanorods by sol-gel electrophoresis, *Adv. Funct. Mater.* 12 (2002) 59-64.

BIOGRAPHICAL SKETCH

Fahd Mohsin Rajab finished high school in 1995 with recognized athletic and academic accomplishments. He joined Aramco Oil Company and was among a group of successful candidates to study bachelors in chemical engineering with a full scholarship. Fahd graduated in 2001 from Vanderbilt University and started a working career at Aramco in refining, planning and management for more than 4 years before he decided to pursue graduate studies.

Fahd received his master's degree in chemical engineering from the University of Florida in 2007. He then started his doctorate studies focusing on nanomaterials and its applications. He worked in various areas including purification of carbon nanotubes, transport in nanomaterials using supercritical fluids, thin film preparation, and fabrication and testing of dye sensitized solar cells. Fahd received his Ph.D. in chemical engineering from the University of Florida in the fall of 2010. Fahd plans to be involved in the educational and industry sectors. Fahd's background in refining and solar energy will help him continue active research for solutions to such important global problems.